Astronomy Letters, Vol. 27, No. 5, 2001, pp. 277–283. Translated from Pis'ma v Astronomicheskiĭ Zhurnal, Vol. 27, No. 5, 2001, pp. 323–329.

First Observations with the 64-m Kalyazin Telescope Included in a Ground-Based–Space Interferometer: The Quasar 3C 147

V. I. Slysh[1]*, M. V. Popov[1], B. Z. Kanevskiĭ[1], A. I. Smirnov[1], A. V. Kovalenko[1], Yu. P. Ilyasov[1], V. V. Oreshko[1], B. A. Poperechenko[2], H. Hirabayashi[3], K. M. Shibata[4], and E. B. Fomalont[5]

[1] *Astrospace Center, Lebedev Institute of Physics, Russian Academy of Sciences, ul. Profsoyuznaya 84/32, Moscow, 117810 Russia*
[2] *Special Design Office, Power Engineering Institute, Moscow, Russia*
[3] *Institute of Space and Astronautical Science, 3-1-1 Yoshinodai, Sagamihara-shi, Kanagawa 229-8510, Japan*
[4] *National Astronomical Observatory, 2-21-1 Osawa, Mitaka, Tokyo 181, Japan*
[5] *National Radio Astronomy Observatory, 520 Edgemont Road, Charlottesville, VA 22903, USA*

Received December 6, 2000

Abstract—The 64-m radio telescope equipped with an S-2 recording system in the town of Kalyazin was involved in an international fine-structure survey of quasars and active galactic nuclei carried out with a ground-based–space radio interferometer. The HALCA Japanese satellite in an orbit with an altitude of up to 24 000 km with an 8-m antenna was used as a space element of the interferometer. A radio image of the inner region of the CSS-type quasar 3C 147 was obtained with an angular resolution of ~0.3 mas at 6 cm. The image exhibits a core and several jet components mostly arranged in the main jet direction, but one of the components moves across the jet. No evidence was found for the superluminal separation of jet components. The estimated brightness temperature, $\sim 10^{11}$ K, is consistent with the theoretical limit imposed by synchro-Compton radiation.

Key words: *interferometry, quasars, fine structure*

1. INTRODUCTION

3C 147 is a compact (≤1″) steep-spectrum (CSS) radio source identified with a quasar at redshift $z = 0.545$. On an arcsecond (≈10 kpc) scale, there are two components asymmetrically located relative to the central core. Their asymmetry is attributed to the interaction of radio jets with galactic material. A 230-mas-long jet emerges from the core southwestward (Zhang *et al.* 1991). The spectrum of the core is flatter than that of the extended components and the jet. On a milliarcsecond scale, the core has a complex structure with deviations from a linear one; there are components displaced from the main axis. The separation between some components increases with time at a velocity of 2.4*c*, while other components are left in place (Alef *et al.* 1988). Alef *et al.* (1988) carried out their VLBI observations in 1978–1984 at a wavelength of 6 cm on the global network of telescopes. However, as was noted by the authors, the angular resolution was not high enough to analyze in detail the complex morphology and kinematics of 3C 147.

We performed VLBI observations of 3C 147 at 6 cm with an angular resolution that was approximately a factor of 2.5 higher than the resolution of the global network. It became possible to reach such a resolution by using the HALCA space radio telescope launched in Japan in 1997 (Hirabayashi *et al.* 1998) as an element of the VLBI network. The 64-m radio telescope near the town of Kalyazin (~200 km from Moscow) was first used as one of the ground-based radio telescopes of the network. It was the first observation with this telescope at 6 cm in the VLBI system.

2. OBSERVATIONS AND DATA REDUCTION

We observed the source 3C 147 (J0542+49) on March 18, 1999, for 8 h as part of the survey of compact radio sources with a high angular resolution, achieved by using the HALCA space telescope (Fomalont *et al.* 2000). The observations were carried out at a frequency of 4800 MHz in left-hand circular polarization in a 32-MHz band. Four ground-based radio telescopes and the HALCA space telescope were involved; their parameters are listed in Table 1.

* E-mail address for contacts: vslysh@asc.rssi.ru

Table 1. Parameters of the VLBI telescopes

Telescope	T_{sys}, K	Gain, K/Jy
1. Kalyazin 64 m	50	0.54
2. Usuda 64 m	100	1.04
3. Torun' 32 m	50	0.16
4. Shanghai 25 m	52	0.10
5. HALCA 8 m	90	0.0062

The 64-m Kalyazin radio telescope was equipped with a cooled low-noise transistor amplifier with a noise temperature of 16 K: we used a combined multifrequency feed, which allowed for simultaneous operation at several frequencies; the antenna aperture efficiency at 6 cm is 0.46. Given the feed losses, antenna and background noise, the total system temperature was 50 K at zenith. We used a hydrogen frequency standard as a stable frequency source for the local oscillator. The signal was recorded with an S-2 broadband tape recorder, which consisted of eight concurrently operating digital tape recorders. The signal was converted to videofrequencies and digitized by using the DAS (Data Acquisition System) videoterminal with digital filters designed at ATNF (Australia) for the S-2 recording system and made available to us for temporary use by the Jet Propulsion Laboratory (USA).

The other ground-based telescopes [64 m in Usuda (Japan), 25 m in Shanghai (China), and 32 m in Torun' (Poland)] used different recording systems. Data from the space telescope were received by the Green Bank (USA), Canberra (Australia), and Usuda (Japan) tracking stations and were recorded on magnetic tape. The signal was correlated with the correlator at the National Astronomical Observatory in Mitaka (Japan). To reduce the records from different telescopes to a single format, the signals were first converted to the VSOP format and recorded again.

The follow-up reduction was made at the Astrospace Center of the Lebedev Physical Institute using the AIPS software package developed at NRAO (USA) and installed on a Pentium-based PC with LINUX. Based on the telescopes' gains and the noise temperatures provided by the observatories (see Table 1), we performed the amplitude calibration.

The radio source was imaged using self-calibration by global fringe fitting, separately for the ground-based array of telescopes and for the combined ground-based–space array.

Figure 1 shows the filling of the *UV*-plane (a) for the ground-based array and (b) for the ground-based–space array. Since only four ground-based telescopes were involved in the experiment (two in Europe and two in Asia), the *UV*-plane filling in Fig. 1a is poor. The inner ring corresponds to the short baselines, Usuda–Shanghai and Kalyazin–Torun', and the outer rings correspond to the long baselines between the European and Asian telescopes. The *UV*-plane filling is considerably improved because of the long duration of the observations and because of the relatively high declination of the source. The beam sizes corresponding to this *UV*-plane filling are 1.28×0.83 mas, with a major-axis position angle of $-62\overset{\circ}{.}5$. Including the space telescope considerably extends the *UV*-plane filling (Fig. 1b), particularly in the *V* direction (north-south), and the synthesized beam, accordingly, narrows to 0.63×0.29 mas with a major-axis position angle of 89°. The ground-based part corresponding to Fig. 1a is seen at the center of Fig. 1b as three unfilled rings. The scales of Figs. 1a and 1b are different. Figure 1b was plotted for the first two hours of observations, when fringes were recorded with the ground-based-space baselines. For the ground-based network (Fig. 1a), the *UV*-plane filling is given for the entire observing session.

3. RESULTS

Although the total 6-cm flux from 3C 147 is 8 Jy, the core contains only ~10% of the total flux, while its remaining part comes from more extended, arcsecond-scale structures. Figure 2a shows the fringe spectrum for the baseline composed of the two ground-based telescopes in Usuda and Kalyazin. The spectrum exhibits several closely spaced peaks which correspond to individual components of the core; the brightest component corresponds to a fringe amplitude of ~50 mJy. Figure 2b presents the fringe spectrum for the baseline composed of the Kalyazin ground-based telescope and HALCA space telescope. The only peak corresponds to a fringe amplitude of ~40 mJy. It should be noted that the spectrum is presented here for the interval with the largest fringe amplitude. At other times, the amplitude was lower; since the signal-to-noise ratio was not that high (much of the time), the fringe amplitude was below the detection threshold of the global fringe fitting code. As was noted above, we chose for imaging only the first two hours of the observations with the involvement of the space radio telescope, while for the remaining time, we used data from the ground-based telescopes.

To assess the role of the space radio telescope, we constructed two radio images: first with the ground-based network alone and the second with the addition of the space radio telescope. The two images are shown in Fig. 3. The images were obtained by using the standard procedure of the AIPS package, including the Fourier transformation of *UV* data and cleaning. To reconstruct the image obtained with the ground-based network (Fig. 3a), we used a 0.8-mas-wide circular beam, which is slightly smaller than the synthesized beam. The image obtained with the space radio telescope added to the ground-based network was reconstructed with a 0.92×0.57 mas beam with a major-axis position angle of $55\overset{\circ}{.}3$; this beam corresponded to the *UV*-plane filling we used.

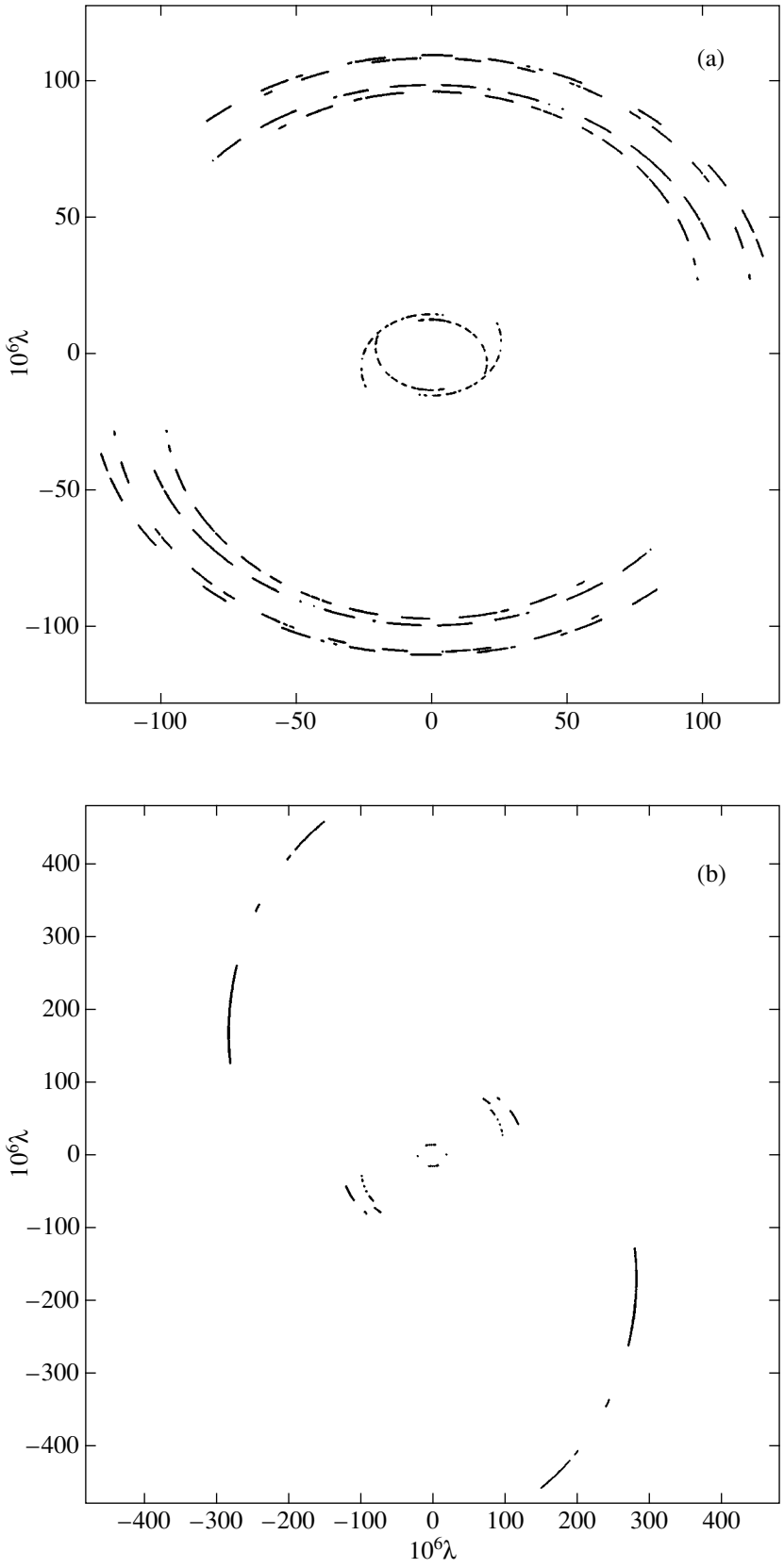

Fig. 1. Filling of the *UV*-plane during the 6-cm observations of 3C 147: (a) ground-based array: Kalyazin, Usuda, Torun', Shanghai; (b) ground-based–space array: ground-based array + HALCA.

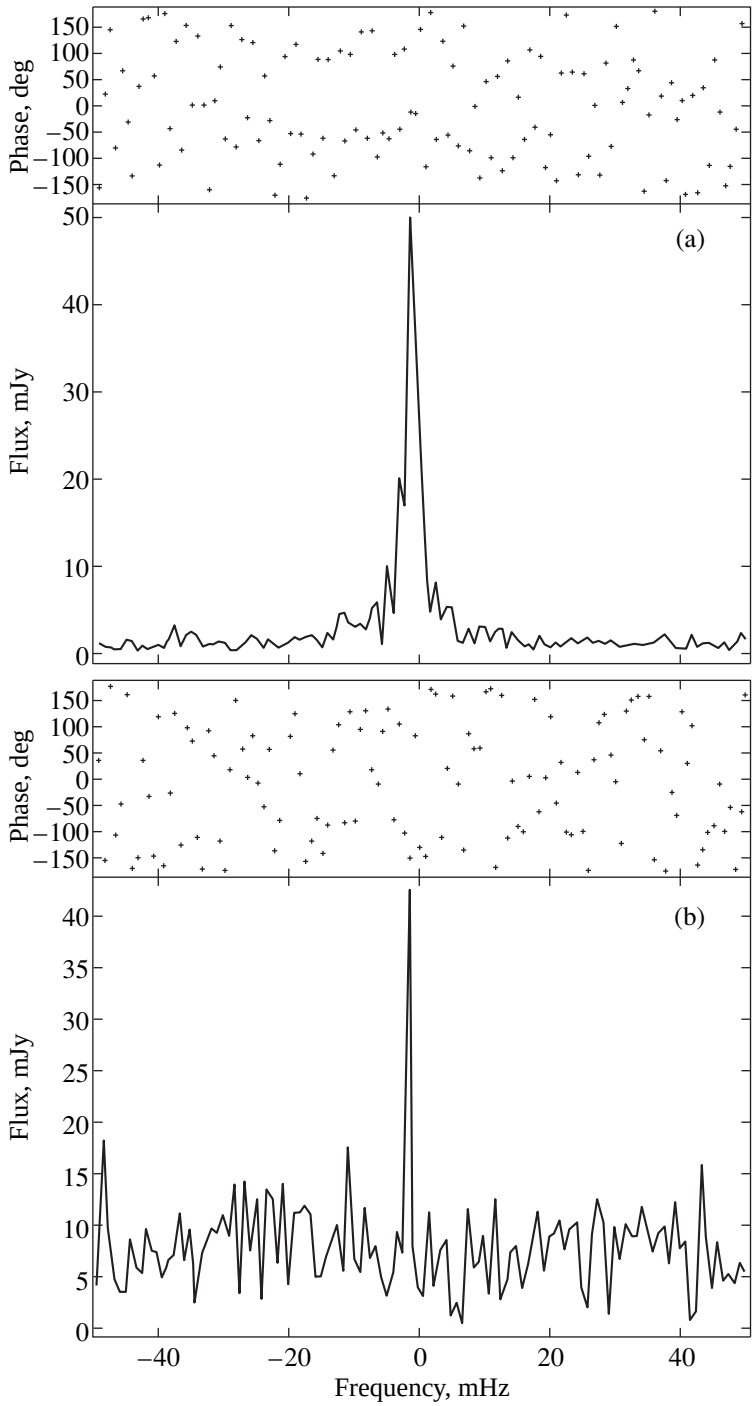

Fig. 2. Fringe spectra for the baselines: (a) Kalyazin–Usuda and (b) Kalyazin–HALCA.

The two images are similar; at least four strong components can be distinguished in them. The weaker components do not always coincide on both maps, mainly because of the stronger noise on the map of Fig. 3b, which was obtained with the small-diameter space telescope. In addition, because of the incomplete *UV*-plane filling, the dynamic range of the maps is narrow, and the weak features can be statistically insignificant. The positions, fluxes, and sizes of the components corrected for beam broadening were determined by fitting them with bivariate Gaussian functions. The parameters of the four strongest components determined from the map of Fig. 3a (ground-based array) are listed in Table 2. Similar parameters were also derived from the map of Fig. 3b, obtained with the involvement of the space radio telescope.

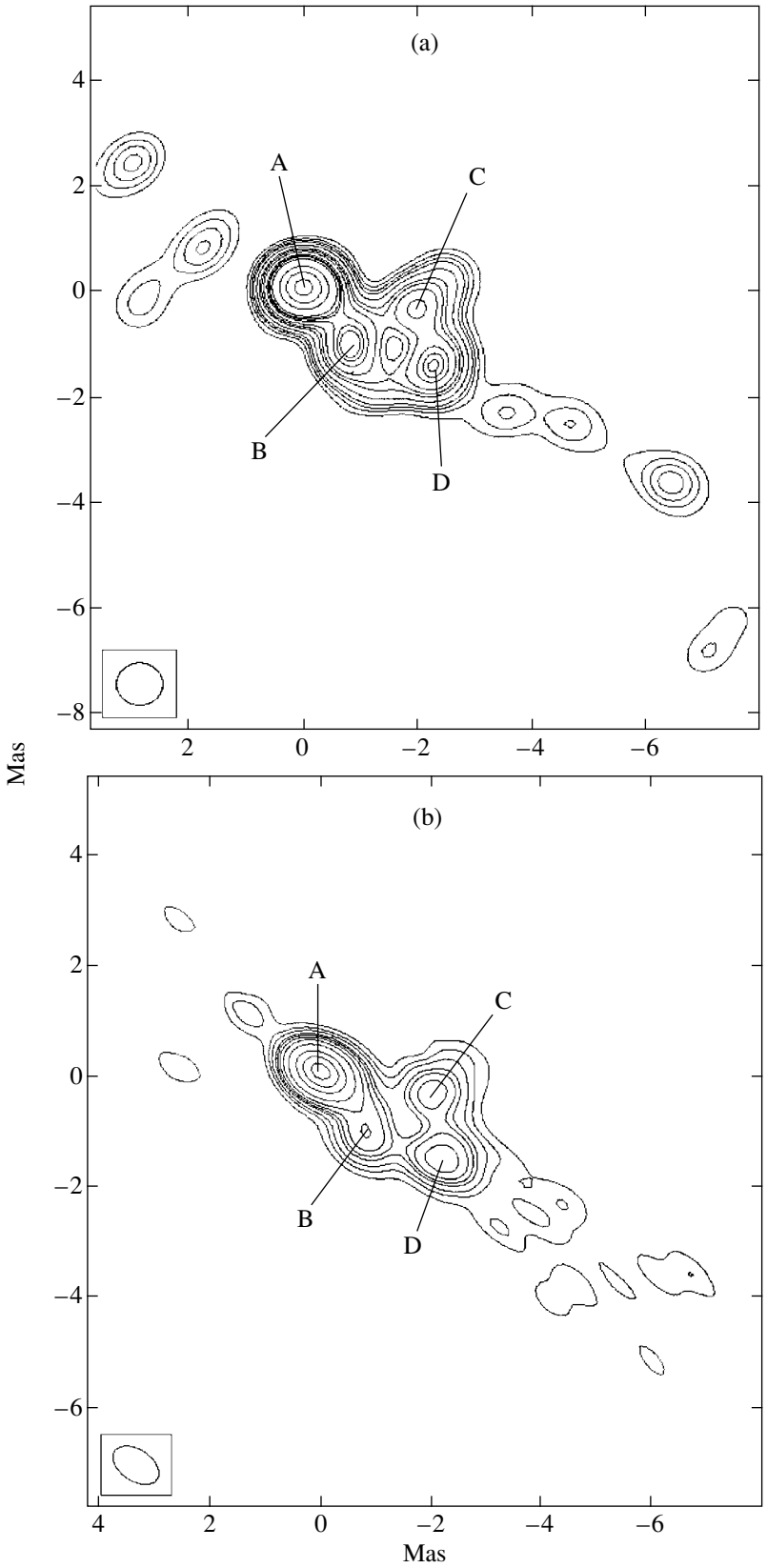

Fig. 3. A radio image of 3C 147 at 6 cm. The beam is shown in the left corner: (a) ground-based array: the contours are (0.2, 0.3, 0.4, 0.5, 0.7, 1, 1.2, 1.5, 2, 3, 5, 7, 9) × 8.1 mJy/beam; (b) ground-based–space array: the contours are (0.3, 0.4, 0.5, 0.7, 1, 1.2, 1.5, 2, 3, 5, 7, 9) × 7.2 mJy/beam.

Table 2. Gaussian components in the image of 3C 147 (ground-based array)

Source components	*S*, mJy	$\Delta\alpha$, mas	$\Delta\delta$, mas	θ_{max}, mas	θ_{min}, mas	Position angle, deg
A	84	0	0	0.23	0.11	100
B	40	−0.83	−1.00	1.19	0.26	16
C	29	−2.01	−0.24	0.97	0.25	130
D	33	−2.26	−1.41	0.80	0.42	147

Note: Coordinates of the reference feature (J2000): $\alpha = 5^h42^m36\overset{s}{.}138$; $\delta = 49°51'07\overset{''}{.}238$. The mean position errors are ~0.05 mas.

4. DISCUSSION

In our observations, we studied the inner part of the entire CSS source 3C 147 with a size of less than 10 mas (80 pc) at a total extent of 700 mas (5.6 kpc) (Ludke *et al.* 1998). A core (A) and a jet consisting of several components (B, C, and D) are observed in this region (Fig. 3). It is remarkable that the jet components in this source are not aligned: whereas core A and components B and D lie on an almost rectilinear curve following the general jet direction in 3C 147 on a large scale, component C goes in a direction almost perpendicular to the main jet direction. This peculiarity of the structure is also characteristic of some other CSS sources. The previous VLBI observations of 3C 147 at 6 cm in 1978–1984 revealed a similar structure (Alef *et al.* 1988). On the VLBI maps obtained at four different epochs with an angular resolution close to our resolution, the same four components, A–D, can be distinguished. Their relative positions changed little during the 21 years that elapsed between the first observations of Alef *et al.* (1988) in 1978 and our observations in 1999. Alef *et al.* (1988) reported an increase in the separation between components A and B during 1981–1984 corresponding to the motion at a velocity of 2.4*c*, but the 1978 observations are inconsistent with this model. In our observations, the separation between components A and B was virtually the same as 21 years ago; hence, these components were stationary. At the same time, Alef *et al.* (1988) found no change in the separation between components A and D; our observations are consistent with the absence of a superluminal separation of components A and D. In the recent VLBI observations of 1995 (also at 6 cm), Nan *et al.* (2000) confirmed the superluminal separation of components A and B. In this work, the brightest component was identified as B, while the weaker component located northeastward of the brightest component was thought to be component A. On the map of Fig. 3a, two weak features are seen at this location which were not included in Table 2 because of their low significance. Since the breakdown of such a complex image as that of 3C 147 into Gaussian components cannot be unambiguous because of the incomplete *UV*-plane filling, our data cannot be used with confidence to estimate superluminal motions.

The ground-based–space interferometer allows us to achieve a high angular resolution and to estimate the brightness temperature of the components in 3C 147. The angular size of the brightest feature A measured with the ground-based array corresponds to a brightness temperature of 2.5×10^{11} K. The angular size measured with the ground-based–space array is slightly larger and corresponds to a brightness temperature of 0.8×10^{11} K. Of these two values, the latter should be preferred, because the angular sizes were measured by the ground-based-space interferometer with a higher reliability, whereas the angular sizes obtained with the ground-based array are at the limit of its angular resolution. Our brightness temperatures correspond to the limit imposed by inverse Compton scattering (Kellermann and Pauliny-Toth 1969), which provides circumstantial evidence that there is no significant Doppler enhancement attributable to superluminal motion. A more comprehensive analysis of the results of the study of 3C 147 and other sources as part of the survey with the HALCA satellite will be given in a special publication.

5. CONCLUSION

The first observations of the 3C 147 structure by using the ground-based–space interferometer with the involvement of the 64-m Kalyazin radio telescope have allowed us to image this quasar with a submilliarcsecond angular resolution.

We detected the components corresponding to the core and the jet; in the jet, there are components in a direction perpendicular to the main jet direction.

We found no evidence for the superluminal separation of some of the components reported in the literature. The image of the quasar is consistent with the assumption of its stationary components.

The brightness temperature of the strongest component is ~10^{11} K and corresponds to the synchro-Compton limit.

REFERENCES

1. W. Alef, E. Preuss, K. I. Kellermann, *et al.*, in *Proceedings of 129th IAU Symposium "The Impact of VLBI on*

Astrophysics and Geophysics," Ed. by M. J. Reid and J. M. Moran (Kluwer, Dordrecht, 1988), p. 95.

2. E. Fomalont, H. Hirabayashi, Y. Murata, *et al.*, in *Proceedings of the VSOP Symposium "Astrophysical Phenomena Revealed by Space VLBI," Institute of Space and Astronautic Science, Sagamihara, Kanagawa, 2000*, Ed. by H. Hirabayashi, P. G. Edwards, and D. W. Murohy, p. 167.
3. H. Hirabayashi, H. Hirosawa, H. Kobayashi, *et al.*, Science **281**, 1825 (1998).
4. K. I. Kellermann and I. I. K. Pauliny-Toth, Astrophys. J. Lett. **155**, 171 (1969).
5. E. Ludke, S. T. Garrington, R. E. Spencer, *et al.*, Mon. Not. R. Astron. Soc. **299**, 467 (1998).
6. R. D. Nan, H. Y. Zhang, D. C. Gabuzda, *et al.*, Astron. Astrophys. **357**, 891 (2000).
7. F. J. Zhang, C. E. Akujor, H. S. Chu, *et al.*, Mon. Not. R. Astron. Soc. **250**, 650 (1991).

Translated by G. Rudnitskiĭ

Astronomy Letters, Vol. 27, No. 5, 2001, pp. 284–291. Translated from Pis'ma v Astronomicheskiĭ Zhurnal, Vol. 27, No. 5, 2001, pp. 330–338.

Optical Studies of Extragalactic Infrared Sources

S. K. Balaian[1]*, S. A. Akopian[1], A. M. Mikaelian[1], and A. N. Burenkov[2]

[1] *Burakan Astrophysical Observatory, National Academy of Sciences of Armenia, Armenia*
[2] *Special Astrophysical Observatory, Russian Academy of Sciences, Nizhni Arkhyz, Stavropol kraĭ, 357147 Russia*

Received March 30, 2000; in final form, November 4, 2000

Abstract—We present spectroscopic observations of 41 galaxies with the 6-m telescope, 31 of which are the optical counterparts of IRAS PSC infrared sources. Redshifts and activity types are provided. © *2001 MAIK "Nauka/Interperiodica".*

Key words: *galaxies, galaxy groups and clusters, intergalactic gas*

INTRODUCTION

The discovery of intense IR emission from extragalactic objects, such as quasars, AGNs, and galaxies with violent star formation, initiated many studies aimed at identifying IRAS (InfraRed Astronomical Satellite) sources. Optical identifications of IR sources are made, in particular, for samples of IR sources either in separate sky regions or with a certain IR energy distribution based on the IRAS fluxes at 12, 25, 60, and 100 μm (Johnson and Klemola 1987; Strauss and Huchra 1988; Wolstencroft *et al.* 1986; Legget *et al.* 1987; Wang *et al.* 1991; Fisher *et al.* 1995; Hau *et al.* 1995; Yuan *et al.* 1996; Saunders *et al.* 1999).

Nevertheless, for many sources, in particular, for those from the IRAS PSC catalog (1989), the optical identifications remain uncertain. To establish these identifications, studies are being carried out at the Burakan Observatory by using plates from the First Burakan Survey (FBS) (Markaryan *et al.* 1989) in the region $+61° < \delta < +90°$ at high Galactic latitudes. An analysis of the low-dispersion spectra for the objects falling within the position error ellipses of IR sources, along with the use of Digital Sky Survey (DSS) data and, in some cases, direct images of the corresponding sky regions obtained with the 2.6-m Burakan Observatory telescope, allowed about 1500 previously unidentified IRAS sources to be identified [see Mikaelian (2000) and references therein]. More than one thousand of these sources are extragalactic objects, which are of greatest interest in our studies.

Observations of the galaxies from our sample with the 6-m Special Astrophysical Observatory (SAO) telescope, the 2.6-m Burakan Observatory telescope, and the 1.93-m Haute Provence Observatory telescope (France) facilitate the concurrent solution of several problems. These problems range from confirming the extragalactic nature of objects and determining their redshifts to detailed analyses of the objects' structure, which proved to be of greatest interest, such as galaxies with enhanced IR luminosities and/or with nuclear or outburst activity.

SPECTROSCOPIC OBSERVATIONS

Previously (Mikaelian *et al.* 1998), apart from describing the sample of 209 extragalactic objects identified at that time, we presented our spectroscopic observations of 11 of the brightest sample galaxies obtained with the 6-m SAO telescope.

Here, we present our spectroscopic observations of optical identifications for 31 more extragalactic IR sources from the IRAS PSC catalog [see Mikaelian (2000) and references therein].

The observations were carried out from July 1997 until March 1999 with a long-slit fast spectrograph mounted at the prime focus of the 6-m SAO telescope (Afanas'ev *et al.* 1995). Before March 1999, we used a 530×580 CCD array and, depending on the grating angle, recorded one of the two spectral ranges, λ4500–7800 Å or λ3800–7000 Å, with a spectral resolution of ~16 Å. In March 1999, we took spectra with a 1024×1024 CCD array in the range λ3600–8000 Å with a slightly higher resolution (14 Å).

Except for the cases where, according to the morphology of the observed galaxy, a special slit orientation was preferred, the spectrograph slit was oriented during the observations in such a way as to obtain spectra for the largest number of the nearest objects, in particular, in an effort to determine whether the nearest galaxies belong to the same group and to study them simultaneously. The estimated spectral types of the stars that fell within the spectrograph slit during the observations are given below together with a description of the simultaneously observed galaxy.

* E-mail address for contacts: bal@moon.yerphi.am

Table 1 gives a log of observations for the galaxies, which are the optical identifications of point IRAS sources and some of the galaxies closest to them. Its columns are: (1) names of the IRAS objects (followed by a Latin letter for the galaxies in a group); (2) and (3) coordinates of the optical objects at epoch 1950.0; (4) exposure times; (5) position angles of the spectrograph slit; and (6) dates of observation. It should be added that when there is a group, the IRAS PSC source is optically identified in most cases with the galaxy from the group that is also most frequently identified with a radio source.

Apart from the objects listed in Table 1, we performed spectroscopic observations for the optical counterparts of IRAS 04137+6940, IRAS 05400+6342, and IRAS 05577+6141, selected as candidates for quasars from their low-dispersion spectra (Mikaelian 1997; Mikaelian *et al.* 1997). All three sources proved to be G–K stars, without confirming the preliminary classification.

RESULTS

We reduced our spectra with the IRAF (Image Reduction Analysis Facility) software package and with the software package developed at the SAO (Vlasyuk 1993). We used a He–Ne–Ar lamp for wavelength calibration of the spectra. For flux calibration of the spectra, we observed the spectrophotometric standard stars PG 1708+602, HD 217086, and G191B2B (Massey *et al.* 1988).

The results of our observations (redshifts and activity types for all the observed galaxies together with their main parameters) are summarized in Table 2. Figure 1 shows tracings of some of our spectra.

The columns of Table 2 give: (1) names of the identified IRAS sources (followed by a letter when there are several components); (2) morphological types; (3) angular sizes of the galaxies (in arcseconds); (4) total magnitudes (close to *V*), as estimated from the Palomar Observatory Sky Survey O and E maps; (5) observed redshifts; (6), (7), and (8) ratios R_1, R_2, and R_3 (see below); (9) types of objects: Abs.—galaxies whose spectra are dominated by absorption lines; Norm.—galaxies with emission only in Hα in the presence of absorption lines; H II—galaxies or galaxy regions with sites of star formation at different stages of activity; LINER—galaxies with low-ionization nuclear emission regions (Heckman 1980); Comp. (Composite)—galaxies with composite spectra and AGN-type activity (Veron *et al.* 1997); and Sy2—galaxies with AGN-type nuclear activity.

To separate objects with the spectral behavior typical of H II regions from objects with the spectra typical of AGNs, such as Sy and LINER galaxies, we used a diagnostic based on the intensity ratios of permitted and forbidden lines (Veilleux and Osterbrok 1987). When estimating the activity type of an object, we used the ratio $R_1 \equiv$ [NII] λ6584 Å/Hα as the main criterion, because Hα emission in seen in the spectra of all program galaxies, then $R_2 \equiv$ [OIII]λ5007 Å/Hβ, $R_3 \equiv$ [SII](λ6716 + λ6731)/Hα, and $R_4 \equiv$ [OI] λ6300/Hα if the corresponding lines were present. Note that the ratio R_1 for our dispersion could be computed only by using a Gauss analysis.

Figure 2 shows two diagnostic diagrams (Veilleux and Osterbrock 1987) that illustrate the distribution of some of the galaxies from among those presented here (see Table 2) and in our previous paper (Mikaelian *et al.* 1998) on activity zones. The first and second diagrams show the distribution of objects in the R_2–R_1 and R_2–R_3 planes, respectively. In both diagrams, the region of H II galaxies at the stage of star formation lies to the left from the curve, while the rectilinear segment divides the region of galaxies with evidence of nuclear activity to the right from the curve into two subregions: Sy2 and LINER galaxies.

We calculated the IR luminosities L_{FIR} for all the observed optical counterparts of IR sources by using the formula

$$L_{FIR}(L_\odot) = 5.6 \times 10^5\,[D(\mathrm{Mpc})]^2\,(2.58F_{60} + F_{100})$$

(Duc *et al.* 1997), which fits the luminosity in the range λ40–120 μm (Lonsdale *et al.* 1985) for the assumed $H_0 = 75$ km s^{-1} Mpc^{-1}. The derived far-IR luminosities do not exceed the lower luminosity threshold corresponding to ultraluminous infrared galaxies (ULIRG), i.e., $L_{FIR} < 6.5 \times 10^{11} L_\odot$ for all objects.

DESCRIPTION OF THE SPECTRA

IRAS 03424+8424. Its spectrum exhibits only comparable (in intensity) emission features in the Hα and [NII] λ6584 Å lines. According to R_1, the object is a nonclassical LINER galaxy (Filippenko and Sargent 1985).

IRAS 05401+6435. The Hα, Hβ, Hγ, [OIII] λ5007, 4959 and [OI] λ6300, as well as [NII] λ6584 and [SII](λ6716+λ6731) lines with $R_1 \approx 0.4$, $R_2 \approx 1$, $R_3 \approx 0.3$, and $R_4 \approx 0.04$ are observed in emission. The nearest object located about 20″ west of the galaxy along the spectrograph slit is an F star.

IRAS 06432+8551b. Apart from a strong hydrogen line, the emission in its spectrum is represented by the [OIII] λ5007, 4959, [OI] λ6300 lines and by the [SII](λ6716+λ6731) doublet. The object located 27″ northeast of the galaxy is a G star.

IRAS 09002+8106. This galaxy is at a late continuum phase of outburst activity (Terlevich 1997). An absorption galaxy with the redshift $z = 0.2038$ lies about 23″ north of the object.

IRAS 09062+8134a,b. These two galaxies are similar in redshifts and in spectral emission features. In both spectra, the emission is represented by Hα lines of virtually identical intensity accompanied by the [NII] λ6584 line, which is stronger than that in IRAS 09062+8134a, the [SII] (λ6716+λ6731) doublet, and the N_1 [OIII] λ 5007 line. The spectrum of the

Table 1. Log of observations

IRAS source	α (1950)	δ (1950)	Exposure, s	P. A.	Date of observation
03424+8424	$03^h42^m46^s.6$	+84°24′36″	900; 1200	120°	Mar. 25, 1999
05401+6435	05 40 07.4	+64 35 48	600	51	Jan. 27, 1998
06432+8551b	06 43 22.4	+85 50 59	900; 600	151	Jan. 15, 1999
07007+8242	07 00 51.5	+82 42 20	1200	86	Mar. 25, 1999
08095+6445	08 09 35.8	+64 45 46	600	50	Dec. 4, 1997
09002+8106	09 00 18.3	+81 06 00	600	84	Jan. 12, 1999
09062+8134a	09 06 24.9	+81 34 43	900; 900	26; 19	Jan. 15, 1999
09062+8134b	09 06 30.8	+81 35 25	900	19	–
09103+8326	09 10 24.9	+83 26 39	600; 600	148	Jan. 12, 1999
09418+8124	09 41 58.6	+81 25 28	900	63	Jan. 15, 1999
09477+7050a	09 47 39.5	+70 50 41	300	137	Mar. 10, 1999
09477+7050b	09 47 41.5	+70 50 43	600; 600	161	–
09477+7050c	09 47 42.4	+70 50 32	600; 600	161	–
09571+8435	09 51 01.6	+84 35 14	900	67	Jan. 15, 1999
15356+6119a	15 35 42.4	+61 19 10	600	128	July 30, 1997
15356+6119b	15 35 44.1	+61 19 27	600	135	–
15427+6141	15 42 47.7	+61 41 12	900	178	–
15449+6459	15 44 58.2	+64 59 08	600	136	–
16030+6312a	16 03 00.3	+63 12 41	600	111	–
16030+6312b	16 03 04.7	+63 12 29	600	111	–
16101+6345	16 10 11.1	+63 45 09	600	110	–
16452+6418a	16 45 16.4	+64 17 27	600	128	–
16452+6418b	16 45 17.0	+64 18 18	600	129	–
16452+6418c	16 45 18.1	+64 18 05	600	97	–
16452+6418d	16 45 19.4	+64 18 03	600; 600	97; 129	–
17008+6444	17 00 50.1	+64 44 51	300; 300	163	July 27, 1997
17017+6416	17 01 49.2	+64 16 33	600; 600	54	–
17102+6442	17 10 15.5	+64 42 50	600	58	–
17173+6119	17 17 23.8	+61 19 04	600	176	–
17190+6219	17 19 03.3	+62 19 43	900	3	–
17207+6307	17 20 39.7	+63 07 24	900	4	–
17349+6139a	17 34 59.8	+61 39 23	900; 900	8	–
17349+6139b	17 35 00.3	+61 39 42	900; 900	8	–
17442+6130	17 44 19.4	+61 30 51	600	148	–
17469+6416	17 46 59.6	+64 16 48	600	14	–
17552+6209	17 55 12.9	+62 09 59	900	12	–
18116+6328	18 11 38.3	+63 29 02	600	88	July 26, 1997
18169+6433c	18 16 58.5	+64 32 42	900	91	July 30, 1997
18169+6433d	18 17 00.7	+64 32 44	900	91	–
18247+6102	18 24 41.1	+61 02 05	600; 600	12	July 27, 1997
18252+6315	18 25 14.8	+63 15 49	900	21	–

fainter galaxy, IRAS 09062+8134b, also exhibits a weak Hβ line. According to R_1, which exceeds 0.7, IRAS 09062+8134a is a nonclassical LINER galaxy. It is also identified with an IR PSC source and is an NVSS radio source (Condon *et al.* 1998).

IRAS 15356+6119a,b. These two galaxies, which belong to the same group, have identical spectra with the same $R_1 \approx 0.4$ and $R_3 \approx 0.1$. IRAS 15356+6119a is identified with a PSC source; this galaxy is simultaneously an NVSS radio source. The object 18″ west of

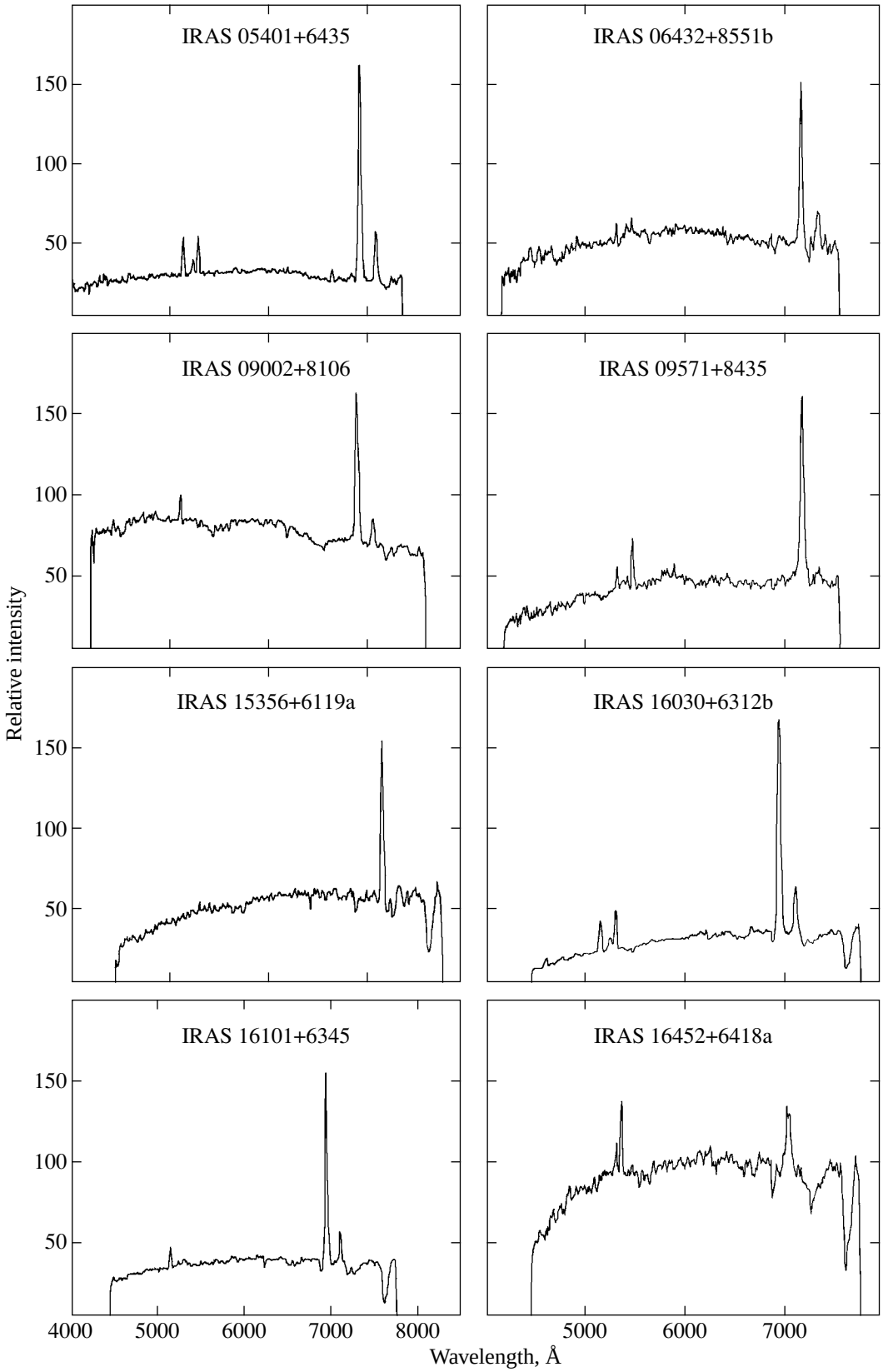

Fig. 1. Spectra of the galaxies optically identified with IRAS sources taken with the 6-m SAO telescope.

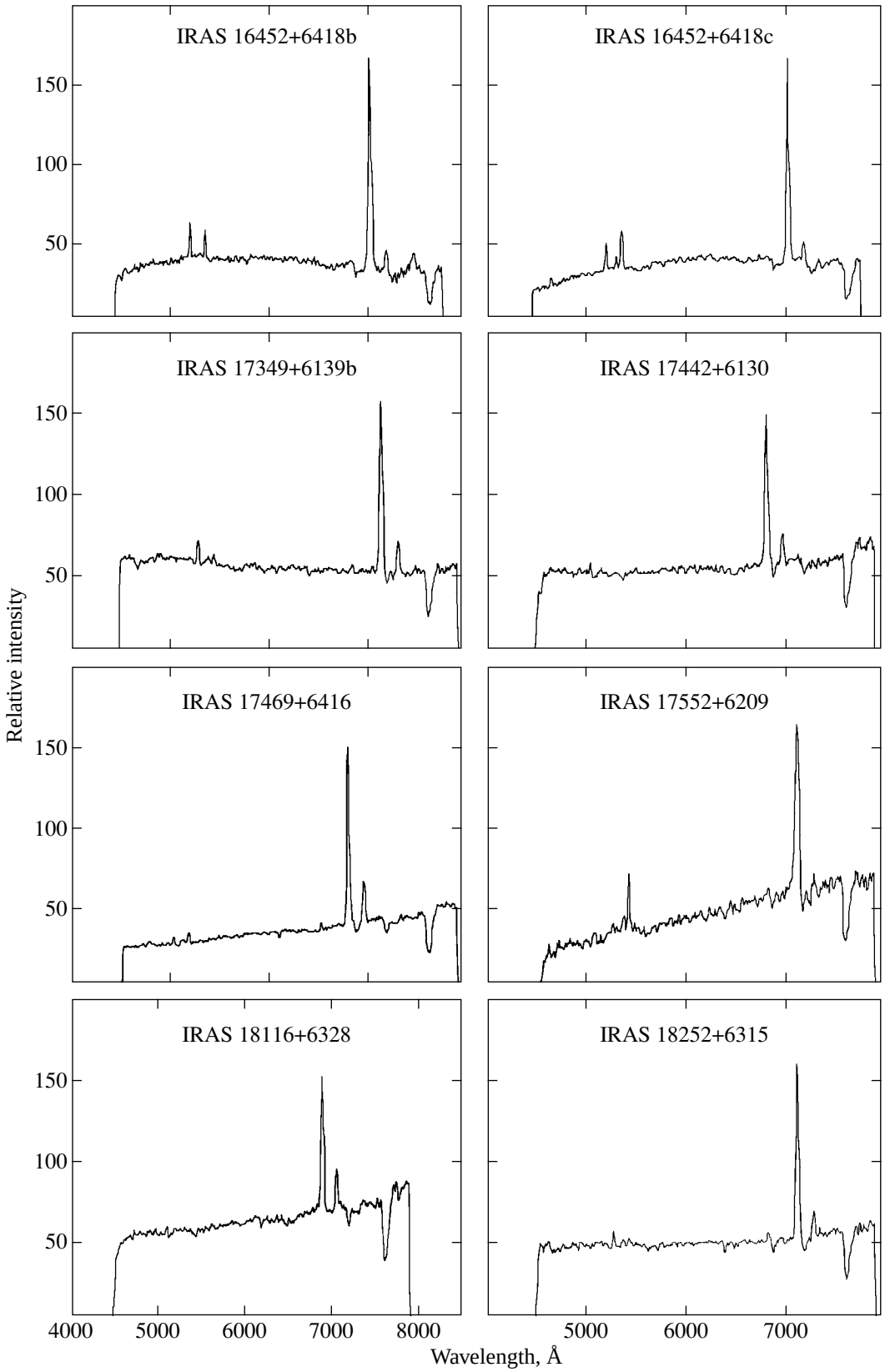
IRAS 16452+6418b
IRAS 16452+6418c
IRAS 17349+6139b
IRAS 17442+6130
IRAS 17469+6416
IRAS 17552+6209
IRAS 18116+6328
IRAS 18252+6315
Relative intensity
Wavelength, Å
150
100
50
4000
5000
6000
7000
8000

Fig. 1. (Contd.)

Table 2. Basic galaxy parameters

IRAS source	Morphological type	Angular size	m	z	R_1	R_2	R_3	Type of object
03424+8424	Sb:	13″ × 9″	16.0	0.0744	0.81	–	–	LINER:
05401+6435	S	10 × 8	15.2	0.0539	0.41	1.01	0.32	H II
06432+8551b	Sa	13 × 11	16.5	0.0891	0.11	1.20	0.19	H II
07007+8242	Sab	16 × 15	16.9	0.0586	0.27	–	0.21	H II
08095+6445	Sb:	46 × 12	14.1	0.0294	–	–	–	Norm.
09002+8106	Sab	17 × 13	16.6	0.0494	0.42	–	0.23	H II
09062+8134a	Sa	17 × 11	16.8	0.0495	0.79	–	0.31	LINER:
09062+8134b	Sa	12 × 7	17.9	0.0491	0.46	–	0.51	H II
09103+8326	Sa	29 × 11	17.1	0.0497	0.41	–	0.30	H II
09418+8124	Sa	31 × 10	16.0	0.0398	–	–	–	Abs.
09477+7050a	S:	6 × 5	18.5	0.1268	0.47	–	–	Norm.
09477+7050b	Sb:	7 × 6	18.0	0.1270	0.24	0.78	0.49	H II
09477+7050c	Gal:	6 × 6	17.5	0.1277	0.22	1.19	0.23	H II
09571+8435	Sa	13 × 11	16.5	0.0924	0.03	2.80	0.02	H II
15356+6119a	Gal.	11 × 9	16.4	0.0886	0.44	–	0.11	H II
15356+6119b	Gal.	16 × 14	14.4	0.0882	0.50	–	0.10	H II
15427+6141	Sa:	10 × 7	17.6	0.0573	–	–	–	Norm.
15449+6459	Sa:	22 × 12	15.3	0.0373	–	–	–	Norm.
16030+6312a	S:	12 × 9	16.8	0.0548	0.46	1.77	0.23	Norm.
16030+6312b	S	23 × 16	15.9	0.0569	–	1.30	0.22	H II
16101+6345	Gal.	13 × 9	16.5	0.0563	0.45	0.43	0.29	H II
16452+6418a	S:	13 × 12	16.3	0.0697	0.75	15.0	–	Sy2
16452+6418b	Gal:	8 × 8	16.6	0.0684	0.54	0.80	0.30	H II
16452+6418c	Sa:	21 × 13	14.2	0.0685	0.41	2.01	0.16	H II
16452+6418d	Irr:	13 × 11	17.1	0.0697	0.38	1.36	0.09	H II
17008+6444	Gal	27 × 18	12.6	0.0278	0.37	0.33	0.20	H II
17017+6416	Sa:	19 × 15	14.1	0.0848	0.44	1.75	0.14	H II
17102+6442	SBb:	17 × 11	14.4	0.0789	0.40	0.51	0.22	H II
17173+6119	SO/Sa:	20 × 11	14.7	0.0735	0.50	4.61	0.22	Comp.
17190+6219	Sb:	17 × 7	17.0	0.0808	0.38	–	0.38	Norm.
17207+6307	Sab:	19 × 13	15.3	0.0336	0.42	0.67	0.29	H II
17349+6139a	S	13 × 11	16.2	0.0858	0.42	–	0.40	H II
17349+6139b	S	6 × 4	18.8	0.0862	0.40	0.38	0.26	Norm.
17442+6130b	Sb:	18 × 15	14.0	0.0365	0.51	–	0.26	Norm.
17469+6416	S:	17 × 11	14.6	0.0355	0.49	1.50	0.31	H II
17552+6209	Sb:	14 × 8	16.4	0.0836	0.75	7.96	0.18	Sy2
18116+6328	S:	20 × 15	13.9	0.0481	0.49	–	0.35	Norm.
18169+6433c	Sa:	53 × 11	12.4	0.0208	0.43	–	0.28	H II
18169+6433d	S	19 × 6	15.1	0.0209	0.40	2.50	0.25	H II
18247+6102	S	19 × 13	15.7	0.0732	0.75	1.60	0.20	LINER
18252+6315	Sb:	19 × 14	15.9	0.0838	0.57	0.40	0.22	H II

IRAS 15356+6119a, which fell within the spectrograph slit during one of the exposures (P.A. = 128), is a G star.

IRAS 16030+6312a,b. The optical counterpart of the IR and radio sources is the brightest of the two observed galaxies belonging to the same group, which is designated here as IRAS 16030+6312b. The spectra of the two galaxies differ significantly. Only the Hα, [NII] λ6584, and [SII] λ6716, 6731 lines are in emission in IRAS 16030+6312a. Apart from the Hβ and Hγ emission lines, the spectrum of IRAS 16030+6312b exhibits the [OIII] λ5007, 4959 emission lines and a weak [OI] λ6300 line.

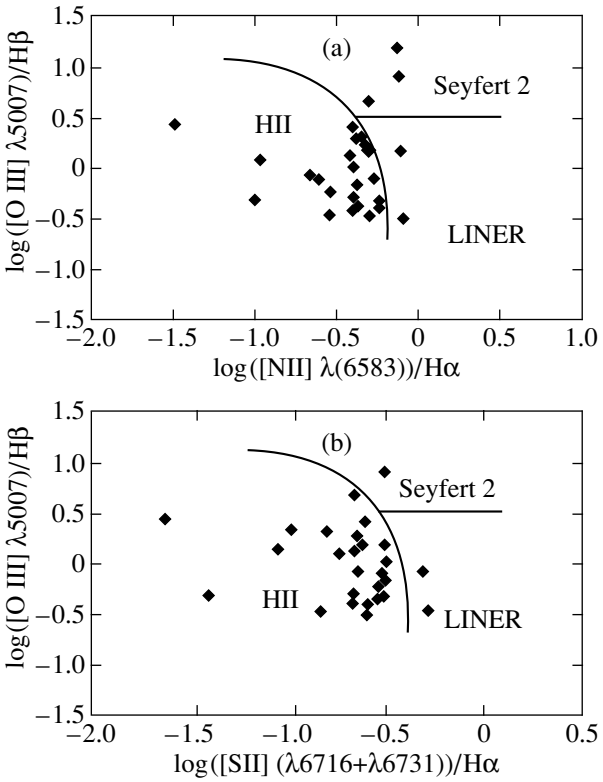

Fig. 2. Distribution of some galaxies in spectral classification diagrams. The diagrams are plots of [OIII]/Hβ intensity ratio versus (a) [NII]/Hα and (b) [SII]/Hα.

IRAS 16101+6345. The first two Balmer lines, nitrogen and sulfur lines, as well as a barely noticeable N_1 oxygen line are in emission. The galaxy is not only an infrared source, but also a radio source (according to the NVSS catalog).

IRAS 16452+6418a,b,c,d. The four galaxies observed near a point IRAS source have approximately the same redshifts. The optical counterpart of this IRAS source is the interacting pair of galaxies IRAS 16452+6418c,d. The same galaxies are also identified with a radio source from the NVSS catalog. Their spectra lead us to conclude that IRAS 16452+6418b,c,d are at approximately the same stage of star formation and that IRAS 16452+6418c,d is an interacting pair. The large angular diameter of IRAS 16452+6418c allowed us to trace the enhancement of Hα, Hβ, and Hγ along the slit from west to east, where Hβ dominates in intensity over the N_1 [OIII] λ5007 line.

IRAS 16452+6418a, which is relatively isolated from the other three galaxies, is most active (Sy2), as suggested $R_1 \geq 0.75$ and $R_2 \gg 3$.

IRAS 17173+6119. When the emission-line intensities change along the galaxy's major axis, the ratios R_1 and R_2 take their peak values ($R_1 = 0.65$ and $R_2 = 4.6$) in different parts of the galaxy, pointing to AGN-type activity.

IRAS 17442+6130b. The blends of Hα with [NII] λ6584, [SII](λ6716+λ6731), and Hβ are in emission. In this case, we are not sure that precisely this object is the optical counterpart of an IRAS source, because the spectrum of the neighboring, fainter galaxy, whose position closely coincides with that of the IRAS source, has not yet been obtained.

IRAS 17469+6416. There is emission in Hα, Hβ, and oxygen (N_1 and N_2) lines, as well as weak emission in [OI] λ6300 and other lines.

IRAS 17552+6209. This is a Sy2 galaxy, as implied by $R_1 \geq 0.75$ and $R_2 \gg 3$. According to Veron-Cetty and Veron (2000), the object was classified as Sy1.9 and has the redshift $z = 0.084$. Three stars fell within the spectrograph slit simultaneously with the object: two G stars 19″ and 70″ northeast and a K star 26″ southwest.

IRAS 18116+6328. Hα, a weak Hβ, and relatively strong [NII] λ6584 and [SII] λ6716, 6731 lines are in emission.

IRAS 18169+6433c,d. The two galaxies have identical spectra with $R_1 \approx 0.4$ and $R_3 \approx 0.3$. The spectrum of IRAS 18169+6433d also exhibits emission in the N_1 [OIII] λ5007 line. The object nearest IRAS 18169+6433c is a K star 16″ west of the galaxy. This star is designated as IRAS 18169+6433b in the identification lists by Mikaelian and Gigoian (1998).

IRAS 18247+6102. The ratios R_1, R_2, and R_3 (see Table 2) are indicative of AGN (LINER)-type activity. The object 29″ south of the galaxy is a K star.

CONCLUSION

In this and previous (Mikaelyan *et al.* 1998) papers, we presented our spectroscopic observations with the long-slit spectrograph of the 6-m SAO telescope as part of our comprehensive studies (Mikaelyan *et al.* 1999) of the optical counterparts of previously unidentified IR sources from the IRAS PSC catalog. We provide data for the 54 galaxies that fell within the position error ellipses of 42 IR sources.

For all objects, we determined their redshifts and computed their IR luminosities, as well as classified their spectra by using an adapted scheme. Twenty of the observed galaxies are members of groups, while the remaining galaxies are isolated objects. We found evidence for the presence of an AGN in nine of the observed galaxies: two Sy2 galaxies, four LINERs, and three Composite-type galaxies. Most of the remaining objects were classified as galaxies with H II regions at various stages of star formation.

ACKNOWLEDGMENTS

This study is based on the observations carried out with the 6-m telescope of the Special Astrophysical Observatory financially supported by the Ministry of Science of Russia (registration number 01-43).

The work was supported by the Armenian National Scientific and Educational Fund.

REFERENCES

1. V. L. Afanas'ev, A. N. Burenkov, V. V. Vlasyuk, and S. V. Drabek, Otchet SAO, No. 234 (1995).
2. J. J. Condon, W. D. Cotton, E. W. Greisen, *et al.*, Astron. J. **115**, 1693 (1998).
3. P. A. Duc, I. F. Mirabel, and J. Maza, Astron. Astrophys. **124**, 533 (1997).
4. A. V. Filippenko and W. L. W. Sargent, Astrophys. J., Suppl. Ser. **57**, 503 (1985).
5. K. B. Fisher, J. P. Huchra, M. A. Strauss, *et al.*, Astrophys. J., Suppl. Ser. **100**, 69 (1995).
6. G. H. T. Hau, H. C. Ferguson, O. Lahav, and D. Lynden-Bell, Mon. Not. R. Astron. Soc. **277**, 125 (1995).
7. T. M. Heckman, Astron. Astrophys. **87**, 142 (1980).
8. IRAS Point Source Catalog, Version 2, on the Optical Disk. Selected Astronomical Catalogs. Supplied by NASA (1989), Vol. 1.
9. H. M. Johnson and A. R. Klemola, Astrophys. J., Suppl. Ser. **63**, 701 (1987).
10. S. K. Legget, R. G. Clowes, M. Kalafi, *et al.*, Mon. Not. R. Astron. Soc. **227**, 563 (1987).
11. C. J. Lonsdale, G. Helou, J. C. Good, and W. Rice, *Catalogued Galaxies and Quasars Observed in the IRAS Survey* (Jet Populsion Laboratory, Pasadena, 1985).
12. B. E. Markarian, V. A. Lipovetski, J. A. Stepanian, *et al.*, Soobshch. Spets. Astrofiz. Obs. **62**, 5 (1989).
13. P. Massey, K. Strobel, J. V. Barnes, and E. Anderson, Astrophys. J. **328**, 315 (1988).
14. A. M. Mickaelian, S. A. Hakopian, and S. K. Balaian, in *Proceedings of the 194th IAU Symposium "Active Galactic Nuclei and Related Phenomena,"* Ed. by Y. Terzian, D. Weedman, and E. Khachikian, p. 156.
15. A. M. Mikaelian, Astrofizika **40**, 1 (1997).
16. A. M. Mikaelian, Astrofizika **43**, 425 (2000).
17. A. Mikaelian and K. S. Gigoian, Astrofizika **41**, 359 (1998).
18. A. Mikaelian, K. S. Gigoian, and D. Russeĭ, Astrofizika **40**, 581 (1997).
19. A. M. Mikaelian, S. A. Akopian, S. K. Balaian, and A. N. Burenkov, Pis'ma Astron. Zh. **24**, 736 (1998) [Astron. Lett. **24**, 635 (1998)].
20. W. Saunders, S. Oliver, O. Keeble, *et al.*, astro-ph/9909191.
21. M. A. Strauss and J. P. Huchra, Astron. J. **95**, 1602 (1988).
22. R. Terlevich, Rev. Mex. Astron. Astrofis., Ser. Conf. **6**, 1 (1997).
23. S. Veilleux and D. E. Osterbrock, Astrophys. J., Suppl. Ser. **63**, 295 (1987).
24. P. Veron, A. C. Goncalves, and M. P. Veron-Cetty, Astron. Astrophys. **319**, 52 (1997).
25. M. P. Veron-Cetty and P. Veron, ESO Sci. Rep., No. 19, 1 (2000).
26. V. V. Vlasyuk, Bull. Spec. Astrophys. Obs. **36**, 107 (1993).
27. G. Wang, R. G. Clowes, S. K. Legget, *et al.*, Mon. Not. R. Astron. Soc. **248**, 112 (1991).
28. R. D. Wolstencroft, A. Savage, R. G. Clowes, *et al.*, Mon. Not. R. Astron. Soc. **223**, 279 (1986).
29. Q. R. Yuan, Z. H. Zhu, Z. L. Yang, and X. T. He, Astron. Astrophys., Suppl. Ser. **115**, 267 (1996).

Translated by A. Dambis

Astronomy Letters, Vol. 27, No. 5, 2001, pp. 292–296. Translated from Pis'ma v Astronomicheskiĭ Zhurnal, Vol. 27, No. 5, 2001, pp. 339–344.

Cosmic-Ray Energetics in the Supernova Remnant Cassiopeia A

K. S. Stankevich* and V. P. Ivanov**

Radiophysical Research Institute, Nizhni Novgorod State University, ul. Lyadova 25/14, GSP-51, Nizhni Novgorod, 603600 Russia

Received October 18, 2000

Abstract—Based on the observed radio spectrum for the supernova remnant Cassiopeia A, we have established that it represents synchrotron radiation of relativistic electrons with a nonpower-law energy spectrum in the form of Kaplan–Tsytovich's standard distribution. The total density of relativistic electrons is 10^{-3} cm^{-3}, only 20% of which form the radio spectrum. The particle number ratio of the proton-nuclear and electron cosmic-ray components inside the shell differs significantly from the mean Galactic ratio (100) and probably does not exceed unity. © *2001 MAIK "Nauka/Interperiodica".*

Key words: *cosmic rays, nonthermal emission; supernovae and supernova remnants*

INTRODUCTION

The Galactic model for the origin of cosmic rays explains the steep part of the energy spectrum at energies below 100 TeV by considering supernova explosions and supernova remnants (SNRs) to be among their sources. Well-known considerations on energy release during supernova explosions suggest that the total power of Galactic supernovae is high enough to maintain a constant intensity of cosmic rays. The synchrotron radiation from SNRs over a wide spectral range provides direct evidence for the existence of an electron cosmic-ray component inside the SNRs. The frequency spectrum of this radiation is unambiguously determined by a power-law energy spectrum of relativistic electrons limited by minimum energies 10–50 MeV. Of particular interest is to elucidate the distribution of relativistic electrons at low energies in an effort to establish the energy distribution function and to determine the total number of relativistic electrons in the source and not only of those emitting in the radio band. This is also of importance in estimating the ratio of the electron and proton-nuclear cosmic-ray components inside SNR shells.

The proton-nuclear cosmic-ray component has not been detected experimentally. The frequency of its synchrotron radiation is too low, and it is unobservable. The SNRs were expected to be the γ-ray sources that resulted from the decay of π° mesons produced by the interaction of the proton-nuclear cosmic-ray component with matter of the swept-up shell and with matter inside the SNRs. The EGRET experiment revealed no expected γ-ray emission (Buckley *et al.* 1998). Since a clear discrepancy shows up between theory and observations, new approaches are needed to determine the intensity of the proton-nuclear cosmic-ray component in SNRs.

The energy distributions of cosmic rays can be analyzed for young powerful SNRs, because accurate absolute flux-density measurements are available for them in the entire radio range. In particular, the radio emission from the SNR Cassiopeia A has been observed for more than 50 years at many frequencies in the range 5 MHz to 250 GHz, and instantaneous spectra of the source can be reconstructed from the available sample.

INSTANTANEOUS SPECTRUM OF THE SNR CASSIOPEIA A

For our purposes, we need the entire radio spectrum from 5 MHz to millimeter waves obtained from observations at close epochs, for example, over a year. Long-term detailed absolute measurements revealed a frequency dependence of the secular decrease in flux density and of the change in spectral slope, as well as the nonstationary nature of these changes (Stankevich *et al.* 1999). Therefore, the data reduction from epoch to epoch, particularly at intervals of several years, is ambiguous, and almost simultaneously measured flux densities are required to construct the source's spectrum.

Both relative and absolute measurements have been made in such a wide frequency range, and their comparison requires reducing data to a single radioastronomical scale. We chose a radioastronomical scale that was based on the calibration of antennas by using

E-mail address for contacts: *@stnk@nirfi.sci-nnov.ru
**@ivnv@nirfi.sci-nnov.ru

1063-7737/01/2705-0292$21.00 © 2001 MAIK "Nauka/Interperiodica"

blackbody radio emission (the artificial-moon method) and that included the spectra of secondary reference sources determined in the frequency range 10 MHz to 30 GHz (Ivanov and Stankevich 1986).

The instantaneous spectrum of 1974 (see Fig. 1) gives an idea of the spectrum for the SNR Cassiopeia A. Ericson and Perley (1975) measured the flux ratio of the sources Cassiopeia A and Cygnus A at eight frequencies in the range 26 MHz ≤ ν ≤ 236 MHz. Based on the reference spectrum of Cygnus A from our absolute scale, we derived the flux densities for Cassiopeia A (see Fig. 1). At frequencies 0.5–10 GHz, we used the absolute measurements at 22 frequencies obtained by the artificial-moon method at epoch 1973.6 (Barabanov *et al.* 1986). Figure 1 shows that the spectrum contains a bend near ν = 300 MHz: the spectral index is α = 0.702 at meter waves and α = 0.809 at higher frequencies. This fact was first noted by Stankevich *et al.* (1973) and analyzed in more detail by Ivanov and Stankevich (1989). Unfortunately, there were no decameter-wave observations during 1973–1974. A complete instantaneous spectrum of Cassiopeia A was obtained only at epoch 1961, when high-quality absolute and relative measurements were made at many frequencies in the range 12 MHz to 10 GHz. The relative measurements were recalculated to flux densities based on our absolute scale and are given together with the absolute measurements in Table 1; the decameter and meter portions of the spectrum for the SNR Cassiopeia A are shown in Fig. 2.

Table 1 also includes the 1966 measurements (Parker 1968; Braude *et al.* 1968), which were reduced to epoch 1961 by taking into account the secular decrease in flux (1.1%), and the 1984–1985 absolute measurements at 5.6 and 8.9 MHz (Vinyaĭkin *et al.* 1987). The latter were not corrected for the secular decrease in flux, because no intensity variations were detected at decameter waves (Zhuk 1987; Ryabov and Serokurova 1993). The observed spectrum has a maximum near 16 MHz. The descending part of the 1961 spectrum is also represented by two spectral indices: α = 0.7 at meter waves and α = 0.8 at decameter and centimeter waves.

INTRINSIC RADIO SPECTRUM OF THE SNR CASSIOPEIA A

The observed spectrum of Cassiopeia A at frequencies below 15 MHz exhibits a turnover, which is partly attributable to the interstellar absorption of radio waves. Therefore, for the source's intrinsic spectrum to be determined, we must eliminate this absorption. The causes of the spectral turnover have been repeatedly discussed in the literature (see, e.g., Vinyaĭkin *et al.* 1987), but they have not been firmly established. There are currently enough data to bridge this gap.

Another peculiarity of the instantaneous spectrum that requires an explanation is the bend near 300 MHz.

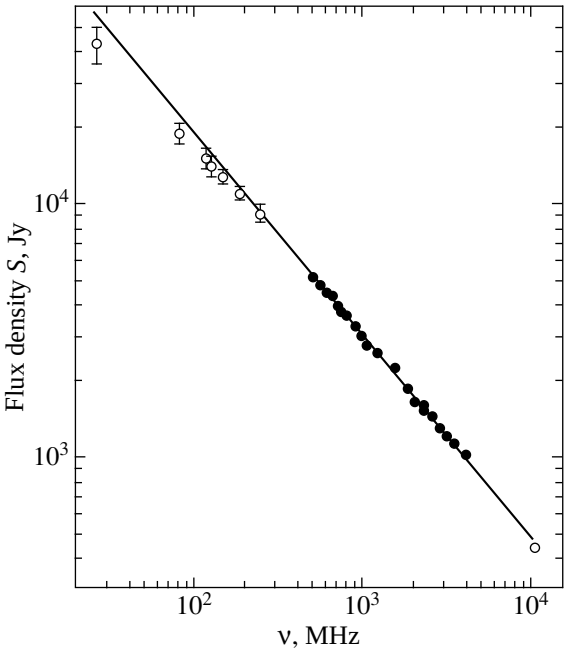

Fig. 1. Instantaneous spectrum of Cassiopeia A (1974) near the bend of the spectral index: (●) Barabanov *et al.* (1986) and (○) Ericson and Perley (1975).

In several studies, the spectrum of Cassiopeia A was represented as a continuously bending spectrum due to cosmic-ray acceleration in the course of SNR evolution (Cowsik and Sarkar 1984; Asvarov 1992). Agreement between models and observations was achieved by adjusting many free parameters. In particular, it was unjustifiably assumed that the emission with different spectral indices came from different locations in the shell.

Since the frequency spectrum for synchrotron radiation is completely determined by the energy spectrum of relativistic electrons, there must be a peculiarity in the energy distribution: the energy spectrum cannot be described by a single power-law distribution function. Kaplan and Tsytovich (1972) suggested a nonpower-law distribution function for the isotropic velocity distributions of ultrarelativistic particles,

$$N(E)dE = K_e \frac{E^2 dE}{(E_* + E)^{\gamma+2}}, \quad (1)$$

which they called a standard distribution that transforms to a power law

$$N(E)dE = K_e E^{-\gamma} dE \quad \text{at} \quad E \gg E_*. \quad (2)$$

When normalized to the total number of relativistic electrons per unit volume n_*,

$$K_e = n_* E_*^{\gamma-1} \frac{\Gamma(\gamma+2)}{2\Gamma(\gamma-1)}, \quad (3)$$

Table 1

Epoch	ν, MHz	*S*, Jy	Reference sources	Reference
1961.6	12.5	50760	Cygnus A	Braude (1965)
1961.6	16.7	57570	Cygnus A	Braude (1965)
1961.6	20	49740	Cygnus A	Braude (1965)
1961.6	24	50280	Cygnus A	Braude (1965)
1961.6	30	44370	Cygnus A	Braude (1965)
1961.6	35	38310	Cygnus A	Braude (1965)
1961.6	40	35820	Cygnus A	Braude (1965)
1961.3	13	56090	Cygnus A	Belikovich *et al*. (1967)
1961.3	25	50710	Cygnus A	Belikovich *et al*. (1967)
1961.6	240	9560	Virgo A	Conway and Moran (1964)
1961.6	412	6060	Virgo A	Conway and Moran (1964)
1961.2	750	3980	Cygnus A, Virgo A	Heeschen and Meredith (1961)
1961.1	3000	1300	Cygnus A, Virgo A	Heeschen and Meredith (1961)
1961.9	9375	507.0	Absolute scale	Stankevich (1962)
1966.9	38	36200	Absolute scale	Parker (1968)
1966.9	81.5	21100	Absolute scale	Parker (1968)
1966.5	152	12800	Absolute scale	Parker (1968)
1966.9	12.6	58500	Absolute scale	Braude *et al*. (1968)
1966.9	14.7	65000	Absolute scale	Braude *et al*. (1968)
1966.9	16.7	60000	Absolute scale	Braude *et al*. (1968)
1966.9	20	65000	Absolute scale	Braude *et al*. (1968)
1966.9	25	58000	Absolute scale	Braude *et al*. (1968)
1985.0	5.6	7000	Absolute scale	Vinyaĭkin *et al*. (1987)
1985.0	8.9	32000	Absolute scale	Vinyaĭkin *et al*. (1987)

where $\Gamma(z)$ is the gamma function. The emissivity of the system of relativistic electrons that corresponds to the distribution function (1) is

$$a_\nu d\nu = 2.1\times10^{-17}H^2 n_*\left(\frac{E_*}{mc^2}\right)^2\frac{\Gamma(\gamma+2)}{\Gamma(\gamma-1)}\frac{1}{\nu_*}\frac{\left(\frac{\nu}{\nu_*}\right)^{3/2}d\nu}{\left(1+\left(\frac{\nu}{\nu_*}\right)^{1/2}\right)^{\gamma+2}}, \quad (4)$$

where

$$\nu_* = 1.2\times10^6 H_\perp\left(\frac{E_*}{mc^2}\right)^2. \quad (5)$$

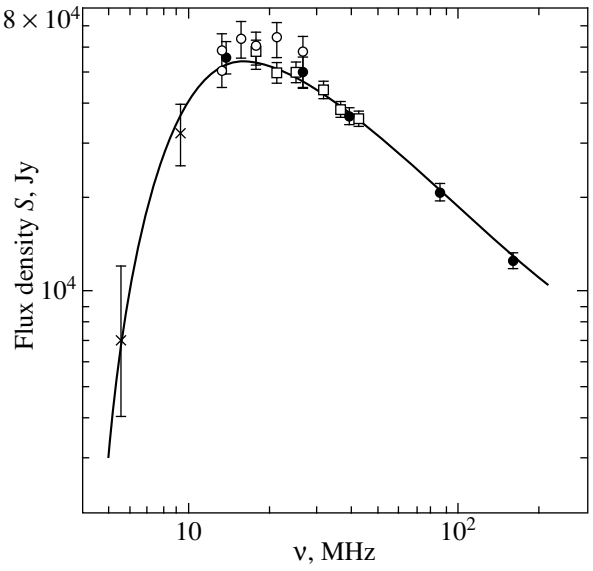

Fig. 2. Observed low-frequency spectrum of Cassiopeia A: (○) Braude (1965), (●) Belikovich *et al.* (1967), (□) Braude *et al.* (1968), and (×) Vinyaĭkin *et al.* (1987).

Using the observed radio fluxes at centimeter waves for Cassiopeia A, we obtain $K_e = 2.65\times10^{-11}$ and $\gamma = 2.6$. The mean magnetic field as inferred from polarization measurements is $H = 3\times10^{-4}$ G (Kenney and Dent 1985). The descending part of the observed spectrum with the bend at 300 MHz is fitted best at the characteristic frequency $\nu_* = 15$ kHz. In Fig. 3, the observed spectrum of the SNR Cassiopeia A is fitted by using formula (4) for the above parameters; curve *2* describes the spectrum at frequencies above the maximum. Thus, the standard energy distribution of relativistic electrons (1) can naturally explain the change in spectral index over the range.

The source's intrinsic spectrum was calculated by using formula (4) for the emissivity and by taking into account synchrotron reabsorption,

$$S_\nu = \pi\left(\frac{r}{R}\right)^2\frac{a_\nu}{\mu_\nu}\left[\int_{0.66}^{1}\left(1-e^{-2\mu_\nu r[x-\sqrt{x^2-0.437}]}\right)x\,dx + \int_{0.66}^{1}(1-e^{-2\mu_\nu rx})x\,dx\right], \quad (6)$$

where μ_ν is the coefficient of self-absorption, r is the outer shell radius, and $R = 3.4$ kpc is the distance to the source. Expression (6) is written for a model homogeneous shell with the thickness $\Delta r = 0.25r$ for $r = 1.7$ pc.

Analytic expressions for the coefficient of synchrotron reabsorption for the power-law energy spectrum (2) can be found in the literature. For the standard distribution (1), we performed numerical calculations by using a general expression for the coefficient of self-absorption (Ginzburg 1981),

$$\mu_\nu = -\frac{c^2}{4\pi\nu^2}\int P_\nu(\nu, E)E^2\frac{d}{dE}\left[\frac{N(E)}{E^2}\right]dE, \quad (7)$$

where $P_\nu(\nu, E)$ is the spectral power of the radiation from a single relativistic electron.

The intrinsic spectrum of Cassiopeia A with synchrotron self-absorption is represented by curve *3* in Fig. 3. The source's radio luminosity calculated from the intrinsic spectrum is $\Lambda = 5.8\times10^{35}$ erg s^{-1}.

Agreement with the observed spectrum (Fig. 2) was achieved by adjusting the optical depth for interstellar plasma absorption,

$$\tau_\nu = \left(\frac{\nu_T}{\nu}\right)^{2.1}, \quad (8)$$

where

$$\nu_T = 0.3(T_e^{-1.35}N_e^2 l)^{0.476} = 0.3\left(\frac{ME}{T_e^{1.35}}\right)^{0.476} \quad (9)$$

has the dimensions of frequency and is measured in GHz; l is the length in parsecs. Figure 3 shows a theoretical spectrum of the source for $\nu_T = 8.2\times10^{-3}$ GHz = 8.2 MHz (curve *4*); this spectrum is also indicated by a solid line in Fig. 2.

Assuming the ionized-gas temperature to be $T_e = 10^4$ K, we obtain the emission measure from the absorption toward Cassiopeia A, $ME = 127$ pc cm^{-6}. There are two pulsars near the source; their positions are given in Table 2. The mean electron density in the interstellar medium near the SNR Cassiopeia A can be determined from the data of Table 2, $n_e = 3.1\times10^{-2}$ cm^{-3}; the emission measure is then $ME = 3.4$ pc cm^{-6}, as might be expected. The excess emission measure $ME = 124$ pc cm^{-6} must be attributed to the H II region around the SNR, which was ionized during the explosion. According to Peimbert (1971), $ME = 740$ pc cm^{-6}. Subsequently, however, Reynolds (1983) found $ME = 20$ pc cm^{-6} and $T = 6000$ K in the H II region from H_α emission. At $T_e = 6000$ K, we obtain from formula (9) $ME = 65$ pc cm^{-6} and, in the H II region around the source, $ME = 62$ pc cm^{-6}. If the radius of the region of weak H_α emission is about 7′ (van der Bergh 1971), then the mean density of thermal electrons for $ME = 62$ pc cm^{-6} is $n_e = 3$–4 cm^{-3}, and the mass of the H II region around the SNR Cassiopeia A then exceeds $20M_\odot$. The origin of the H II region around Cassiopeia A and its association with the presupernova are the subject of a separate study.

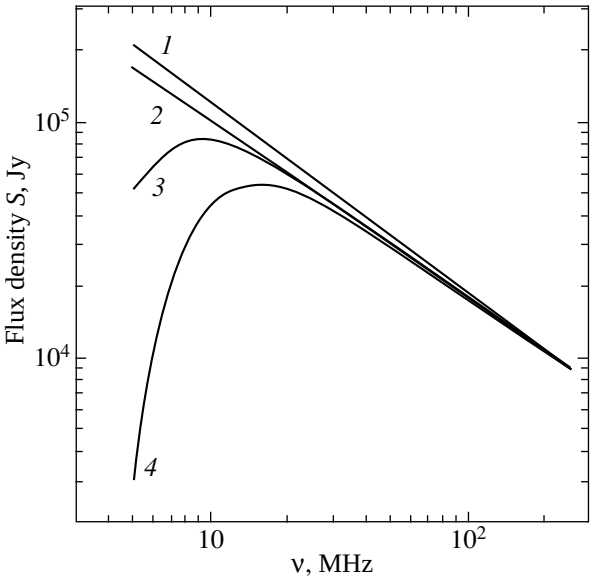

Fig. 3. Intrinsic low-frequency spectrum of Cassiopeia A. Curves *1–4* represent the flux densities for a power-law distribution function without self-absorption, a nonpower-law distribution function without self-absorption, a nonpower-law function with self-absorption, and a nonpower-law function with self-absorption and interstellar absorption, respectively.

COSMIC-RAY ENERGETICS

As we showed above, the peculiarities of the radio spectrum for the SNR Cassiopeia A result from the energy distribution of relativistic electrons (1) for the following parameters: the energy near the maximum of the distribution function $E_* = 3.3$ MeV, $\gamma = 2.6$, and $K_e = 2.65\times10^{-11}$. The purely power-law distribution (2) is formed at energies >30 MeV. It follows from formula (3) that the total number of relativistic electrons per unit volume of the shell is $n_* = 10^{-3}$ cm^{-3}, of which only 20% form the source's observed spectrum.

In Galactic cosmic rays, the electron component accounts for 1% of the number of particles of the proton-nuclear component. If this ratio also held in the cos-

Table 2

PSR	Galactic coordinates		Distance, kpc	Dispersion measure, cm^{-3} pc
	l	*b*		
2323+63	113°	2°.0	4.2	120
2424+60	112°.9	0°.0	3.4	120

mic rays inside the supernova shell, then the density of the proton-nuclear component would be $n_{cr} = 10^{-1}$ cm^{-3}. Since, according to X-ray data, the mean number of thermal plasma particles in the shell is $n_e \sim 5$ cm^{-3}, the percentage of the relativistic matter is found to be unrealistically high. The density of the proton-nuclear component must be considerably lower, probably, $n_{cr} \sim n_* = 10^{-3}$ cm^{-3}. This fact may explain the failures to detect γ-ray emission from SNRs during the EGRET experiment.

CONCLUSION

(1) The observed radio spectrum for the remnant of Supernova 1680 in the range 5 MHz to 250 GHz has several peculiarities: a change of the spectral index in the descending part of the spectrum with a bend frequency of about 300 MHz and a turnover at frequencies below 15 MHz. The intrinsic low-frequency spectrum is formed by synchrotron self-absorption and is weakened by absorption in the interstellar plasma and in the H II region around the source at frequencies below the maximum.

(2) The synchrotron radiation from Cassiopeia A is generated by relativistic electrons with a non-power-law energy distribution in the form of Kaplan–Tsytovich's standard distribution with the energy at maximum $E_* = 3.3$ MeV. The total density of relativistic electrons is 10^{-3} cm^{-3}, of which only 20% emit in radio waves.

(3) The particle number ratio of the proton-nuclear and electron cosmic-ray components inside the shell of the SNR Cassiopeia A differs significantly from its mean Galactic value (100) and, probably, does not exceed unity.

REFERENCES

1. A. I. Asvarov, Astron. Zh. **69**, 675 (1992) [Sov. Astron. **36**, 386 (1992)].
2. A. P. Barabanov, V. P. Ivanov, and K. S. Stankevich, Astron. Zh. **63**, 926 (1986) [Sov. Astron. **30**, 549 (1986)].
3. V. V. Belikovich, E. A. Benediktov, and Yu. S. Korobkov, Astron. Zh. **44**, 981 (1967).
4. S. Ya. Braude, Izv. Vyssh. Uchebn. Zaved., Radiofiz. **8**, 229 (1965).
5. S. Ya. Braude, I. N. Zhuk, S. M. Lebedeva, *et al.*, Dokl. Akad. Nauk SSSR **180**, 1323 (1968) [Sov. Phys. Dokl. **13**, 512 (1968)].
6. J. H. Buckley, C. W. Kerlof, D. A. Carter-Lewis, *et al.*, Astron. Astrophys. **329**, 639 (1998).
7. R. G. Conway and M. Moran, Mon. Not. R. Astron. Soc. **127**, 377 (1964).
8. R. Cowsik and S. Sarkar, Mon. Not. R. Astron. Soc. **207**, 745 (1984).
9. W. C. Ericson and R. A. Perley, Astron. J. (Lett.) **200**, L83 (1975).
10. V. L. Ginzburg, *Theoretical Physics and Astrophysics* (Pergamon, Oxford, 1979; Nauka, Moscow, 1981).
11. D. S. Heeschen and B. I. Meredith, NRAO Publ. **1**, 121 (1961).
12. V. P. Ivanov and K. S. Stankevich, Astron. Zh. **66**, 30 (1989) [Sov. Astron. **33**, 15 (1989)].
13. V. P. Ivanov and K. S. Stankevich, Izv. Vyssh. Uchebn. Zaved., Radiofiz. **29**, 3 (1986).
14. S. A. Kaplan and V. N. Tsytovich, *Plasma Astrophysics* (Nauka, Moscow, 1972; Pergamon, Oxford, 1974).
15. J. D. Kenney and W. A. Dent, Astrophys. J. **298**, 644 (1985).
16. E. A. Parker, Mon. Not. R. Astron. Soc. **138**, 407 (1968).
17. M. Peimbert, Astrophys. J. **170**, 261 (1971).
18. R. J. Reynolds, Astrophys. J. **268**, 698 (1983).
19. M. I. Ryabov and N. G. Serokurova, Astron. Astrophys. Trans. **4**, 29 (1993).
20. K. S. Stankevich, Astron. Zh. **39**, 610 (1962) [Sov. Astron. **6**, 480 (1962)].
21. K. S. Stankevich, V. P. Ivanov, S. A. Pelyushenko, *et al.*, Izv. Vyssh. Uchebn. Zaved., Radiofiz. **16**, 786 (1973).
22. K. S. Stankevich, V. P. Ivanov, and S. P. Stolyarov, Pis'ma Astron. Zh. **25**, 584 (1999) [Astron. Lett. **25**, 501 (1999)].
23. S. van den Bergh, Astrophys. J. **165**, 269 (1971).
24. E. N. Vinyaĭkin, V. A. Nikonov, Yu. V. Tokarev, *et al.*, Astron. Zh. **64**, 987 (1987) [Sov. Astron. **31**, 517 (1987)].
25. I. N. Zhuk, in *Proceedings of the 29th All-Union Radio-astronomy Conference* (Akad. Nauk Ést. SSR, Tallin, 1987), p. 161.

Translated by V. Astakhov

Astronomy Letters, Vol. 27, No. 5, 2001, pp. 297–303. Translated from Pis'ma v Astronomicheskiĭ Zhurnal, Vol. 27, No. 5, 2001, pp. 345–352.

The X-ray Source SLX 1732–304 in the Globular Cluster Terzan 1: The Spectral States and an X-ray Burst

M. N. Pavlinsky[1], S. A. Grebenev[1]*, A. A. Lutovinov[1], R. A. Sunyaev[1, 2], and A. V. Finoguenov[1]

[1] *Space Research Institute, Russian Academy of Sciences, Profsoyuznaya ul. 84/32, Moscow, 117810 Russia*
[2] *Max-Planck-Institut fuer Astrophysik, Karl Schwarzschild Strasse 1, 86740 Garching bei Muenchen, Germany*

Received June 29, 2000

Abstract—ART-P/Granat observations of the X-ray burster SLX 1732–304 in the globular cluster Terzan 1 are presented. The X-ray (3–20 keV) fluxes from the source differed by more than a factor of 4 during the observing sessions on September 8 ($F_X \simeq 6.95 \times 10^{-10}$ erg cm^{-2} s^{-1}) and October 6, 1990 ($F_X \simeq 1.64 \times 10^{-10}$ erg cm^{-2} s^{-1}). The intensity variations of SLX 1732–304 were apparently accompanied by variations in its hardness: whereas the source in its high state had the spectrum with a distinct exponential cutoff typical of bright low-mass X-ray binaries, its low-state spectrum could be satisfactorily described by a simple power law with a photon index $\alpha \simeq 1.7$. During the ART-P observation on September 8, a type I X-ray burst was detected from SLX 1732–304.

Key words: *neutron stars, bursters, X-ray sources, X-ray bursts, globular clusters*

INTRODUCTION

Persistent X-ray emission from the globular cluster Terzan 1 was first discovered in 1985 with the XRT telescope onboard the SPACELAB-2 space laboratory (Skinner *et al.* 1987). A flux of 1.84×10^{-10} erg cm^{-2} s^{-1} was detected in the 3-30 keV energy band. The XRT telescope was one of the first coded-aperture X-ray instruments that allowed the sky images within the field of view to be reconstructed with an angular resolution of several arcminutes. The localization with XRT showed that the new X-ray source, designated as SLX 1732–304, closely coincided in position with the cluster center. Since two X-ray bursts had been previously detected from this region with the HAKUCHO instruments (Makishima *et al.* 1981), Skinner *et al.* (1987) concluded that the discovered source was an X-ray burster, i.e., a neutron star with a weak magnetic field in a low-mass binary system. Weak X-ray emission was detected from the source with approximately the same flux during its subsequent EXOSAT (Parmar *et al.* 1989), Granat (Pavlinsky *et al.* 1995; Borrel *et al.* 1996), ROSAT (Johnston *et al.* 1995), and RXTE (Guainazzi *et al.* 1999; Molkov *et al.* 2001) observations. Only the recent BeppoSAX observations (Guainazzi *et al.* 1999), when the 2–10 keV flux from the source was a factor of ~300 lower than its normal value, constitute an exception. Of particular interest are also the ART-P/Granat observations (Pavlinsky *et al.* 1995), when the source was observed in states with different intensities and when an X-ray burst was detected from it.

Note that the distance to the globular cluster Terzan 1 has been poorly known until recently. In several studies (Skinner *et al.* 1987; Pavlinsky *et al.* 1995; Borrel *et al.* 1996), it was assumed to be $d \sim 10$ kpc. Optical observations suggested a more modest value, $d \simeq 5.9$ kpc [see Johnston *et al.* (1995) and references therein]. In general, this estimate is confirmed by recent observations of the cluster with the ESO telescopes, $d \simeq 4$–5.5 kpc (Ortolani *et al.* 1993), and with the Hubble Space Telescope, $d \simeq 5.2 \pm 0.5$ kpc (Ortolani *et al.* 1999). In our subsequent analysis, we use $d = 5.2$ kpc.

Here, we present the results of our detailed timing and spectral analyses of the ART-P/Granat observations for the X-ray source in Terzan 1 obtained in 1990–1992.

OBSERVATIONS

The ART-P telescope onboard the Granat orbiting astrophysical observatory consists of four independent modules; each module is a position-sensitive detector with a geometric area of 625 cm^2 equipped with a collimator and a coded mask whose opaque elements always cover half of the detector. The instrument has a $3.^\circ4 \times 3.^\circ6$ field of view (FWHM) and an angular resolution of $5'$ (the element size of the coded mask). Because of the detector's higher spatial resolution (~1.25 arcmin), the localization accuracy for discrete sources is several-fold higher. The telescope is sensitive to photons in the energy range 2.5–60 keV (the photon arrival time is accurate to within ~3.9 ms, and the ART-P dead time is 580 μs) and has an energy resolution of ~22% in the 5.9-keV iron line. See Sunyaev

* E-mail address for contacts: sergei@hea.iki.rssi.ru

Table 1. ART-P observations of SLX 1732–304 in 1990–1992

Date (UT)	Exposure, s	Efficiency[a]	Flux[b], mCrab	N_B^d
Sept. 8, 1990	26680	42.0	25.0 ± 1.0	1
Sept. 9, 1990	7370	2.5	107[c]	0
Oct. 6, 1990	40460	29.1	7.4 ± 1.6	0
Oct. 9, 1990	6590	4.0	72.4[c]	0
Feb. 23, 1991	3040	2.8	460[c]	1
Aug. 30, 1991	4995	3.2	300[c]	0
Sept. 19, 1991	16950	20.9	25.8[c]	0
Oct. 2, 1991	13970	13.3	39.6[c]	0
Oct. 15, 1991	7400	1.8	239[c]	1
Oct. 17, 1991	6040	4.5	219[c]	0
Oct. 18, 1991	3960	3.3	325[c]	0
Oct. 19, 1991	7920	4.1	188[c]	3
Feb. 19, 1992	24530	14.4	14.3[c]	0
Feb. 29, 1992	5360	3.0	439[c]	1
Mar. 1, 1992	4590	2.9	489[c]	0
Apr. 2, 1992	7460	2.9	392[c]	0
Apr. 3, 1992	5350	3.7	343[c]	0
Apr. 4, 1992	6700	4.0	281[c]	0
Apr. 6, 1992	6550	4.2	270[c]	0
Apr. 7, 1992	3890	4.7	316[c]	1
Apr. 8, 1992	1790	5.7	381[c]	0

[a] Collimator transmission efficiency, %.
[b] Mean 6–20 keV flux.
[c] 3σ upper limit.
[d] The number of bursts detected from sources within the field of view.

et al. (1990) for a more detailed description of the telescope.

During regular observations of the Galactic-center region, SLX 1732–304 was within the ART-P field of view many times. The total exposure was ~6.6×10^5 s. In most cases, however, the source was at the very edge of the field of view in the region where the efficiency of observations was low due to the drop in collimator transmission. Table 1 gives data only for those sessions during which the mean efficiency exceeded 1%. During a session, the telescope axis could deviate from the pointing direction within 30 arcmin because of the spacecraft wobbling, and, accordingly, the efficiency of observations could exceed its mean value during some periods. We therefore selected time intervals for the sessions listed in the table during which the instantaneous efficiency exceeded 1% and used them to determine the photon flux from the source and the actual exposure. Note that the efficiencies given in the table also refer only to the selected good parts of the sessions. The total exposure for these parts is ~2.2×10^5 s.

We see from Table 1 that in most sessions, no flux was detected from the source, and only the corresponding upper limit was obtained. Nevertheless, these sessions provide important information for the search for X-ray bursts from the source and for estimating their recurrence time. Over the entire period of observations, we detected only one burst that was unambiguously identified with SLX 1732–304. In addition, we detected nine more bursts (7 during the session described in Table 1) that we failed to localize and to identify with any source of persistent emission in the Galactic-center region (Grebenev *et al.* 2001). Based on our data, we can estimate the burst recurrence time, $11.2 < \tau < 61.1$ h (the lower limit follows from the session duration on October 6, 1990, while the upper limit follows from the total duration of observations, ~2.2×10^5 s). Since only three X-ray bursts were detected from this source for

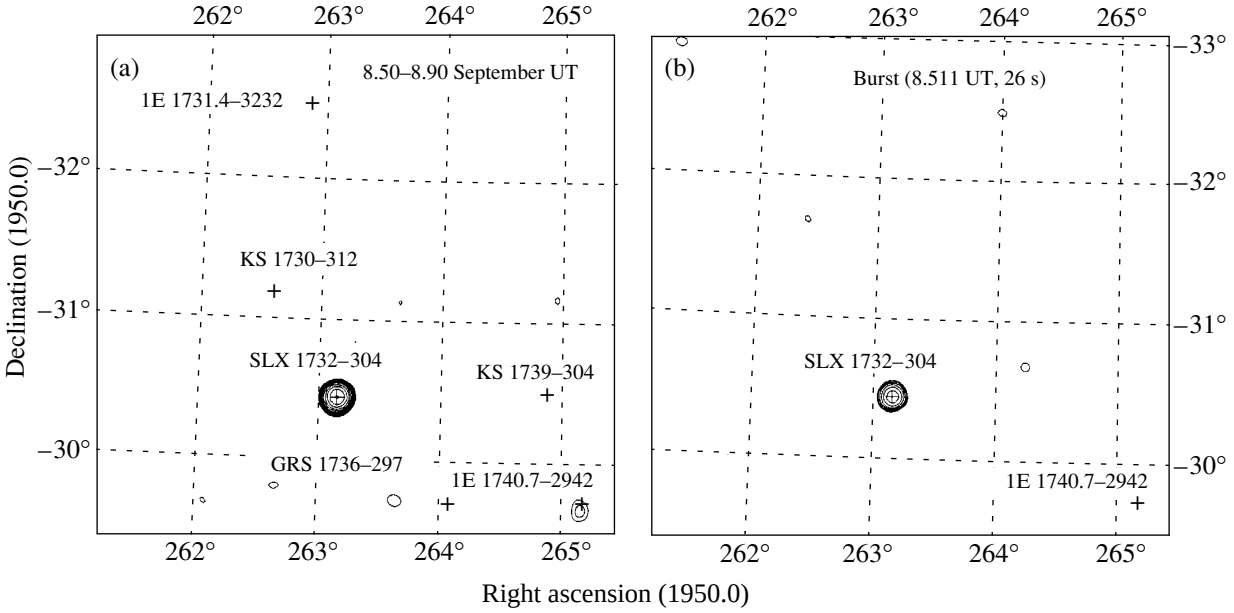

Fig. 1. ART-P 3-20 keV images of the sky region with SLX 1732–304 (a) during the entire observing session on September 8, 1990, and (b) during the burst. The 3, 4, 5, or more σ confidence regions of the source are indicated by contours.

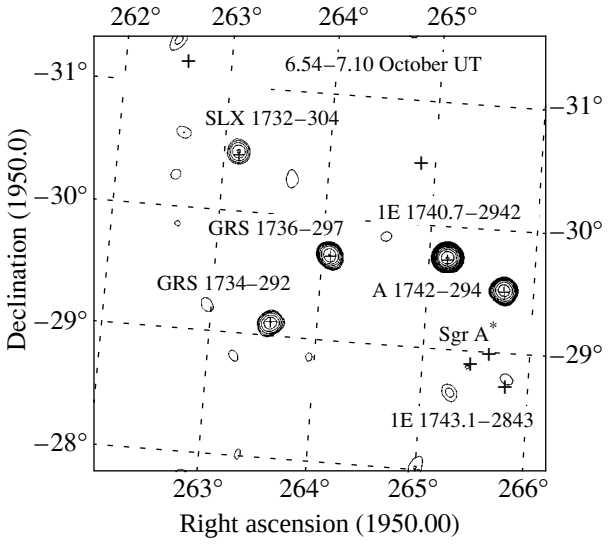

Fig. 2. ART-P 3–20 keV images of the sky region with SLX 1732–304 during the observing session on October 6, 1990. The 3, 4, 5, or more σ confidence regions of the source are indicated by contours.

over more than twenty years of its observations, τ is most likely closer to the upper limit.

A statistically significant persistent X-ray flux from the source was detected by ART-P only during two sessions: September 8 and October 6, 1990 (see Table 1). During the former observation, the flux was a factor of ~4 higher than that during the latter observation. An X-ray burst was detected from the source on September 8, 1990.

PERSISTENT SPECTRUM

The X-ray spectrum of SLX 1732–304 in quiescence can generally be described by a power law with a photon index $\alpha \sim 2.1$ modified at low energies by interstellar absorption, which corresponds to a hydrogen column density $N_H \simeq 1.8 \times 10^{22}$ cm^{-2} (Parmar *et al.* 1989; Johnston *et al.* 1995; Guainazzi *et al.* 1999; Molkov *et al.* 2001). During the ART-P observation on September 8, SLX 1732–304 was virtually the only bright source within the field of view (Fig. 1a), while the main target for the October 6 observation was the Galactic-center region (Fig. 2); apart from SLX 1732–304, there were such bright sources as A1742–294 and 1E1740.7–2942, as well as the new sources GRS 1734–292 and GRS 1736–297 within the field of view (Pavlinsky *et al.* 1992, 1994). The ART-P design allows the spectra of each object within the field of view to be measured irrespective of their number. The 3–20 keV fluxes measured on September 8 and October 6 were $(6.95 \pm 0.18) \times 10^{-10}$ erg cm^{-2} s^{-1} (28.6 ± 0.7 mCrab) and $(1.64 \pm 0.27) \times 10^{-10}$ erg cm^{-2} s^{-1} (6.7 ± 1.1 mCrab), respectively. Below, we therefore arbitrarily call the source's states during the September 8 and October 6 observations high and low, respectively. The changes in the spectrum occurred between these observations are clearly seen in Fig. 3, which shows pulse-height spectra of the source, and in Fig. 4, which shows the restored photon spectra.

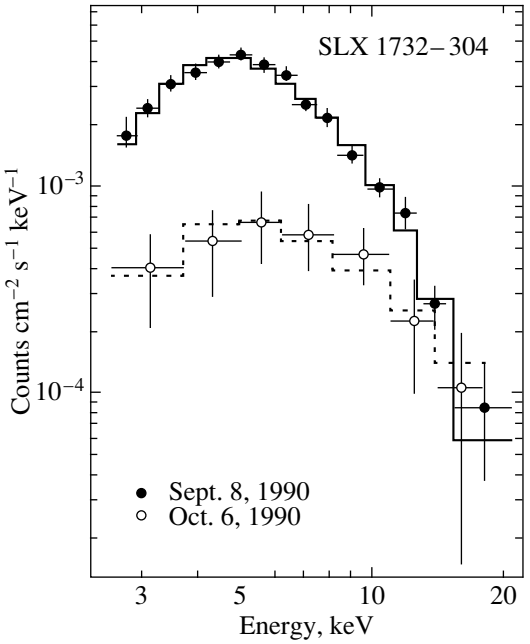

Fig. 3. Pulse-height spectra for the high (filled circles) and low (open circles) states of SLX 1732–304 on September 8 and October 6, 1990, respectively. The best fits to the spectra are indicated by histograms. The errors correspond to one standard deviation.

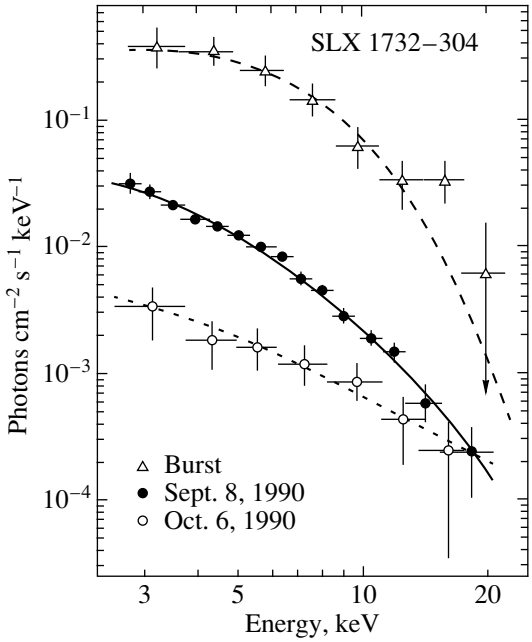

Fig. 4. Photon spectra for the high (filled circles) and low (open circles) states of SLX 1732–304 and for the X-ray burst (triangles). The solid, dotted, and dashed lines represent the corresponding model spectra. The errors correspond to one standard deviation.

Table 2. Best-fit parameters for the spectra of SLX 1732–304

Date	Model[a]	Parameters	$\chi^2_N(N)$[d]
Sept. 8, 1990	ST	$I_0^b = 0.255 \pm 0.069$	0.78(14)
		$kT_e = 2.32 \pm 0.25$ keV	
		$\tau = 7.08 \pm 1.04$	
	BR	$I_0^b = 0.217 \pm 0.012$	0.85(15)
		$kT = 6.12 \pm 0.36$ keV	
	PL	$I_0^b = 0.765 \pm 0.087$	2.52(15)
		$\alpha = 2.55 \pm 0.62$	
Oct. 6, 1990	ST	$I_0^b = 0.017 \pm 0.024$	0.08(6)
		$kT_e = 3.62 \pm 2.63$ keV	
		$\tau = 7.74 \pm 6.59$	
	BR	$I_0^b = 0.019 \pm 0.004$	0.09(7)
		$kT = 26 \pm 26$ keV	
	PL	$I_0^b = 0.029^{+0.033}_{-0.016}$	0.13(7)
		$\alpha = 1.66 \pm 0.38$	
	ST	$I_0^b = 0.106 \pm 0.004$	0.37(7)
		$N_H^c = 31 \pm 17$	
		$kT_e = 2.32$ keV	
		$\tau = 7.08$	

[a] ST for the spectrum Comptonized in a disk with electron temperature kT_e and optical depth τ, BR for bremsstrahlung with temperature kT, and PL for a power-law spectrum with photon index α.
[b] I_0 is the flux at 1 keV (phot. cm^{-2} s^{-1} keV^{-1}).
[c] N_H is the hydrogen column density ($\times 10^{22}$ cm^{-2}).
[d] The χ^2 value normalized to the number of degrees of freedom N.

Best-fit parameters for the high- and low-state spectra are listed in Table 2. The interstellar absorption toward SLX 1732–304 was fixed at $N_H = 1.8 \times 10^{22}$ cm^{-2} (Johnston *et al.* 1995). This value is in satisfactory agreement with $N_H \lesssim 2.4 \times 10^{22}$ cm^{-2} that was directly determined from ART-P data (Pavlinsky *et al.* 1995). The spectra were fitted by three models: a power law (PL), bremsstrahlung of an optically thin plasma (BR), and Comptonization of low-frequency photons in a cloud of high-temperature plasma (ST) suggested by Sunyaev and Titarchuk (1980).

As we see from Figs. 3 and 4 and from Table 2, the source's high-state spectrum exhibits a cutoff at high energies, resulting in a poor description of the spectrum by a pure power law. The ST and BR models describe the spectrum equally well; the bremsstrahlung fit yields the temperatures typical of many bright low-mass X-ray binaries, objects of the same type as that of SLX 1732–304.

Since the source's low-state spectrum was measured with large statistical errors, we cannot prefer one model to another. When this spectrum is fitted by the ST and BR models, the temperatures that characterize the steepness of the high-energy exponential cutoff are generally larger than those obtained for the high-state spectrum. This is evidence that the source's hardness increases with a transition to its low state. The best-fit parameters (see the low part of Table 2) of the low-state spectrum for the Comptonization model with fixed kT_e and τ (the same as those obtained for the high state) confirm this conclusion. The spectrum normalization I_0 and the hydrogen column density N_H, which characterizes the interstellar absorption, were taken as the free parameters. This model simulates a situation in which the transition between the states was associated with a change in intrinsic intensity of the source's radiation (without any change in spectral shape) or with the emergence of a scattering and absorbing cloud of cold plasma on the line of sight. Although both these possibilities cannot be completely rejected, we see that this model describes the pulse-height spectrum worst. The long-term SIGMA/Granat observations of SLX 1732–304 (Pavlinsky *et al.* 1995; Borrel *et al.* 1996) also indicate that the source has a hard Comptonized spectrum in its low state.

In Figs. 3 and 4, the solid and dashed lines represent the best fits to the source's high- and low-state spectra with the Comptonization model. According to the ART-P data, the source's mean 3–20 keV luminosity during these states was 2.25×10^{36} and 5.3×10^{35} erg s^{-1}, respectively.

X-RAY BURST

During the September 8, 1990 observation at $12^h16^m18^s$ (UT), ART-P detected an intense X-ray burst (Fig. 5). Its localization showed that the position of the burst source, R.A. = $17^h32^m34^s$ and Decl. = $-30°29'26''$ (Pavlinsky *et al.* 1994), coincides, within the error limits ($120''$ at 90% confidence), with the position of SLX 1732–304. Our result is illustrated by Fig. 1b, which shows an X-ray (3–20 keV) map of the sky within the ART-P field of view during the first 26 s of the burst. It is of interest to compare it with a similar map obtained during the entire observing session on September 8 (see Fig. 1a).

The time profile of the burst (an insert in Fig. 5) indicates that it belongs to type I bursts, which are produced by a thermonuclear explosion on the neutron-star surface and which are characterized by an abrupt rise followed by a slow exponential decline in X-ray flux.

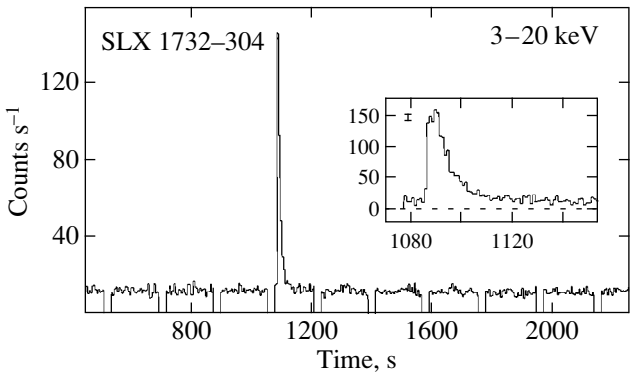

Fig. 5. Observed light curve of SLX 1732–304 on September 8, 1990. The insert shows the X-ray burst with the highest time resolution. Time t from the beginning of the session is plotted along the horizontal axis.

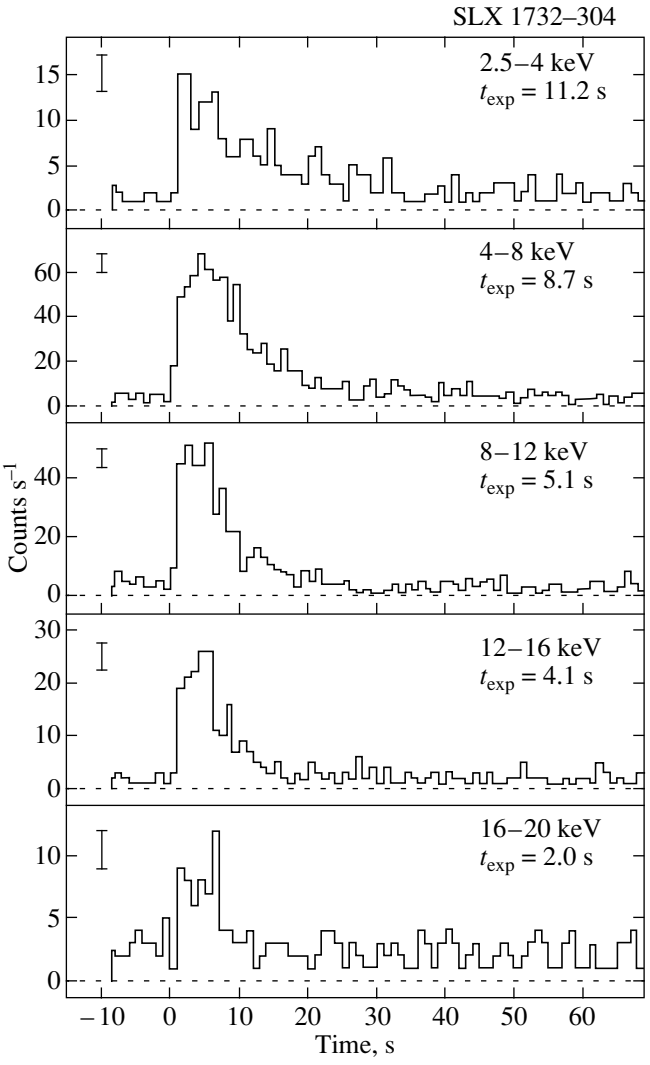

Fig. 6. Profiles of the X-ray burst in different energy bands with a time resolution of 1 s; t_{exp} is the e-folding decline time of the source in each band. The errors correspond to one standard deviation.

A distinctive feature of type I bursts is the so-called "cooling" of the radiation at the burst exponential stage, i.e., a gradual softening of the spectrum and a decrease in e-folding decline time with increasing energy. The burst time profiles in Fig. 6 and the corresponding e-folding times of exponential decline t_{exp} show that the cooling state is well defined in this case.

Figures 4 (triangles) and 7 (filled and open circles) show three photon spectra measured during the burst: the spectrum averaged over the entire burst time (~26 s), the spectrum near peak flux (3–5 s after the burst onset), and the spectrum at the end of the cooling stage (13–16 s). The dashed, solid, and dotted lines represent the best fits to these spectra with the blackbody model. Figure 7 clearly shows that the spectrum appreciably softens by the end of the burst. To better trace the spectral evolution, we singled out seven intervals in the burst profile and performed a spectral analysis for each of them. The best-fit parameters for each spectrum with the model of a blackbody sphere and the corresponding X-ray (3–20 keV) flux are given in Table 3. The spectrum averaged over the entire burst time can be described by the model of a blackbody sphere with temperature $kT_{bb} \simeq 1.83 \pm 0.17$ keV, radius $R_{bb} \simeq 6.6 \pm 1.2$ km, and the 3–20 keV flux $F \simeq (1.92 \pm 0.19) \times 10^{-8}$ erg cm^{-2} s^{-1}, which corresponds to a luminosity $L_X \simeq 6.2 \times 10^{37}$ erg s^{-1}. Note that the blackbody

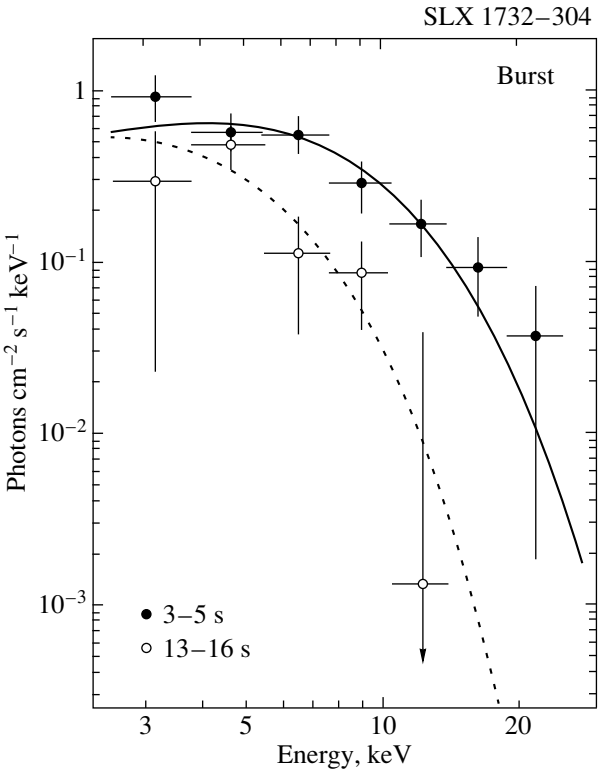

Fig. 7. Measured photon spectra of SLX 1732–304 at the burst peak (filled circles) and the end of the cooling stage (open circles). The solid and dotted lines represent the corresponding model spectra.

Table 3. Spectral evolution of SLX 1732–304 during the X-ray burst

Interval, s[a]	Flux[b], mCrab	kT_{bb}, keV	R_{bb}, km	χ^2_N (N)[c]
0–2	904 ± 272	3.84 ± 1.17	1.88 ± 1.02	0.43 (8)
3–5	2470 ± 340	2.49 ± 0.33	6.43 ± 1.59	1.43 (8)
6–8	1549 ± 281	1.98 ± 0.33	7.80 ± 2.63	0.66 (8)
9–12	535 ± 236	1.77 ± 0.55	6.38 ± 4.21	0.10 (5)
13–16	578 ± 163	1.38 ± 0.40	9.76 ± 3.53	0.84 (5)
17–24	178 ± 86	1.00 ± 0.39	13.74 ± 14.74	1.45 (8)

[a] From the burst onset at $12^h16^m18^s$ (UT).
[b] The 3–20-keV flux.
[c] The χ^2 value normalized to the number of degrees of freedom N.

model does not satisfactorily describe the measured burst spectrum at hard ($h\nu \gtrsim 18$ keV) energies (see Fig. 4).

Figure 8 shows the evolution of the source's bolometric luminosity L_{bb}, radius R_{bb}, and temperature kT_{bb} during the burst in the blackbody model. The radius R_{bb} is almost always smaller than the typical neutron-star radius, $R_{ns} \simeq 15$ km, suggesting that the thermonuclear explosion responsible for the burst took place not instantaneously over the entire neutron-star surface, but only in its part. However, a much more probable reason is the oversimplified description of the measured spectra. As was first shown by Sunyaev and Titarchuk (1986) and Ebisuzaki and Nomoto (1986), the Comptonized spectra of the radiation emerging from the photospheres of X-ray bursters during bursts can differ markedly from Planck spectra. In particular, the Wien radiation component with a temperature corresponding to the electron temperature of the outer photosphere, which can be higher than the effective (blackbody) temperature, dominates in the X-ray band.

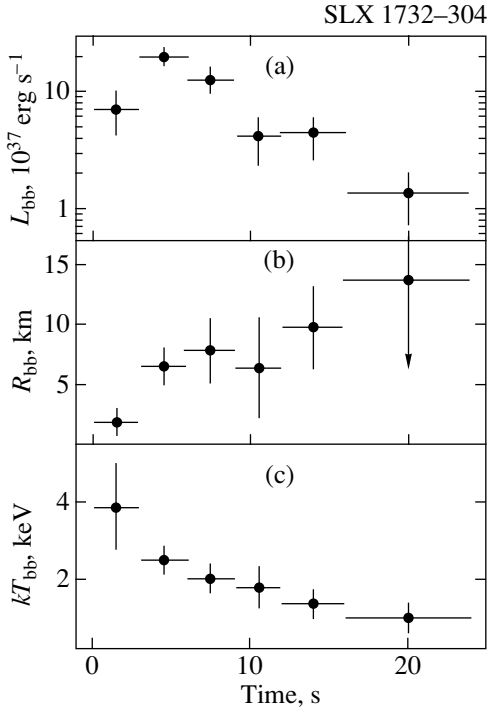

Fig. 8. Evolution of (a) the source's bolometric luminosity, (b) its radius, and (c) the blackbody temperature during the X-ray burst detected by ART-P.

CONCLUSION

The ART-P observations of the X-ray burster SLX 1732–304 in the globular cluster Terzan 1 are unique not only because the source was detected during them in states with different intensities, but also because, for the first time, it has become possible to carry out a detailed spectral study of the evolution of its radiation during an X-ray burst.

Our analysis shows that the transition between the high and low states was apparently accompanied by a change in the source's hardness. In its high state, the spectrum of the source was typical of bright low-mass X-ray binaries whose compact object is a neutron star with a weak magnetic field. It could be satisfactorily described by bremsstrahlung of an optically thin thermal plasma with $kT \sim 6$ keV or, equally well, by Comptonization of low-frequency photons in a cloud of hot ($kT_e \sim 2.3$ keV) electron plasma. In its low state, the source in the ART-P energy band most likely had a power-law spectrum with no evidence of a clear high-energy cutoff. This means that the emission from the source in this state originates in much hotter and more tenuous plasma.

The X-ray burst observed with ART-P on September 8 became the third burst detected from this source over the entire period of its observations. Our analysis shows that it is a classical type I burst; i.e., it is characterized by an abrupt rise in flux followed by a slow exponential decline, with the decline at hard energies ($t_{exp} \simeq 2$ s) being faster than that at soft energies ($t_{exp} \simeq 11$ s). Our study of the source's spectrum during the burst indicates that it can be satisfactorily described by the model of a blackbody with a temperature smoothly falling during the burst from 3.8 to 1.0 keV. The total energy release during the burst is $E \simeq 1.7 \times 10^{39}$ erg, which is equivalent to an explosion of $M \simeq E/\epsilon_N \simeq 9.5 \times 10^{20}$ g of matter, where $\epsilon_N \simeq 0.002c^2$ is the helium burning efficiency. If we use an estimate for the rate of accretion onto the neutron star in quiescence ($\dot{M} = L_X R_{ns}/GM_{ns}$, where L_X, $M_{ns} \simeq 1.4M_\odot$, and $R_{ns} \simeq 15$ km are the luminosity, mass, and radius of the neutron star, respectively), then we can estimate the time it takes for this amount of matter to be accreted onto the stellar surface, i.e., the characteristic burst recurrence time: $\tau \simeq 14.8$ h during the high state and $\tau \simeq 62.7$ h during the low state. When comparing these estimates with the duration of the source's ART-P observations in its high and low

states (see Table 1), the burst detection in the former case and its absence in the latter case seems natural. However, one should not attach too great a significance to these estimates. Many bright X-ray sources are known to show up as bursters only in a state with a certain (usually moderately high) luminosity (Lewin *et al.* 1993; Molkov *et al.* 1999). In this sense, the observation of the burst from SLX 1732–304 in its high state provides further evidence that this source is exceptional and unique among X-ray bursters.

ACKNOWLEDGMENTS

This study was supported by the Russian Foundation for Basic Research (project nos. 98-02-17056, 99-02-18178, and 00-15-99297). We wish to thank K.G. Sukhanov, flight director, the staffs of the Lavochkin Research and Production Center, RNIIKP, and the Deep Space Communications Center in Evpatoria, the Evpatoria team of the Space Research Institute (Russian Academy of Sciences), the team of I.D. Tserenin, and B.S. Novikov, S.V. Blagiĭ, A.N. Bogomolov, V.I. Evgenov, N.G. Khavenson, and A.V. D'yachkov from the Space Research Institute who operated the Granat Observatory, provided the scientific planning of the mission, and performed a preliminary processing of telemetry data. We also wish to thank the team of M.N. Pavlinsky (Space Research Institute) and the staff of the former Research and Development Center of the Space Research Institute in Bishkek who designed and manufactured the ART-P telescope.

REFERENCES

1. V. Borrel, L. Bouchet, E. Jourdan, *et al.*, Astrophys. J. **462**, 754 (1996).
2. T. Ebisuzaki and K. Nomoto, Astrophys. J. Lett. **305**, L67 (1986).
3. S. A. Grebenev, A. A. Lutovinov, M. N. Pavlinsky, *et al.*, Pis'ma Astron. Zh. **27**, 423 (2001) [Astron. Lett. **27** (2001) (in press)]; Preprint No. 2031, IKI RAN (Space Research Institute, Russian Academy of Sciences, Moscow, 2000).
4. M. Guainazzi, A. Parmar, and T. Oosterbroek, Astron. Astrophys. **349**, 819 (1999).
5. H. Johnston, F. Verbunt, and G. Hasinger, Astron. Astrophys. **298**, L21 (1995).
6. W. Lewin, J. van Paradijs, and R. Taam, Space Sci. Rev. **62**, 223 (1993).
7. K. Makishima, T. Ohashi, H. Inoue, *et al.*, Astrophys. J. Lett. **247**, L23 (1981).
8. S. V. Molkov, S. A. Grebenev, M. N. Pavlinsky, and R. A. Sunyaev, Astrophys. Lett. Commun. **38**, 141 (1999); astro-ph/9903089.
9. S. V. Molkov, S. A. Grebenev, and A. A. Lutovinov, Pis'ma Astron. Zh. **27** (2001) (in press) [Astron. Lett. **27** (2001) (in press)].
10. S. Ortolani, B. Barbuy, E. Bica, *et al.*, Astron. Astrophys. **350**, 840 (1999).
11. S. Ortolani, E. Bica, and B. Barbuy, Astron. Astrophys. **267**, 66 (1993).
12. A. Parmar, L. Stella, and P. Giommi, Astron. Astrophys. **222**, 96 (1989).
13. M. N. Pavlinsky, S. A. Grebenev, and R. A. Sunyaev, Pis'ma Astron. Zh. **18**, 217 (1992) [Sov. Astron. Lett. **18**, 88 (1992)].
14. M. N. Pavlinsky, S. A. Grebenev, and R. A. Sunyaev, Astrophys. J. **425**, 110 (1994).
15. M. Pavlinsky, S. Grebenev, A. Finogenov, and R. Sunyaev, Adv. Space Res. **16** (3), 95 (1995).
16. G. Skinner, A. Willmore, C. Eyles, *et al.*, Nature **330**, 544 (1987).
17. R. A. Sunyaev and L. G. Titarchuk, Astron. Astrophys. **86**, 121 (1980).
18. R. A. Sunyaev, S. I. Babichenko, D. A. Goganov, *et al.*, Adv. Space Res. **10** (2), 233 (1990).
19. R. A. Sunyaev and L. G. Titarchuk, Pis'ma Astron. Zh. **12**, 857 (1986) [Sov. Astron. Lett. **12**, 359 (1986)].

Translated by V. Astakhov

Astronomy Letters, Vol. 27, No. 5, 2001, pp. 304–312. Translated from Pis'ma v Astronomicheskiĭ Zhurnal, Vol. 27, No. 5, 2001, pp. 353–362.

General-Relativistic Curvature of Pulsar Vortex Structure

A. A. Shatskiĭ*

Moscow State University, Vorob'evy gory, Moscow, 119899 Russia

Received July 3, 2000; in final form, October 6, 2000

Abstract—The motion of a neutron superfluid condensate in a pulsar is studied. Several theorems of general-relativistic hydrodynamics are proved for a superfluid. The average density distribution of vortex lines in pulsars and their general-relativistic curvature are derived. *© 2001 MAIK "Nauka/Interperiodica".*

Key words: *pulsars*

1. INTRODUCTION

The superfluidity of matter in rotating neutron stars combines with the closeness of their gravitational $\left(r_g = \frac{2GM}{c^2}\right)$ and geometrical (R) radii, where G is the gravitational constant, c is the speed of light, and M is the neutron-star mass (see, e.g., Manchester and Taylor 1980). Therefore, general-relativistic effects can appreciably affect the processes in the superfluid cores of pulsars and the mechanisms of glitches. In this regard, Andreev *et al.* (1995) discussed low angular velocities in general relativity: $\Omega < \Omega_c \sim \hbar/(m^*R^2)$, where m^* is the mass of a superfluid condensate particle (a Cooper pair), $\Omega \sim \Omega_c$ (see Kirzhnits and Yudin 1995), and the number of vortex lines (VLs) is 0 and 1, respectively.

Here, we deal with the realistic, opposite case,

$$\Omega_c \ll \Omega < c/R, \tag{1}$$

when there is a dense system of VLs. Recently, the interest in this problem has risen dramatically, which is most likely attributable to an increase in the accuracy of measuring glitches in pulsars. Consequently, it becomes possible to detect in principle post-Newton gravimagnetic effects in pulsars, which are described below. See, e.g., Prix (2000) and Langlois (2000) for an overview of this subject. Here, we propose a method of solving the problem in question that slightly differs from that proposed by these authors.

Bekarevich and Khalatnikov (1961) proved that rigid-body rotation is stable in the nonrelativistic case, and that VLs are rectilinear and distributed at a constant density. Because of general-relativistic gravielectric and gravimagnetic effects, which are determined, respectively, by $\nabla g_{\alpha\beta}$ and curl rot$\mathbf{g}$ [by the definition of Landau and Lifshitz (1988b), $\mathbf{g} = \{-g_{0\alpha}/g_{00}\}$ and g_{ik} is the metric tensor], differential rotation becomes stable (to be more precise, this rotation is stable dynamically, while rigid-body rotation is stable kinematically as before; see below). In this case, VLs curve and are redistributed in space. These effects are described below.

2. ANALYZING CHANGES IN THE SYSTEM WHEN AN ORDINARY FLUID IS REPLACED WITH A QUANTUM, FERMI SUPERFLUID

2.1. General Relations for a Superfluid Condensate in General Relativity

The wave function of a superfluid condensate is known (see, e.g., Bekarevich and Khalatnikov 1961) to be

$$\psi = \nu\exp(i\phi).$$

Given the identity u $u_i u^i = 1$,[1] the generalization of the nonrelativistic relation $\mathbf{v} = \frac{\hbar}{m^*}\nabla\phi$ to general relativity is

$$u_i = \frac{\partial_i\phi}{k}, \quad k^2 = \partial_i\phi\partial^i\phi. \tag{2}$$

Indeed, let us derive an expression for a general-relativistic superfluid current $j_i = nu_i$[2] with the continuity equation $j_i^{;i} = j^i_{;i} = 0$.

[1] The indices i, j, k, l, m, and n run the series 0, 1, 2, and 3; the indices α, β, and γ run the series 1, 2, and 3.

[2] We introduce the notation in which the scalar densities ε, p, $\omega = p + \varepsilon$, and n are identified with their eigenvalues (i.e., with the values in a commoving frame of reference), respectively: the energy density, pressure, thermal function, and density of the particles; u_i are the components of the 4-velocity vector for the matter.

* E-mail address for contacts: bruk@lpi.ru

Let us write the Lagrangian of a superfluid condensate in general relativity by using the Madelung hydrodynamic representation (see Grib *et al.* 1980; Bogolyubov and Shirkov 1993):

$$L = \frac{1}{2}\psi^*_{;i}\psi^{;i} + |\psi|^2\tilde{F}(|\psi|^2) = \frac{1}{2}\nu^2\partial_i\phi\partial^i\phi + \nu^2 F(\nu^2). \quad (3)$$

The principle of least action relative to a change in ϕ yields

$$(\nu^2\partial^i\phi)_{;i} = 0. \quad (4)$$

Consequently, the current vector is $j^i = nu^i = \text{const} \cdot \nu^2\partial^i\phi$. This is seen from a comparison of j^i and j^i_{sf} in the nonrelativistic case: $u^i = v^i/c$ and $j^i = nv^i/c$. For a superfluid, we write $n = \nu^2$, $v^i = \frac{\hbar}{m^*}\partial^i\phi$, and $j^i_{sf} = \frac{\hbar}{m^*c}\nu^2\partial^i\phi$. Since the continuity equation $j^i_{;i} = 0$ must hold in any case, we derive Eq. (4) for a superfluid. Hence, we obtain for a superfluid current in general relativity

$$j^i = \frac{\hbar}{m^*c}\nu^2\partial^i\phi = nu^i \quad (5)$$

or, for covariant quantities,

$$j_i = \frac{\hbar}{m^*c}\nu^2\partial_i\phi = nu_i. \quad (6)$$

A scalar multiplication of the latter expression by Eq. (5) yields

$$\left(\frac{\hbar}{m^*c}\right)^2\nu^4\partial^i\phi\partial_i\phi = n^2.$$

Expression (2) follows from this.

In the Newton approximation, $k^2 \approx (m^*c/\hbar)^2$. The scalar k is identified with $\omega/(nc\hbar)$ (see subsection 2.2). Hence, since $\nu^2 \approx n$ in the Newton approximation, Eq. (6) or (2) yields

$$u_i \approx \frac{\hbar}{m^*c}\partial_i\phi. \quad (7)$$

In seeking to approach an optimum regime, a superfluid current undergoes a well-known rearrangement (see Bekarevich and Khalatnikov 1961). As a result, while the current remains potentially almost everywhere, vorticity arises, which generally coincides with the vorticity for an ordinary (nonsuperfluid) fluid at the same point. This occurs, because a system of VLs is formed, with the phase of the wave function $\phi = \varphi + f(t)$ corresponding to each of them.[3] According to (7), we then have for a single vortex

$$u_\varphi \approx \frac{\hbar}{m^*c}. \quad (8)$$

[3] In what follows, we use a cylindrical coordinate system with the z axis directed along the spin axis: $x^{0,1,2,3} = ct, \rho, \varphi$, and z.

On the vortex axis itself, where ϕ is uncertain, the wave function loses its meaning, and the superfluidity vanishes. This corresponds to a physically nonsuperfluid VL core of a macroscopically small radius, which is responsible for the nonzero curl of velocity (see Bekarevich and Khalatnikov 1961).

The above reasoning is universal and equally applies to the nonrelativistic and general-relativistic cases.

2.2. The General-Relativistic Bernoulli Theorem

For the subsequent analysis of a superfluid in general relativity, we need the general-relativistic Bernoulli theorem.

The classical Bernoulli theorem is derived for a steady, isentropic fluid flow from the Euler hydrodynamic equations (see Landau and Lifshitz 1988a):

$$\frac{\partial\mathbf{V}}{\partial t} + (\mathbf{V}\nabla)\mathbf{V} = -\nabla\frac{\omega}{mn}.$$

In the relativistic case, these equations can be written as

$$u^i\partial_i(k^*u_j) = \partial_j k^*, \quad (9)$$

where $k^* = \frac{\omega}{n}$. Note that these equations have a particular solution of the form $k^*u_j = \text{const} \cdot \partial_j\phi$, where ϕ is a scalar function of the coordinates. Therefore, in contrast to the nonrelativistic case, the quantity k^*u_j rather than the velocity has the potential. Hence, according to (2), we immediately identify k^* for a superfluid with $\hbar ck$:

$$k^* = \frac{\omega}{n} = \hbar ck. \quad (10)$$

In general relativity, ∂_j is replaced with the covariant derivative ∇_j:

$$u^i\nabla_i(k^*u_j) = \nabla_j k^* \quad (11)$$

or, expanding the covariant derivative,

$$u^i\partial_i(k^*u_j) - u^i\Gamma^m_{ij}k^*u_m = \partial_j k^*.$$

Substituting the expressions for the Christoffel symbols in this relation,

$$\Gamma^m_{ij} = \frac{1}{2}g^{mn}(\partial_i g_{jn} + \partial_j g_{in} - \partial_n g_{ij}), \quad (12)$$

yields

$$u^i\partial_i(k^*u_j) - \frac{1}{2}k^*u^iu^n\partial_j g_{in} = \partial_j k^*. \quad (13)$$

Denoting

$$\phi_j = \partial_j\phi = ku_j; \quad \phi^j = \partial^j\phi = ku^j, \quad (14)$$

we obtain for a superfluid

$$\phi^i\partial_i\phi_j - \frac{1}{2}\phi^i\phi^n\partial_j g_{in} = \frac{1}{2}\partial_j k^2. \quad (15)$$

In that case, since $k^2 = g_{in}\phi^n\phi^i$, we derive two equations,

$$\phi^\alpha[\partial_\alpha\phi_0 - \partial_0\phi_\alpha] = 0 \quad (16)$$

and

$$\phi^\alpha[\partial_\alpha\phi_\gamma - \partial_\gamma\phi_\alpha] + \phi^0[\partial_0\phi_\gamma - \partial_\gamma\phi_0] = 0. \quad (17)$$

The former follows from the latter. Denoting

$$\sigma_{\alpha\gamma} = \frac{1}{2\pi}[\partial_\alpha\phi_\gamma - \partial_\gamma\phi_\alpha], \quad (18)$$

we obtain for $\sigma_{\alpha\gamma}$[4]:

$$\sigma_{\alpha\gamma} = \frac{\phi^0}{2\pi\phi^\beta\phi_\beta}[\phi_\alpha\partial_\gamma\phi_0 - \phi_\gamma\partial_\alpha\phi_0 + \phi_\gamma\partial_0\phi_\alpha - \phi_\alpha\partial_0\phi_\gamma]. \quad (19)$$

We emphasize that our system is not axially symmetric because it contains vortices, but this symmetry is restored by averaging over the VL distribution. As a result, there is no steady state in this case. Clearly, an infinite number of stationary frames of references exist for an ordinary fluid uniformly rotating in a vessel. Below, we show that there is a (unique) frame of reference for a rotating superfluid comoving with VL cores in which all quantities are stationary. For this frame of reference, we derive from (17) $\sigma_{\alpha\gamma} = 0$ on all current lines where $\partial_\gamma\phi_0' = 0$[5] ($\partial_\gamma$ in any direction). Therefore,

$$ku_0' = \phi_0' = \text{const}. \quad (20)$$

This is the general-relativistic analog of the Bernoulli theorem. In the nonrelativistic limit (see Landau and Lifshitz 1988a):

$$k = \frac{1}{\hbar c}\frac{\omega}{n} \longrightarrow \frac{m^*c}{\hbar}\left(1 + \frac{p}{\tilde{\rho}c^2}\right),$$

$$u_0 = \sqrt{\frac{g_{00}}{1 - v^2/c^2}} \longrightarrow \left(1 + \frac{\tilde{\varphi}}{c^2}\right)\left(1 + \frac{v^2}{2c^2}\right) \longrightarrow 1 + \frac{\tilde{\varphi}}{c^2} + \frac{v^2}{2c^2},$$

$$\text{hence } ku_0 \longrightarrow \frac{m^*c}{\hbar}\left(1 + \frac{\tilde{\varphi} + v^2/2 + p/\tilde{\rho}}{c^2}\right) = \text{const},$$

where $\tilde{\varphi}$ and $\tilde{\rho}$ are the Newton gravitational potential and the matter density, respectively. This is the ordinary Bernoulli theorem.

For a rotating superfluid with vortices, the laboratory frame of reference ceases to be stationary, but we can choose a frame of reference for a rotating superfluid that comoves with VL cores; in this case, the frame of reference is stationary and does not comove with the superfluid.

3. DETERMINING THE RELATIONSHIP BETWEEN DYNAMICAL SUPERFLUID PARAMETERS

3.1. The Principle of Least Action for a Rotating Superfluid in General Relativity

Hartl and Sharp (1967) proved that rigid-body rotation with an angular velocity equal to the shell angular velocity is most favorable for an ideal, ordinary fluid in general relativity.

Let us prove that this assertion remains also valid for a superfluid.[6]

In view of the general-relativistic Bernoulli theorem and by analogy with the study of Hartl and Sharp (1967) for an ordinary fluid, we assume the spatial components $\partial_\gamma\phi$ and the probability density ν^2 for a condensate particle to be detected at a given point to be independent variables for superfluid dynamics. In addition, we will remember that x_k are the variables that determine the vortex shape and coordinates, while the metric components g_{ik} are the variables that determine the system's gravitational field.

Given the conservation of momentum and the total number of particles, the expression for the total energy of a superfluid can be written as (Hartl and Sharp 1967)

$$\tilde{L} = \nu^2\phi_0\phi^0 - \nu^2[F + k^2/2] - \Omega\left(-\frac{1}{c}\nu^2\phi^0\phi_\varphi\right) - \mu\nu^2\phi^0, \quad (21)$$

where Ω and μ are the corresponding Lagrange factors.

In addition, we must take into account the Lagrangian L_0 of the shell. Given momentum conservation, the analog of (21) for the shell can be written as

$$\tilde{L}_0 = J_0\Omega_0^2/2 - \Omega J_0\Omega_0,$$

where J_0 and Ω_0 are the moment of inertia and angular velocity of the shell in the frame of reference under

[4] Since the condensate ceases to exist on vortex lines, the concept of phase loses its meaning; thus, the theorem on the curl of a gradient ceases to be valid on vortex cores, and the 4-gradient of phase $\partial_i\phi$ is replaced with a 4-vector ϕ_i.

[5] The prime means that the quantities under consideration refer to a stationary frame of reference outside VL cores.

[6] By the angular velocity of a superfluid, we imply the mean value of $\frac{u^\varphi}{cu^0}$ averaged over the surface orthogonal to the vortex direction near the point under consideration whose area is much smaller than the system's cross-sectional area, but, at the same time, is still much larger than the square of the mean separation between vortices. As we show below, this condition can definitely be satisfied for pulsars.

consideration, respectively. Varying over Ω_0 leads to the equality

$$\Omega = \Omega_0.$$

If, however, the satisfaction of the general-relativistic potentiality condition for a superfluid flow must also be taken into account, then, according to the general rules for imposing additional conditions, we must add the term $\Delta\tilde{L}$ to $\tilde{L}$ to express the fact that the circulation of the phase gradient over a closed contour is proportional to the number of vortices crossing this contour. This is the general-relativistic generalization of the potentiality condition for a superfluid flow:

$$\oint_\Gamma \partial_\gamma \phi dx^\gamma = \int_\Gamma (\partial_\beta\partial_\gamma\phi - \partial_\gamma\partial_\beta\phi) dx^\beta \wedge dx^\gamma = 2\pi K, \quad (22)$$

where $dx^\beta \wedge dx^\gamma$ is the directed surface element pulled over contour Γ, and K is the number of vortices crossing the contour. Thus, the general-relativistic potentiality condition, according to (18), can be written as

$$2\pi\sigma_{\beta\gamma} = \sum_{k=1}^{N} 2\pi n^k_{\beta\gamma}\delta^2(x - x_k), \quad (23)$$

while the addition to $\tilde{L}$ corresponding to this condition can be written as

$$\Delta\tilde{L} = \xi^{\beta\gamma}(x)\left[2\pi\sigma_{\beta\gamma} - \sum_{k=1}^{N} 2\pi n^k_{\beta\gamma}\delta^2(x - x_k)\right]. \quad (24)$$

Here, according to (18), $2\pi\sigma_{\beta\gamma}$ is the curl of ϕ_γ; $n^k_{\beta\gamma}$ is a unit antisymmetric tensor dual to one of the surfaces which are orthogonal to the vectors of the vortex direction at each point, $n^k_{\beta\gamma}$ is defined at the point of intersection of this surface with vortex k, and the summation over k is performed over all vortices in the system;[7] $\delta^2(x - x_k)$ is the bivariate delta function, and x is the radius vector defined on this surface; and the antisymmetric tensor $\xi^{\beta\gamma}(x)$ is the Lagrange functional factor.

3.2. Determining the Relationship between the Components of the 4-Gradient of Phase for a Superfluid Condensate

Action A in general relativity is known to be related to Lagrangian L by

$$A = \int L dX, \quad dX = \sqrt{-g}d^4x,$$

where the integration is performed over 4-space; g is the determinant of the metric tensor g_{ik}. We denote the integral of $\tilde{L}$ over space by

$$\tilde{E} = \int \sqrt{-g}\tilde{L}d^3x, \quad (\Delta\tilde{E} = \int \sqrt{-g}\Delta\tilde{L}d^3x). \quad (25)$$

By its physical meaning, $\tilde{E}$ is the system's energy for imposed additional conditions, such as allowance for the conservation of angular momentum, the total number of particles in the system, etc.

We break up the integral over space into an integral over the surface dual to the tensor $n^k_{\beta\gamma}$ and integrals over the lengths of the vortices orthogonally crossing this surface. Because of the presence of delta functions, the following sum remains from $\Delta\tilde{E}$:

$$\Delta\tilde{E} = \int \sqrt{-g}2\xi^{\beta\gamma}(x)(\partial_\beta\phi_\gamma)d^3x + \sum_{k=1}^{N} 2\pi l_k\sqrt{-g}\xi^{\beta\gamma}(x_k)n^k_{\beta\gamma},$$

where l_k is the length of vortex line k.

After varying $\Delta\tilde{E}$ over ϕ_γ, the following term remains:

$$-2\partial_\beta(\sqrt{-g}\xi^{\beta\gamma}). \quad (26)$$

If we discard addition (26), then the subsequent analysis will be valid only for an averaged description of the superfluid motion. Let us prove that term (26) vanishes on vortex cores. Since the coordinates x_k must correspond to equilibrium vortex positions in the system, the system must be stable against core displacements orthogonal to the direction of the vortices themselves:

$$2\pi l_k n^k_{\beta\gamma}[\partial_\beta(\sqrt{-g}\xi^{\beta\gamma})]\big|_{x=x_k} = 0. \quad (27)$$

This proves the above assertion. The corrections related to the term $\Delta\tilde{E}$ in action will not be considered everywhere, because we are interested in the system's dynamics only when expression (27) holds, i.e., on vortex cores, or, equivalently, only an averaged description of all quantities for the system. Below, we thus denote average quantities by a hat above the symbol (e.g., $\hat{A}$). According to Eq. (3), the principle of least action relative to a change in ν^2 leads to the equation

$$\frac{\partial L}{\partial \nu^2} = \frac{\partial}{\partial \nu^2}\{\nu^2[k^2/2 + F(\nu^2)]\} = 0. \quad (28)$$

Given that $k^2 = g^{\alpha\beta}\phi_\alpha\phi_\beta + 2g^{0\alpha}\phi_0\phi_\alpha + g^{00}(\phi_0)^2$ and denoting

$$A^\alpha = \frac{\partial\phi_0}{\partial\phi_\alpha}, \quad B^\alpha = \frac{\partial\phi^0}{\partial\phi_\alpha}, \quad (29)$$

[7] In general, addition (24) to $\tilde{L}$ should be written for each such surface, but this is implied by default.

we obtain

$$\frac{\partial k^2}{\partial \phi_\alpha} = 2g^{\alpha\beta}\phi_\beta + 2g^{0\alpha}\phi_0 + 2g^{0\alpha}\phi_\alpha A^\alpha + 2g^{00}\phi_0 A^\alpha = 2[\phi^\alpha + \phi^0 A^\alpha]. \quad (30)$$

Taking a variational derivative of Eq. (21) with respect to ϕ_γ and using Eqs. (29) and (30), we derive for the average quantities

$$\hat{B}^\gamma\left(\hat{\phi}_0 + \frac{\Omega}{c}\hat{\phi}_\varphi - \mu\right) = \hat{\phi}^\gamma - \frac{\Omega}{c}\hat{\phi}^0\delta^\gamma_\varphi. \quad (31)$$

Now, taking the variational derivative of Eq. (21) and using (28), we obtain

$$\hat{\phi}_0 + \frac{\Omega}{c}\hat{\phi}_\varphi - \mu = 0. \quad (32)$$

Comparing Eqs. (31) and (32), we obtain the analog of rigid-body rotation for a superfluid:

$$\left.\frac{\phi^\gamma}{\phi^0}\right|_{x = x_k} = \frac{\hat{\phi}^\gamma}{\hat{\phi}^0} = \frac{d\hat{x}^\gamma}{dx^0} = \frac{\Omega}{c}\delta^\gamma_\varphi. \quad (33)$$

3.3. Magnus Force and the General-Relativistic Theorem on the Conservation of Circulation

The Magnus force acts on a rotating body in an incoming flow and is attributable to a nonzero pressure difference for the opposite sides of the flow around the body. In turn, the pressure along the body boundary changes because of the Bernoulli theorem: the velocity of the medium that flows around a rotating body changes when going around the body axis.

Let us write the Bernoulli equation for the nonrelativistic case:

$$p + mn\mathbf{V}^2/2 = \text{const}. \quad (34)$$

It would be natural to consider a portion of the VL core as the body on which the Magnus force acts. As we show below, the Magnus force does not depend on the radius a of this core. Choose a cylindrical coordinate system whose z axis coincides with the rotation axis of this core. Since the core radius a is much smaller than any scales on which the incoming flow produced by the remaining vortices changes appreciably, this flow may be considered constant for the flow around the core. According to (33), the physical velocity of this flow at the core point is

$$\mathbf{V}_0 = [\mathbf{\Omega} \times \mathbf{r}].$$

At the same time, the velocity produced by the core itself on its boundary, according to (8) is

$$\mathbf{V}_k = \frac{\hbar}{m^* a^2}[\mathbf{e}_z \times \mathbf{a}],$$

where $\mathbf{a}$ and $\mathbf{e}_z$ are the vector in the direction of the core radius (equal to a in magnitude) and a unit vector along the core rotation axis, respectively. The total velocity on the core boundary is

$$\mathbf{V} = \mathbf{V}_0 + \frac{\hbar}{m^* a^2}[\mathbf{e}_z \times \mathbf{a}].$$

The force per unit core area is equal to the pressure multiplied by a unit vector: $-\mathbf{e}_a = -\frac{\mathbf{a}}{a}$. Accordingly, the force per unit core length is

$$\mathbf{F} = -\oint \mathbf{e}_a p(\varphi) dl = -\int_0^{2\pi} \mathbf{e}_a p(\varphi) a d\varphi. \quad (35)$$

Expressing P from Eq. (34) and substituting it in Eq. (35) yields

$$\mathbf{F} = -\int_0^{2\pi} \mathbf{a}\{\text{const} - mn(\mathbf{V}_0^2 + \mathbf{V}_k^2 + 2\mathbf{V}_0\mathbf{V}_k)/2\} d\varphi. \quad (36)$$

Since the φ-independent terms vanish and since $n \approx \nu^2$ and $m \approx m^*$ for a superfluid in the nonrelativistic case, we derive for the Magnus force per unit core length

$$\mathbf{F} = \int_0^{2\pi} \mathbf{a}\left\{mn\mathbf{V}_0\frac{\hbar}{m^* a^2}[\mathbf{e}_z \times \mathbf{a}]\right\} d\varphi = \pi\hbar\nu^2[\mathbf{V}_0 \times \mathbf{e}_z]. \quad (37)$$

It follows from Eq. (37) that the Magnus force acting on the VL core that is at rest relative to a remote observer causes it to move toward the vessel wall. As it accelerates toward the wall, an incoming flow emerges (to be more precise, the core itself runs on the superfluid); as a result, the Magnus force changes its direction, causing the VL core to precess around some point of the superfluid flow. This precession is rapidly damped, and the core starts moving in such a way that the Magnus force does not act on it, i.e., that the system's energy becomes minimal. This requires that the core be at rest with respect to the superfluid flow at its location. The above reasoning proves that the VL system is frozen in, i.e., that there is no slip in the nonrelativistic case.

In general relativity, expression (34) for the Bernoulli theorem is replaced with expression (20).

For the nonrelativistic case, Hess (1967) showed that the VLs are, as it were, frozen in a superfluid and move at angular velocity Ω, the shell rotation velocity. Thus, there is no slip relative to this angular velocity.

To generalize the slip theorem to general relativity, there is no need to repeat similar calculations in order to determine the Magnus force, which, incidentally, are very complex. It will suffice to note that $\phi_0 = ku_0$, $k = k(|\mathbf{V}|, p, n, g_{ik})$, and $u_0 = u_0(|\mathbf{V}|, g_{ik})$ and that when going

around the core of a vortex line, the changes in metric g_{ik} and density n, if any, are so negligibly small,[8] they may be disregarded.

Therefore, we can write for the superfluid portion adjacent to the core

$$p = p(|\mathbf{V}|). \tag{38}$$

We thus see that there is no general-relativistic Magnus force for a VL motion with $|\mathbf{V}| = \text{const}$ around the core. This is possible only when the VL core accompanies the superfluid flow, i.e., when $\mathbf{V}$ is produced by the core itself.

Consequently, given Eq. (33), we see that there is no slip in general relativity either.

In conclusion, note that the absence of slip also follows from another important theorem of hydrodynamics, the theorem on the conservation of circulation (see, e.g., Landau and Lifshitz 1988a).

4. CALCULATING THE MEAN DENSITY AND CURVATURE OF VORTEX LINES IN A PULSAR WITH GENERAL-RELATIVISTIC CORRECTIONS

4.1. Passing to a Rotating Frame of Reference

As will be evident below, it is more convenient to perform an analysis in a comoving (with vortex cores), i.e., rotating frame of reference.

According to Landau and Lifshitz (1988b), the following formulas can be derived that relate the tensor components in various frames of reference:

$$\begin{cases} g'_{\rho\rho} = g_{\rho\rho}; \quad g'_{\varphi\varphi} = g_{\varphi\varphi}; \quad g'_{zz} = g_{zz} \\ g'_{0\varphi} = g_{0\varphi} + \dfrac{\Omega}{c} g_{\varphi\varphi} \\ g'_{00} = g_{00} + \left(\dfrac{\Omega}{c}\right)^2 g_{\varphi\varphi} + 2\dfrac{\Omega}{c} g_{0\varphi} \\ u'_\rho = u_\rho; \quad u'_\varphi = u_\varphi; \quad u'_z = u_z; \quad u'_0 = u_0 + \dfrac{\Omega}{c} u_\varphi. \end{cases} \tag{39}$$

Here, the components in a frame of references rotating with angular velocity Ω are marked by primes.

4.2 Calculating the Covariant Curl of Superfluid Velocity and the Vortex Density in the System

By definition, the mean density of vortices is the number of vortices crossing the orthogonal surface divided by its area. Therefore, using Eq. (22) to derive the vortex density $\sigma_{\beta\gamma}$, we obtain

$$\sigma_{\beta\gamma} = \frac{K}{dx^\beta \wedge dx^\gamma} = \frac{1}{2\pi}(\partial_\beta \phi_\gamma - \partial_\gamma \phi_\beta). \tag{40}$$

[8] The core radius is known to have sizes of the order of 1–10 interparticle separations.

It is convenient to express the quantities ϕ_γ in terms of ϕ_0, the metric, and the shell angular velocity in the frame of reference under consideration:

$$\begin{cases} \phi_\alpha = \phi^0 g_{0\alpha} + \phi^\gamma g_{\alpha\gamma} = \phi^0\left(g_{0\alpha} + g_{\alpha\gamma}\dfrac{\phi^\gamma}{\phi^0}\right) \\ \phi_0 = \phi^0 g_{00} + \phi^\gamma g_{0\gamma} = \phi^0\left(g_{00} + g_{0\gamma}\dfrac{\phi^\gamma}{\phi^0}\right). \end{cases}$$

Hence, according to (33), we obtain for the average quantities

$$\hat{\phi}_\alpha = \hat{\phi}_0 \frac{g_{0\alpha} + \dfrac{\Omega}{c} g_{\varphi\alpha}}{g_{00} + \dfrac{\Omega}{c} g_{\varphi 0}}. \tag{41}$$

Since the average quantities do not depend on time and angle φ, we introduce the notation

$$X_\gamma = 2\pi\hat{\sigma}_{\varphi\gamma} = -\partial_\gamma \hat{\phi}_\varphi; \quad Y = \hat{\phi}_0;$$
$$Z = -\frac{g_{0\varphi} + \dfrac{\Omega}{c} g_{\varphi\varphi}}{g_{00} + \dfrac{\Omega}{c} g_{\varphi 0}}, \tag{42}$$

and derive from (41)

$$X_\gamma = \partial_\gamma (YZ). \tag{43}$$

On the other hand, we obtain from Eqs. (19) and (33)

$$X_\gamma = (c/\Omega)\partial_\gamma Y. \tag{44}$$

Solving the last two equations for X_γ and Y yields

$$X_\gamma = \text{const} \frac{\partial_\gamma Z}{\left(1 - \dfrac{\Omega}{c} Z\right)^2}, \tag{45}$$

$$Y = \frac{\text{const}}{1 - \dfrac{\Omega}{c} Z}. \tag{46}$$

Since $Y = \hat{\phi}_0 \longrightarrow k \longrightarrow \dfrac{m^* c}{\hbar}$ in the nonrelativistic limit, we see that $\text{const} = \dfrac{m^* c}{\hbar}$.

Hence, we have

$$\hat{\sigma}_{\varphi\gamma} = \frac{m^* c}{2\pi\hbar} \frac{\partial_\gamma Z}{\left(1 - \dfrac{\Omega}{c} Z\right)^2}. \tag{47}$$

As was shown above, $\Omega' = 0$ in the comoving (with cores) frame of reference; therefore, Eq. (47) in this frame of references is especially simple:

$$\hat{\sigma}^{\alpha'} = \frac{m^*c}{2\pi\hbar\sqrt{\tilde{\gamma}'}}e^{\alpha\gamma\varphi}\partial_\gamma g'_\varphi, \quad (48)$$

where, according to Landau and Lifshitz (1988b), $g_\gamma = -g_{0\gamma}/g_{00}$, $\tilde{\gamma} = -g/g_{00}$ is the determinant of the spatial metric tensor, and the three-dimensional vector σ^α dual to the tensor $\sigma_{\gamma\beta}$ was defined as $\sigma^\alpha = (2\sqrt{\tilde{\gamma}})^{-1} \cdot e^{\alpha\gamma\beta}\sigma_{\gamma\beta}$, $e^{\alpha\gamma\beta}$ is a unit antisymmetric tensor.

The vector $\hat{\sigma}^\alpha$ coincides in direction with the vortex direction in the system and is equal in magnitude to the mean vortex density at a given point.

For the invariant mean vortex density, we can write

$$\hat{\sigma} = \sqrt{\hat{\sigma}_{ij}\hat{\sigma}^{ij}} = \sqrt{2\hat{\sigma}_{0\alpha}\hat{\sigma}^{0\alpha} + \hat{\sigma}_{\alpha\beta}\hat{\sigma}^{\alpha\beta}}. \quad (49)$$

As a result, we have for the invariant density in the first post-Newton approximation

$$\hat{\sigma} \approx |\hat{\sigma}_{\varphi\alpha}|\sqrt{g^{\alpha\alpha}g^{\varphi\varphi}}, \quad (50)$$

which matches the nonrelativistic limit for the VL density.

According to Eqs. (39), we have for g'_α

$$g'_\alpha = \delta^\varphi_\alpha \frac{g_\varphi - \frac{\Omega}{c}\frac{g_{\varphi\varphi}}{g_{00}}}{1 + \left(\frac{\Omega}{c}\right)^2\frac{g_{\varphi\varphi}}{g_{00}} - 2g_\varphi\frac{\Omega}{c}}. \quad (51)$$

Given that $g' = g$, we obtain for $\tilde{\gamma}'$

$$\tilde{\gamma}' = -\frac{g'}{g'_{00}} = \frac{\tilde{\gamma}}{1 + \left(\frac{\Omega}{c}\right)^2\frac{g_{\varphi\varphi}}{g_{00}} - 2\frac{\Omega}{c}g_{0\varphi}}.$$

In the nonrelativistic case, $\tilde{\gamma} \longrightarrow \rho^2$, $g_{00} \longrightarrow 1$, $g_{\rho\rho} \longrightarrow -1$, $g_{\varphi\varphi} \longrightarrow \rho^2$, $g_{zz} \longrightarrow -1$, $g_{0\gamma} \longrightarrow 0$, $\phi_0 \longrightarrow k \longrightarrow \frac{m^*c}{\hbar}$; therefore, we derive the already known expression in this limit

$$\hat{\sigma}^\alpha \longrightarrow \hat{\sigma}^\alpha_0 = \delta^\alpha_z\frac{\Omega m^*}{\pi\hbar} = \text{const}.$$

For a millisecond pulsar, $\hat{\sigma}^\alpha_0 \sim 10^6$ cm^{-2}, with a separation between vortices $d \sim 10^{-3}$ cm corresponding to this value. As for the radius of the core itself, its order-of-magnitude value is 10^{-11} cm.

As we see from this section, the general-relativistic corrections that determine the curvature of VLs and the change in their mean density are small for real pulsars, and, therefore, the relative curvature does not exceed a few percent.

5. CALCULATING CORRECTIONS FOR A HOMOGENEOUS MODEL

Let us calculate the invariant density of vortex lines in a pulsar in the first post-Newton approximation. The model is based on the assumption that the pulsar interiors rotate at angular velocity Ω and, because the compressibility of a neutron condensate is low, its density is assumed to be $\tilde{\rho}$ in the entire volume.[9]

In the first post-Newton approximation, the metric in a conformally Euclidean coordinate system[10] can be written as

$$ds^2 = (1 + 2\tilde{\varphi})dt^2 - (1 - 2\tilde{\varphi})[d\rho^2 + dz^2 + \rho^2 d\varphi^2] - 2g_\varphi dt d\varphi. \quad (52)$$

According to Eq. (50), we write

$$\hat{\sigma} = \sqrt{g^{\gamma\gamma}g^{\varphi\varphi}}\frac{\hat{\sigma}_0}{2\Omega}\partial_\gamma[g_\varphi - \Omega g_{\varphi\varphi}/g_{00}], \quad \left(\hat{\sigma}_0 = \frac{\Omega m^*}{\pi\hbar}\right). \quad (53)$$

Since $g^{\alpha\alpha} \approx 1/g_{\alpha\alpha}$, the corrections to $\hat{\sigma}_0$ can be arbitrarily divided up into two groups:

(1) Gravimagnetic corrections: $\hat{\sigma}_1 = \left(\frac{m^*}{2\pi\hbar}\right)\frac{(\partial_\rho + \partial_z)g_\varphi}{\rho}$.

(2) Gravielectric corrections:

$$\hat{\sigma}_2 = \frac{\hat{\sigma}_0}{2}\frac{1 + 2\tilde{\varphi}}{\rho}(\partial_\rho + \partial_z)\left[\rho^2\frac{1 - 2\tilde{\varphi}}{1 + 2\tilde{\varphi}}\right] - \hat{\sigma}_0.$$

We thus see that the VL curvature and redistribution in a pulsar result from the gravimagnetic interaction of VLs with the Lense–Tirring field of the system and from the gravielectric deformation of the system's Euclidean geometry.

The Newton gravitational potential $\tilde{\varphi}$ of the model can be easily calculated:

$$\tilde{\varphi} = -2\pi\tilde{\rho}R^2(1 - x^2/3 - y^2/3) \quad (x = \rho/R, y = z/R). \quad (54)$$

Hence, it is easy to derive an expression for the gravielectric corrections:

$$\hat{\sigma}_2 = 4\pi\tilde{\rho}R^2\hat{\sigma}_0(1 - x^2 - y^2/3 - 2xy/3).$$

Given that $\tilde{\varphi}_R = -4\pi\tilde{\rho}R^2/3$ on the stellar surface, we obtain for the gravielectric corrections

$$\hat{\sigma}_2(x, y) = 3|\tilde{\varphi}_R|\hat{\sigma}_0(1 - x^2 - y^2/3 - 2xy/3). \quad (55)$$

[9] For convenience of calculations, we take $G = 1$ and $c = 1$ in this section.

[10] It is easy to see that the result does not depend on the choice of a coordinate system in this approximation.

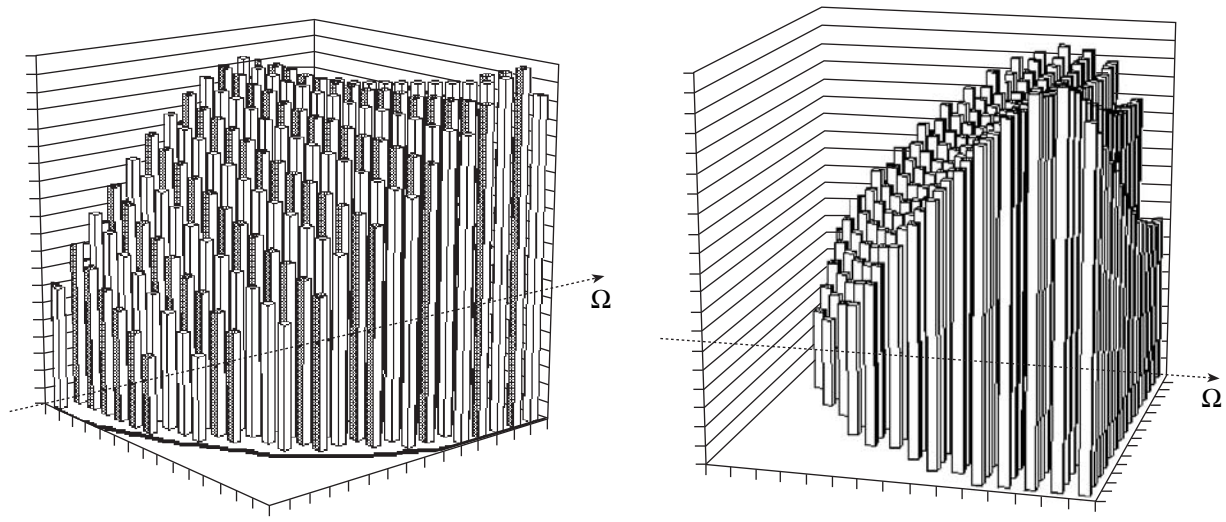

Dependence of corrections $(\hat{\sigma}_1 + \hat{\sigma}_2)/(\hat{\sigma}_0|\tilde{\varphi}_R|)$ along the vertical axis on coordinates: the rotation axis Ω and the perpendicular axis in the equatorial plane (the lower right quadrant of the pulsar meridional section is shown).

To determine the gravimagnetic corrections, we use Eq. (106.15) from Landau and Lifshitz (1988b) to derive the metric components g_φ. In Cartesian coordinates,

$$g_{0\alpha}(\mathbf{r}) = \frac{1}{2}\int_V \tilde{\rho}\, dr'^3 \left\{ \frac{7[\mathbf{\Omega}\times\mathbf{r}']_\alpha + ([\mathbf{\Omega}\times\mathbf{r}']_\beta, n_\beta)n_\alpha}{|\mathbf{r}-\mathbf{r}'|} \right\}, \quad (56)$$

where $n_\alpha = (r_\alpha - r'_\alpha)/|\mathbf{r}-\mathbf{r}'|$.

Hence, it is easy to calculate the angular component of the gravimagnetic field in cylindrical coordinates:

$$g_\varphi(\mathbf{r}) = -\frac{\rho}{2}\int_V \tilde{\rho}\, d\varphi|_{-\pi}^{+\pi} dz'\rho' d\rho' \left\{ \frac{7\Omega\rho'\cos\varphi}{|\mathbf{r}-\mathbf{r}'|} + \frac{\Omega\rho' p^2 \cos\alpha\cos\gamma}{|\mathbf{r}-\mathbf{r}'|^3} \right\}. \quad (57)$$

Here, $(\mathbf{r}-\mathbf{r}')^2 = (z-z')^2 + p^2$, $p^2 = \rho^2 + \rho'^2 - 2\rho\rho'\cos\varphi$, $\cos\alpha = \cos\varphi\sin\theta + \sin\varphi\cos\theta$, $\cos\gamma = -\sin\theta$, $\sin\theta = \frac{\rho'}{p}\sin\varphi$, and $\cos\theta = \frac{p^2+\rho^2-\rho'^2}{2p\rho}$.

As a result, expression (57) reduces to

$$g_\varphi(\mathbf{r}) = -\frac{\Omega\rho}{2}\int_V \tilde{\rho}\, d\varphi|_{-\pi}^{+\pi} dz'\rho' d\rho' \left\{ \frac{7\rho'\cos\varphi}{|\mathbf{r}-\mathbf{r}'|} + \frac{\rho'\sin^2\varphi(\rho'^2 + p\rho - p\rho'\cos\varphi)}{|\mathbf{r}-\mathbf{r}'|^3} \right\}. \quad (58)$$

Since the integrand is even in variable φ, by changing variables $x = \rho/R$, $x' = \rho'/R$, $y = z/R$, $y'(y) = (z'-z)/R$, and $p'(x, \varphi) = p/R$, we can write the expression for the gravimagnetic corrections as

$$\hat{\sigma}_1(x, y) = \hat{\sigma}_0|\tilde{\varphi}_R|\int_0^\pi d\varphi \int_0^1 dx'\, f(x, x', y, \varphi), \quad (59)$$

where

$$f(x, x', y, \varphi) = -\frac{3x'^2}{8\pi x}(\partial_x + \partial_y)\int_{y'_1}^{y'_2} dy' \left\{ \frac{7x\cos\varphi}{[y'^2 + p'^2]^{1/2}} + \frac{xx'\sin^2\varphi(x'^2 + p'x - p'x'\cos\varphi)}{[y'^2 + p'^2]^{3/2}} \right\}, \quad (60)$$

$$y'_1 = -\sqrt{1-x'^2} - y, \quad y'_2 = +\sqrt{1-x'^2} - y.$$

Hence, integrating and then differentiating yields

$$A = 7x\cos\varphi,$$

$$B = xx'\sin^2\varphi(x'^2 + p'x - p'x'\cos\varphi),$$

$$C = \sqrt{y'^2 + p'^2}$$

$$A_x = 7\cos\varphi,$$

$$B_x = x'\sin^2\varphi(x'^2 + p'x - p'x'\cos\varphi) + xx'\sin^2\varphi(p' + (x - x'\cos\varphi)^2/p'),$$

$$I_x = A_x \ln(y' + C) + A\frac{x - x'\cos\varphi}{C(y' + C)} + \frac{B_x y'}{Cp'^2}$$

$$- By'\frac{x - x'\cos\varphi}{p'^2 C^3} - 2By'\frac{x - x'\cos\varphi}{p'^4 C},$$

$$I_y = -A/C - B/C^3,$$

$$\Rightarrow f(x, x', y, \varphi) = -\frac{3x'^2}{8\pi x}[I_x + I_y]_{y'_1}^{y'_2}.$$

When deriving the last expression, we took into account the fact that the derivative with respect to y could be taken inside the integral and that $\partial_y = -\partial_{y'}$.

Integral (59) can be calculated numerically. The integration results with gravielectric corrections (55) are shown in the figure (the maximum amplitude of relative corrections is $\simeq 1$).

ACKNOWLEDGMENTS

I wish to thank Yu.M. Bruk and A.Yu. Andreev for help. I am also grateful to the late D.A. Kirzhnits, with whom the ideas and approaches to this study were formulated. This work was supported by the Russian Foundation for Basic Research (project no. 96-15-96616).

REFERENCES

1. A. Yu. Andreev, D. A. Kirzhnits, and S. N. Yudin, Pis'ma Zh. Éksp. Teor. Fiz. **61**, 825 (1995) [JETP Lett. **61**, 846 (1995)].
2. I. Bekarevich and I. M. Khalatnikov, Zh. Éksp. Teor. Fiz. **40**, 920 (1961) [Sov. Phys. JETP **13**, 643 (1961)].
3. N. N. Bogolyubov and D. V. Shirkov, *Quantum Field* (Nauka, Moscow, 1993).
4. A. A. Grib, S. G. Mamaev, and V. M. Mostepanenko, *Quantum Effects in Intense External Fields* (Atomizdat, Moscow, 1980).
5. J. R. Hartl and D. H. Sharp, Astrophys. J. **147**, 317 (1967).
6. G. B. Hess, Phys. Rev. **189**, 161 (1967).
7. D. A. Kirzhnits and S. N. Yudin, Usp. Fiz. Nauk **165**, 11 (1995).
8. L. D. Landau and E. M. Lifshitz, *Fluid Mechanics* (Pergamon, Oxford, 1987; Nauka, Moscow, 1988a).
9. L. D. Landau and E. M. Lifshitz, *The Classical Theory of Fields* (Pergamon, Oxford, 1975; Nauka, Moscow, 1988b).
10. D. Langlois, astro-ph/0008161.
11. R. N. Manchester and J. H. Taylor, *Pulsars* (Freeman, San Francisco, 1977; Mir, Moscow, 1980).
12. R. Prix, Phys. Rev. D **62**, 103005 (2000); gr-qc/0004076.

Translated by V. Astakhov

Astronomy Letters, Vol. 27, No. 5, 2001, pp. 313–323. Translated from Pis'ma v Astronomicheskiĭ Zhurnal, Vol. 27, No. 5, 2001, pp. 363–375.

Analysis of HST and IUE Ultraviolet Spectra for T Tauri Stars: DF Tau

S. A. Lamzin[1]*, A. A. Vittone[2], and L. Errico[2]

[1] *Sternberg Astronomical Institute, Universitetskiĭ pr. 13, Moscow, 119899 Russia*
[2] *Capodimonte Astronomical Observatory, Naples, Italy*

Received July 10, 2000; in final form, September 26, 2000

Abstract—We analyze ultraviolet spectra of DF Tau, a binary system whose primary component is a classical T Tauri star. The spectra were obtained from the Hubble Space Telescope and the IUE satellite. The stellar emission in the wavelength range covered is shown to originate in an accretion shock wave. The gas infall velocity is ~250 km s^{-1}. The accreted-gas density is typically $N_0 \le 10^{11}$ cm^{-3}, but it can occasionally be higher by one and a half orders of magnitude. The continuum intensity near $\lambda = 1900$ Å was found to be virtually constant for such a significant change in N_0. The star's photometric variability is probably attributable to variations in accreted-gas density and velocity, as well as to variations in the area of a hot spot on the stellar surface and in its orientation relative to the observer. The mean accretion rate is $\dot{M} \sim 3 \times 10^{-9} M_\odot$ yr^{-1}. The interstellar extinction for DF Tau is $A_V \simeq 0\overset{m}{.}5$, the stellar radius is $\le 2 R_\odot$, and the luminosity of the primary component is most likely no higher than $0.3 L_\odot$. We argue that the distance to DF Tau is about 70 pc. Upper limits are placed on the primary's coronal emission measure: $EM(T = 10^7 \text{ K}) < 3 \times 10^{54}$ cm^{-3} and $EM(T = 1.3 \times 10^6 \text{ K}) < 3 \times 10^{55}$ cm^{-3}. Absorption lines originating in the stellar wind were detected in the star's spectrum. Molecular hydrogen lines have essentially the same radial velocity as the star, but their full width at half maximum is FWHM $\simeq$ 50 km s^{-1}. We failed to explain why the intensity ratio of the C IV λ1550 doublet components exceeds 2. © *2001 MAIK "Nauka/Interperiodica".*

Key words: *stars—variable and peculiar*

INTRODUCTION

Here, we continue to analyze ultraviolet spectra of T Tauri stars from the Hubble Space Telescope (HST). We consider DF Tau, a classical T Tauri star (CTTS) with $W_{H\alpha} \sim 50$–60 Å (Herbig and Bell 1988). The star's brightness varies erratically: for example, its B magnitude changes by more than 3^m. Grinin (1980) assumed the light and (U–B) and (B–V) color variations to be attributable to the formation of hot spots on the stellar surface through unsteady circumstellar gas accretion. Apart from H I Balmer lines, the optical spectrum of DF Tau shows intense metal and helium emission lines. The blue and red emission-line wings exhibit absorption components whose presence is interpreted as evidence for the simultaneous gas accretion onto the star and the stellar wind from its vicinity [see Edwards *et al.* (1994), Johns-Krull and Basri (1997) and references therein].

Chen *et al.* (1990) found DF Tau to be a binary. According to Thiébaut *et al.* (1995), the semimajor axis of the secondary component's orbit is $0\overset{''}{.}19 \pm 0\overset{''}{.}03$, the orbital period is 82 ± 12 yrs, and the orbital inclination to the line of sight is $i = 63° \pm 5°$. Based on HST observations, Ghez *et al.* (1997) were able to determine the spectral energy distribution for each of the components. They estimated the spectral types of the primary and secondary stars to be M0 and M3, respectively, corresponding to effective temperatures of 3800 and 3350 K. Figure 3 from the above paper shows that the contribution of the secondary to the combined spectrum sharply decreases at $\lambda < 6000$ Å and accounts for less than 10% at $\lambda \simeq 3000$ Å. It thus apparently follows that the primary star is responsible for the observed line and continuum emission in DF Tau, so the ultraviolet spectra analyzed below belong to this star.

There is a large uncertainty in A_V for DF Tau, which affects parameter estimation for the star itself and estimation of the accretion and mass-loss rates. For example, according to Hartigan *et al.* (1995), $A_V = 1\overset{m}{.}3$, yielding a stellar luminosity of $\simeq 2 L_\odot$ and an accretion rate $\dot{M}_a = 8 \times 10^{-6} M_\odot$ yr^{-1}. Gullbring *et al.* (1998) found that $A_V = 0\overset{m}{.}45$ and $1.8 \times 10^{-7} M_\odot$ yr^{-1}. Finally, Ghez *et al.* (1997) obtained $A_V = 0\overset{m}{.}04 \pm 0\overset{m}{.}51$ and the primary's luminosity of $\simeq 0.51 L_\odot$.

* E-mail address for contacts: lamzin@sai.msu.ru

All the above authors assumed the star's distance (d) to be equal to the mean distance to the Tau-Aur star-forming region, i.e., 140 pc. However, the Hipparcos parallax for DF Tau is 0.02572 ± 0.00636 (ESA 1997), corresponding to $d \simeq 40$ pc. Although Bertout *et al.* (1999) doubt that the Hipparcos parallax is correct, they have failed to prove that it is in error. Meanwhile, Thiébaut *et al.* (1995) found the total mass of the system's components for $d = 140$ pc to be abnormally large, $M_s = M_1 + M_2 = 2.8 \pm 1.5 M_\odot$. However, if we assume that $d = 40$ pc, then M_s will decrease approximately to $0.1 M_\odot$, which is apparently too small even for a system of two M stars. The luminosity of DF Tau is found to be also too low ($\simeq 0.05 L_\odot$) if the value obtained by Ghez *et al.* (1997) is recalculated to the new distance. In addition, a change in distance will cause i inferred by Thiébaut *et al.* (1995) to deviate from the inclination of the DF Tau rotation axis to the line of sight (Bouvier and Bertout 1989), because the stellar radius will change. In turn, an appreciable deviation of i from 60° casts doubt on the Doppler imaging of DF Tau (Unruh *et al.* 1998). In short, we have to recognize that the parameters of DF Tau are known poorly. Below, we show what kind of information about the star can be extracted from HST and IUE spectra. All of our assertions about the accretion-shock structure and spectrum are based on our previous results (Lamzin 1998a); below, all references to this paper are omitted for brevity.

OBSERVATIONAL DATA

The spectra analyzed below were taken from the HST archival database and reduced by means of the IRAF v2.11 and STSDAS/TABLES v2.0.2 software packages. We applied the standard technique described in Chapter 36 of the HST Data Handbook (http://www.stsci.edu/documents/data-handbook.html); the files recommended in the archival database were used for calibration.

The spectra of DF Tau were taken on August 8, 1993, with the GHRS spectrograph with an intermediate ($\simeq 3$ km s^{-1}) resolution and recorded by detector 2. Table 1 gives the starting time of each exposure to within a minute (UT), the identification numbers of archival spectra, the diffraction gratings used, the spectral range covered, and the number of intermediate exposures (parameter RPTOBS+1). All spectra were taken in accumulation (ACCUM) mode with aperture LSA ($D \simeq 2''$) and have the same values of the following service parameters: FP_SPLIT = 'NO', STEPPATT = 5, and COMB_ADD = 'FOUR'. In the Objects column, the abbreviation W_Cal refers to auxiliary spectra, which were obtained to improve the wavelength calibration. The wavelengths were corrected for the Earth's and spacecraft motions and are given below for a vacuum at $\lambda < 2000$ Å and for air otherwise. The Atomic Line List v2.01 (http://www.pa.uky.edu/peter/atomic) and the catalog of molecular hydrogen lines (Roncin and Launay 1994) were used for line identification. To improve the signal-to-noise ratio, we used for our analysis the spectra averaged over all independent observations and additionally smoothed by a four-point running mean; these data are shown in Figs. 1–5. As a result, the formal resolution of our spectra was about 15 km s^{-1}.

The IUE spectra were taken from the INES database (http://ulda.inasan.rssi.ru) and were not subjected to any follow-up reduction.

LINE IDENTIFICATION IN THE STELLAR SPECTRUM

Figure 1 shows the spectrum of DF Tau near the Mg II λ2800 (uv 1) resonance doublet; in this and the following figures, the portions of the spectrum that fall on dead photodiodes of Detector 2 are indicated by thin lines. A continuum level of $\simeq 3.6(\pm 0.4) \times 10^{-14}$ erg s^{-1} cm^{-2} Å^{-1} is indicated in the spectrogram by a broken line. The uv 1 doublet lines ($^2S_{1/2}$–$^2P^o_{1/2,\,3/2}$ transition) have identical asymmetric profiles and represent an emission peak with absorption features superimposed on its blue wing. The narrow absorption feature near the line center is attributable to interstellar absorption, while the dip near –150 km s^{-1}, which sinks below the continuum level, appears to be attributable to stellar-wind absorption; the profiles of the Balmer hydrogen and Na I D lines exhibit similar features (Edwards *et al.* 1994; Najita *et al.* 2000).

However, the above optical lines exhibit no counterparts of yet another absorption feature seen to the left from the centers of both magnesium resonance doublet lines. The intensity minimum of this feature is shifted from the line center by ~–400 km s^{-1}, whereas the blue wing of the [O I] λ6300 line attributable to mass outflow from the star's vicinity extends no further than –250 km s^{-1} (Hartigan *et al.* 1995). We therefore assume that this absorption feature is unrelated to the uv 1 multiplet lines, but is attributable to the subordinate Mg II uv 3 ($^2P^o$–^2D) multiplet lines. The lower level of these multiple lines is the upper level of the uv 1 multiple resonance lines and is, probably, populated by the photons of these lines (Lamzin 2000a, 2000b; Errico *et al.* 2000). In other words, we assume that the emission peaks near λ2791 and 2798 Å, as well as the absorption dips located to the right from them, are the Mg II λλ2790.84, 2797.99, and 2798.06 lines with inverse P Cyg profiles. The maximum of the λ2790.84 Å line emission peak is shifted by +25 km s^{-1} from its laboratory value, while the maximum of the emission feature in the red wing of the Mg II k line is offset by +20 km s^{-1} from the unshifted position of the λ2798.06 Å line (see Fig. 1). We also see from the figure that the minimum of the absorption feature is shifted from the centers of the same lines by +164 and +160 km s^{-1}, respectively. The absorption features near +150 km s^{-1} also show up in the red wings of H_β, H_γ, H_δ, and Na I D (Edwards *et al.*

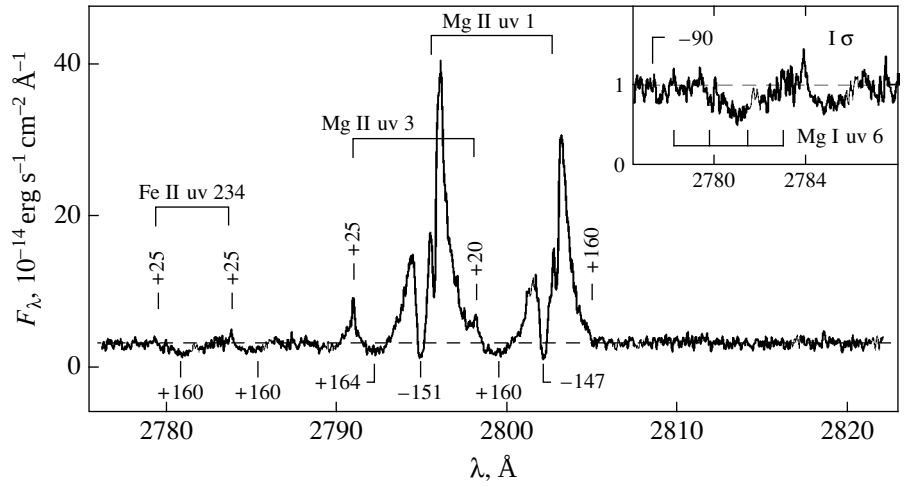

Fig. 1. Spectrum of DF Tau near the Mg II λ2800 doublet. In this and the following figures, the spectral flux density (in units of 10^{-14} erg s^{-1} cm^{-2} Å^{-1}) is plotted along the vertical axis, unless specified otherwise. A portion of the spectrum near the Fe II uv 234 multiplet lines is shown in the upper right corner on an enlarged scale, in which the continuum level was taken to be unity. The noise level σ determined from the continuum between 2806 and 2821 Å is shown (see the text for details).

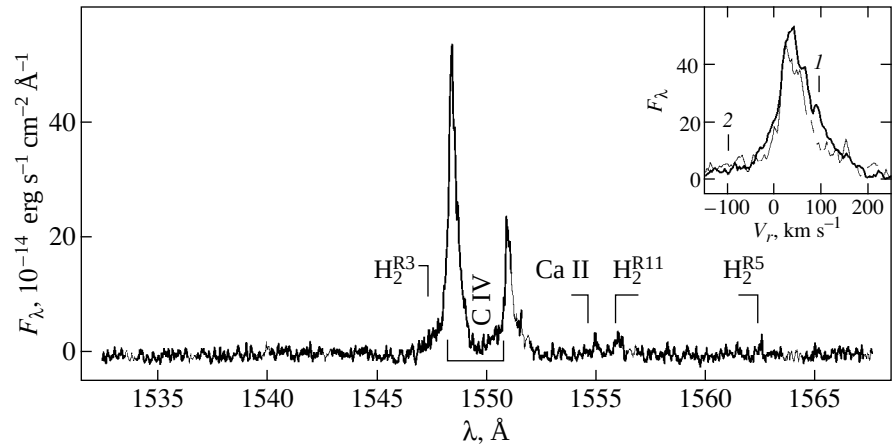

Fig. 2. Spectrum of DF Tau near the C IV λ1550 doublet. The profiles of the λ1548.20 Å (heavy line) and 1550.78 Å (thin line) doublet components are shown in the upper right corner; the intensity of the latter line was doubled. Number *1* in the red wing of the λ1548.20 line marks the expected position of Fe II λ1548.70; number *2* marks the expected position of Fe II λ1550.27 in the blue wing of λ1550.78 (see the text for details).

1994). At the same time, there is no similar feature in H_α, nor is it present in the Mg II uv 1 resonance doublet lines (see Fig. 1, in which a mark corresponding to +160 km s^{-1} is shown in the red wing of the Mg II h line). The small dip in the blue wing of the Mg II λ2790.84 line, which sinks below the continuum level and can be interpreted as a stellar-wind line, is also worth mentioning. Unfortunately, this portion of the spectrogram falls on dead diodes of Detector 2, so we are not completely sure that this absorption feature is real.

Similar HST/GHRS spectrograms for the stars RU Lup and RW Aur exhibit strong Fe II uv 234 λλ2779.30 and 2783.69 Å multiplet lines. In Fig. 1, we placed marks corresponding to shifts from the centers of these lines by +25 and +160 km s^{-1}. These marks turned out to point to the positions of (weak) emission peaks and the intensity minima of (deep) absorption features. It thus follows that the Fe II uv 234 multiplet lines also have inverse P Cyg profiles. In the upper right corner of Fig. 1, the vicinity of the λλ2779.30 and 2783.69 Å lines is shown on an enlarged scale, and the inverse P Cyg profile is seen more clearly. By analogy with RW Aur, we may suspect that the subordinate Mg I uv 6 multiplet lines are superimposed on the Fe II λ2779.30 line profile. In DF Tau, the only unblended line of this multiplet is the λ2778.20 Å line, which seems to have a P Cyg profile with the blue boundary of the absorption dip near –90 km s^{-1}. However, the signal-to-noise ratio is too low to talk with confidence not only about the profile, but also about the very presence of the Mg I uv 6 multiplet lines.

Table 1. Information about the observing session for DF Tau

t_0, UT	Spectrum code	Object	Grating	Δλ, Å	*N*
02 : 29	z18e0203m	W_Cal	G270M	2879–2924	1
02 : 30	z18e0204m	DF Tau	G270M	2777–2823	2
02 : 43	z18e0205m	W_Cal	G160M	1503–1539	1
02 : 44	z18e0206m	W_Cal	G160M	1384–1420	1
02 : 46	z18e0207m	DF Tau	G160M	1383–1419	4
04 : 06	z18e0208m	DF Tau	G160M	1532–1568	4
04 : 27	z18e0209m	DF Tau	G160M	1328–1364	5

Figure 2 shows the stellar spectrum near the C IV λ1550 resonance doublet. The total flux in the doublet lines is 4.2×10^{-13} erg s^{-1} cm^{-2}, which is approximately a factor of 1.9 higher than the flux obtained by Gomez de Castro and Franqueira (1997) from IUE observations of the star. The observed intensity ratio of the doublet components is 2.2. That the line intensity ratio exceeds 2 is clearly seen from a comparison of the λ1548.20 Å profile (heavy curve) with the profile of the 1550.78 Å line (thin curve), whose intensity was artificially doubled (see the upper part of the figure).

The spectrogram also exhibits the subordinate Ca II λ1554.64 line, with the metastable $^2D_{5/2}$ level serving as its lower level. This level appears to be pumped by the λ8542.09 line, the most intense calcium infrared triplet line in the spectrum of DF Tau (Batalha *et al.* 1996). The intensity peak of the λ1554.64 line is shifted by about +60 km s^{-1}, so its profile is similar to that of the C IV λ1548.20 line. There are also the λλ1547.34, 1555.89, and 1562.39 Å molecular hydrogen lines in the spectral range under consideration (see Table 2 for details). Column 1 gives vibrational and rotational quantum numbers for the line lower level belonging to the ground electronic configuration $X^1\Sigma_g^+$. Column 2 gives the same quantum numbers for the upper level belonging to the $2p\sigma B^1\Sigma_u^+$ electronic configuration. The letters *P* and *R* denote the $J'' = J' \pm 1$ transitions, respectively. Columns 3 and 4 list, respectively, line wavelengths and transition probabilities (Abgrall *et al.* 1993). All lines were combined into groups with a common upper level; information about the line that pumps this level by absorbing an H I Ly_α photon is provided at the beginning of the list. The last column gives wavelength shifts of these lines from the Ly_α line center (in units of velocity).

Figure 3 shows the spectrum of DF Tau near the Si IV λλ1393.76 and 1402.77 resonance doublet. Apart from the Si IV lines, there are intense molecular hydrogen lines in the spectrogram which severely distort the Si IV line profiles. It is unclear what is responsible for the abnormally high intensity of Si IV λ1402.77: the superposition of $H_2P(3)$ λ1402.65 Å onto it or this is an instrumental effect (we see from Fig. 3 that the region of enhanced intensity falls on dead photodiodes of Detector 2).

The emission feature near λ1335 Å in T Tauri stars has been previously thought to be the C II uv 1 (λλ1334.53, 1335.66, and 1335.71 Å) resonance triplet. However, it is evident from Fig. 4 that the emission feature near λ1335 Å in DF Tau is a blend of carbon and

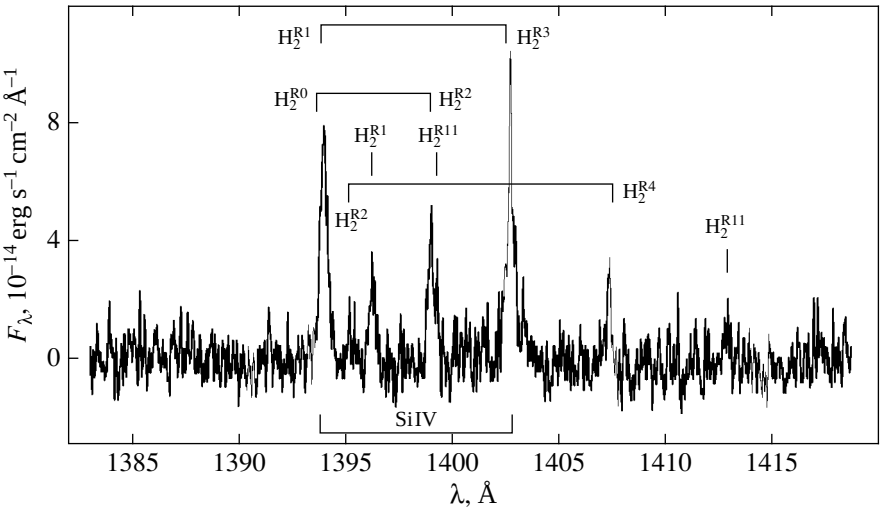

Fig. 3. Spectrum of DF Tau near the Si IV λ1400 doublet (see the text for details).

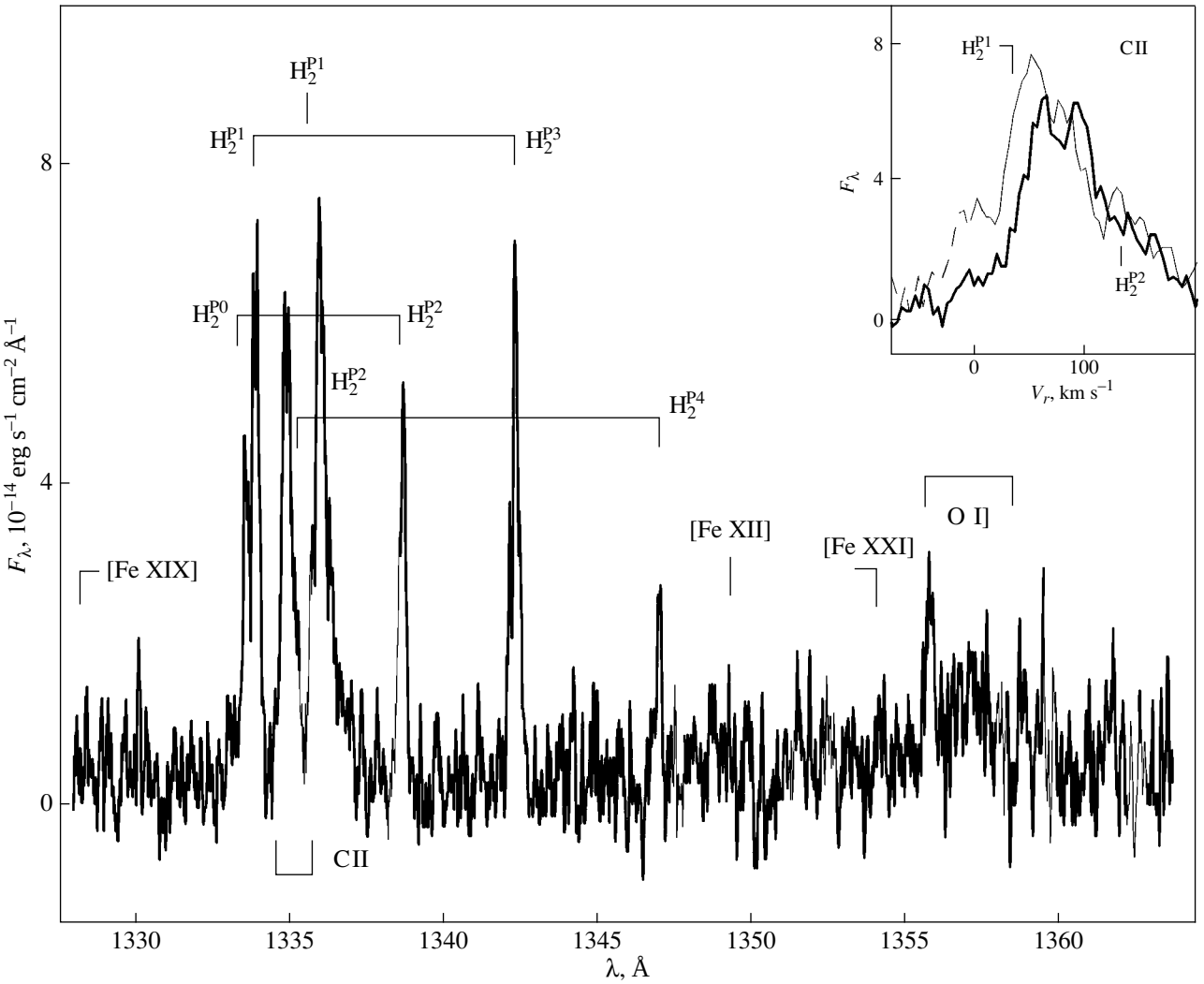

Fig. 4. Spectrum of DF Tau in the wavelength range 1328–1364 Å. The C II uv 1 multiplet line profile is shown in the right corner (see the text for details).

molecular hydrogen lines. The C II uv 1 multiplet line profiles are shown in the upper right corner of Fig. 4: the heavy and thin lines correspond, respectively, to the λ1334.53 Å line and a blend of the λ1335.66 and 1335.71 Å lines with their centers separated by 11.2 km s^{-1}. The C II lines are seen to be redshifted. However, it makes no sense to discuss the profile features, first, because of the low signal-to-noise ratio and, second, because of distortions, which are introduced by molecular hydrogen lines: R(2) λ1335.13 and P(1) λ1335.87 are superimposed on the red wing of the λ1334.53 Å line and on the blue wing of the λ1335.7 Å blend, respectively.

The spectrogram under consideration exhibits the O I λ1355.60 and 1358.51 resonance doublet lines, which form during a transition from the common $^5S_2^o$ upper level. The ratio of spontaneous-transition probabilities for the doublet components is 2 : 1, apparently in agreement with their observed intensity ratio. The intensity peak of the λ1355.60 line is shifted by about +50 km s^{-1}. The positions of three coronal lines are also in the wavelength range of the spectrogram: [Fe XII] λ1349.36, [Fe XIX] λ1328.90, and [Fe XXI] λ1354.10. None of these lines clearly shows up above the noise level. An upper limit on the flux in the coronal lines is estimated below, while for now we note that the mean continuum intensity in the range 1347 to 1355 Å is close to $\sigma_c \simeq 5 \times 10^{-15}$ erg s^{-1} cm^{-2} Å^{-1}; i.e., no continuum is seen in the spectrogram, nor is it seen in the spectrograms shown in Figs. 2 and 3.

INTERPRETING THE SPECTRUM OF DF Tau

Only two Fe II lines belonging to the uv 234 multiplet with λ2779.30 and 2783.69 Å are seen in the spectral range of Fig. 1; their lower-level excitation energy is $E_i \simeq 3.2$ eV. The situation with RW Aur and RU Lup is similar. The absence of other Fe II lines in the spec-

Table 2. Information about H_2 lines in the spectrum of DF Tau

v'', J''	v', J'	λ, Å	A_{ij}, 10^8 s^{-1}	ΔV, km s^{-1}
1, P13	2.12	1217.91	0.9	+550
5, R11		1399.24	0.8	
8, R11		1555.89	1.1	
2, R0	0.1	1217.21	0.7	+390
4, R0		1333.48	1.6	
4, P2		1338.57	3.1	
5, R0		1393.72	1.4	
5, P2		1398.95	2.6	
2, P1	0.0	1219.37	2.0	+913
4, P1		1335.87	4.7	
5, P1		1396.22	4.0	
2, R1	0.2	1217.65	0.8	+490
4, R1		1333.80	1.9	
4, P3		1342.26	2.8	
5, R1		1393.96	1.6	
5, P3		1402.65	2.3	
2, R2	0.3	1219.09	0.8	+840
4, R2		1335.13	2.0	
4, P4		1346.91	2.6	
5, R2		1395.20	1.8	
5, P4		1407.29	2.2	
2, P5	1.4	1216.07	1.6	+100
8, R3		1547.34	1.1	
8, P5		1562.39	1.2	
2, R9	2.10	1219.11	1.3	+850
5, P11		1412.82	1.0	

tral range covered can be explained by assuming that the Fe^+ level population with $E_i < 4$ eV corresponds to LTE at $T_e < 10^4$ K (Errico *et al.* 2000). This assumption is based on the fact all Fe II lower levels up to $E_i \simeq 4.7$ eV have the same parity, so their population is governed mainly by collisional transitions (McMurry *et al.* 1999).

Judging by their profiles, the Fe II and Mg II uv 3 lines originate in matter that falls to the star at a velocity of no less than 200 km s^{-1} (see Fig. 1). The lines have reverse P Cyg profiles, implying that part of the accreted matter lies between the star and the observer, and the other part is projected outside the stellar limb. The radial velocity of DF Tau is $V_r = 15.8 \pm 1.0$ km s^{-1} (Hartmann and Stauffer 1989), whereas the maximum of the emission peak of all metal lines and O I λ1355.60 has a radial velocity of ~25 km s^{-1}. This discrepancy probably stems from the fact that, apart from the radial velocity component, the accreted matter has a tangential velocity component, which seems quite natural from a theoretical point of view (Miller and Stone 1997).

Figure 2 shows that the wings of the C IV λ1550 doublet emission lines do not extend to the red further than 200 km s^{-1} either. Nevertheless, we believe the gas infall velocity V_0 for DF Tau to be much larger than this value for the following reasons. The point is that for stars in an accretion shock wave, the C IV λ1550 doublet lines originate mainly in the preshock H II region and far behind the shock front, where the cooled-gas recombination takes place. These two regions have different kinematic characteristics: the emitting-gas velocity relative to the star is V_0 and no higher than 10 km s^{-1} in the former and latter regions, respectively. It follows from calculations that the relative contribution of the zones to the total flux strongly depends on gas infall velocity; at $V_0 < 250$ km s^{-1}, the region whose gas is almost at rest relative to the star gives a larger contribution [see Lamzin (1998b) for more details]. Thus, if V_0 were appreciably lower than 250 km s^{-1}, the C IV λ1550 doublet lines would have virtually no extended red wings, which is in conflict with observations. The resulting line profile depends both on the accreted-gas parameters and on the geometry of the accretion zone and its velocity field. Since there is only one profile observation, we cannot unequivocally restore all these parameters and, hence, restrict ourselves to the assertion that V_0 is apparently closer to 300 than to 200 km s^{-1}.

In our case, this assertion proves to be informative. Calculations of evolutionary tracks indicate that young M0 stars cannot have masses above $0.5M_\odot$ (D'Antona and Mazzitelli 1994). Assuming that V_0 does not exceed the escape velocity $V_\infty = (2GM/R)^{1/2}$, we then find that the radius of DF Tau cannot be larger than $3R_\odot$. Actually, the radius must be appreciably smaller, because matter falls to the star not from infinity, but from a distance of the order of the radius of the accretion-disk inner boundary, which cannot exceed several stellar radii for T Tauri stars (Königl 1991). Hence, we obtain an upper limit on the stellar luminosity: $L < 0.4L_\odot(R/2R_\odot)^2 \times (T/3800)^4$.

To within the observational errors, this value matches the luminosity of the primary component inferred by Ghez *et al.* (1997). However, these authors assumed that the veiling continuum contributed negligibly to the primary's radiation at $\lambda \geq 5500$ Å. On the one hand, this results in an overestimation of the stellar luminosity, but, on the other hand, for the same reason, Ghez *et al.* (1997) obtained a very low interstellar extinction, which underestimated the primary's luminosity. Let us show that Ghez *et al.* (1997) actually underestimated A_V. Figure 5a presents the IUE spectrum of DF Tau taken on December 10, 1993, in the range 1850–3350 Å (spectrogram archival number 26 547 in the INES-LWP database). The continuum intensity near 2150 Å is seen to have a local minimum (partly masked by the Fe II emission), which can be naturally associated with the peak in the interstellar extinction curve in this spectral range (Bless and Savage 1972). Thus, A_V cannot be very low. Figures 5b–5d show how the same spectrum would appear if it were corrected for interstellar reddening with A_V equal to $0\overset{m}{.}5$, $1\overset{m}{.}0$, and $1\overset{m}{.}5$ by using a normal interstellar extinction law (Seaton 1979). We see that when A_V is

appreciably larger than $0^m.5$, a local maximum emerges in the continuum near 2150 Å. Unfortunately, the INES archive contains no spectra for DF Tau in the range 1150–1850 Å taken almost simultaneously with spectrum LWP 26 547, and we cannot trace the star's spectral energy distribution in a sufficiently extended range of wavelengths shorter than 2150 Å. Therefore, this method cannot yield a sufficiently accurate A_V, and we restrict ourselves to the assertion that it does not differ greatly from $0^m.5$, in agreement with $A_V = 0^m.45$ from Ghez *et al.* (1997).

Since the spectral energy distribution for M0 stars has a maximum near 1 μm, disregarding interstellar extinction with $A_V \simeq 0^m.5$, Ghez *et al.* (1997) underestimated the primary's luminosity by no more than 30%. Gullbring *et al.* (1998) estimated the accretion-shock contribution to the total luminosity of DF Tau to be of the same order of magnitude; therefore, the luminosity obtained by Ghez *et al.* (1997) is essentially constant. However, since the variability amplitude of DF Tau is large, the levels of stellar activity when the observations used in these two papers were carried out should be compared before drawing any conclusions.

Figure 6a shows how the *B* brightness of DF Tau varied with its *V* brightness in Johnson's photometric system from 1975 until 1997. The magnitudes were taken from the Herbst database (ftp://www.astro.wesleyan.edu/pub/ttauri). It follows from Fig. 1 in Gullbring *et al.* (1998) that the stellar λ = 4400 Å flux at the time of observation was 4.5×10^{-14} erg s^{-1} cm^{-2} Å^{-1}, corresponding to a magnitude $B \simeq 13^m.0$ (Allen 1977). Ghez *et al.* (1997) gave the star's brightness at the time of observation in the HST WFPC2 U', B', V', R', and I' photometric bands, which are similar to the corresponding bands of Johnson's system. Using their relations and data from Allen (1977), we found the total brightness of the components of DF Tau at the time of observation to be $13^m.10 \pm 0^m.04$ and $12^m.01 \pm 0^m.04$ in Johnson's *B* and *V* bands, respectively. The inferred value, indicated in Fig. 6 by the triangle, falls within the band of ground-based observations, and, consequently, the magnitudes were properly converted from the HST system to Johnson's system. We may now assert that during the observations of Ghez *et al.* (1997), the star was a mere $0^m.1$ fainter in *B* than it was during the observations of Gullbring *et al.* (1998); in both cases, its *B* brightness corresponded to the mean activity level of DF Tau (see Fig. 6b).

Thus, we conclude that our upper limit on the luminosity of the primary component of DF Tau, $L_* \simeq 0.4L_\odot$, agrees with its value obtained from observations by assuming that the distance to the star is close to 140 pc. By the estimate of Gullbring *et al.* (1998), for such a luminosity, the excess luminosity attributable to accretion must be of the order of $0.3L_* \simeq 0.1L_\odot$. The validity of this estimate is questionable, because Gullbring *et al.* (1998) used several arguable theoretical assumptions to

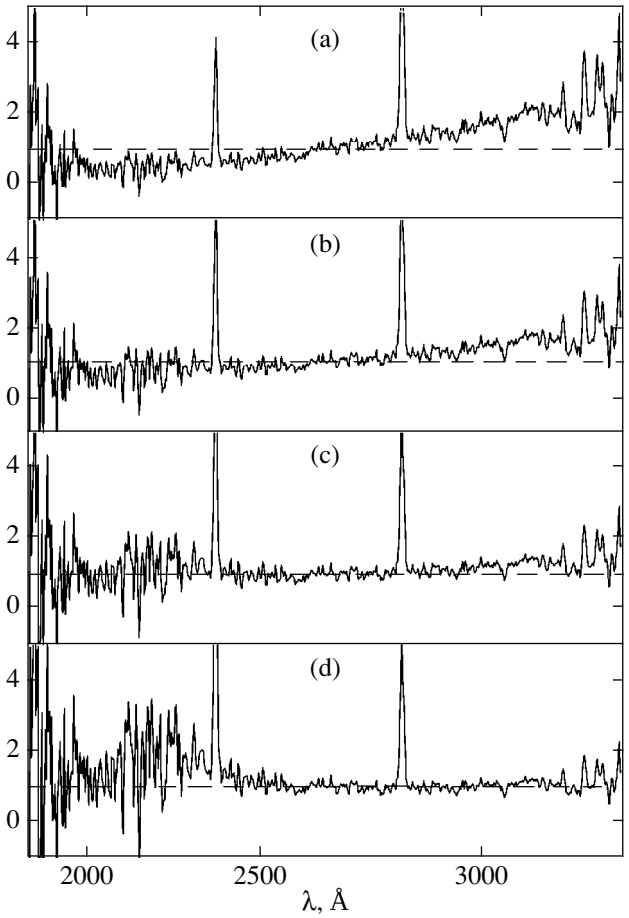

Fig. 5. (a) IUE spectrum LWP 26547 of DF Tau. The figures below show the same spectrum corrected for interstellar extinction with $A_V = 0^m.5$ (b), $1^m.0$ (c), and $1^m.5$ (d). All spectra were normalized to the continuum intensity at λ = 2600 Å (see the text for details).

convert the observed radiation intensity to the bolometric luminosity. However, the estimate is apparently valid in order of magnitude, as suggested by the following considerations. We see from Fig. 6b that the observations of Ghez *et al.* (1997) correspond to a *V* magnitude that is $0^m.8$ brighter than the minimum $V_{\min}$ between 1975 and 1997. If $V_{\min}$ is assumed to correspond to the almost complete absence of accretion-disk radiation, then, disregarding the contribution of the veiling continuum in *V*, Ghez *et al.* (1997) overestimated the star's luminosity approximately by 50%. In short, for the mean brightness of DF Tau, the accretion-shock luminosity is approximately a factor of 2 to 4 lower than the luminosity of the system's primary component: $L_* \simeq 0.3L_\odot$.

Let us see how well this value agrees with theoretical estimates. The accretion rate is

$$\dot{M} = 4\pi R_*^2 \xi \mu m_{\rm H} N_0 V_0$$

$$\simeq 4.2 \times 10^{-9} \left(\frac{N_0}{10^{11}}\right)\left(\frac{V_0}{250}\right)\left(\frac{\xi}{0.2}\right)\left(\frac{R_*}{2R_\odot}\right)^2 M_\odot/\text{year},$$

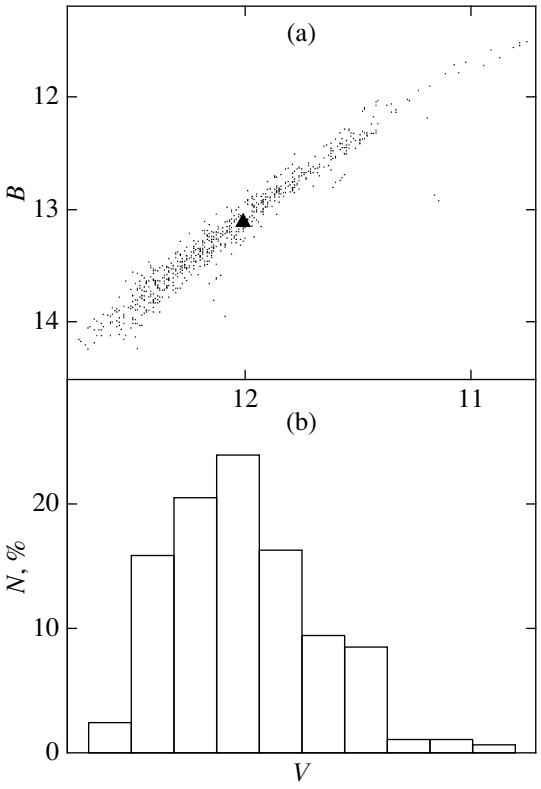

Fig. 6. (a) Relationship between brightness variations of DF Tau in the *B* and *V* bands of Johnson's system from 1975 until 1997. (b) A histogram that characterizes the percentage of occurrences of various brightness levels from 1975 until 1997 (see the text for details).

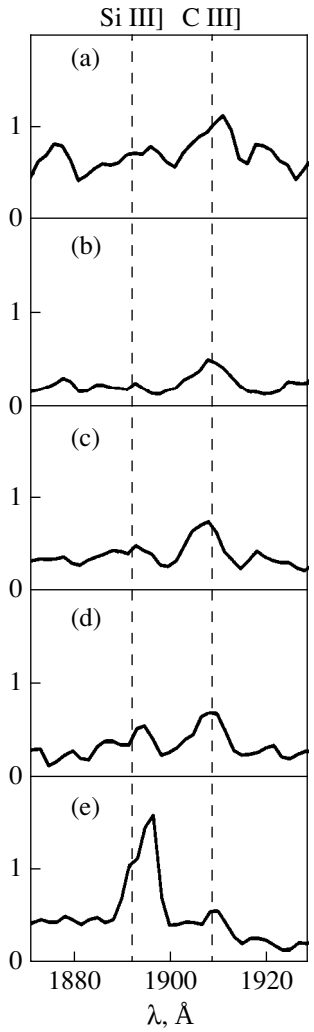

Fig. 7. Portions of the IUE spectra in the range 1150–1950 Å (see the text for details).

where $\mu = 1.3$ is the mean molecular weight of the accreted gas; $m_H \simeq 1.67 \times 10^{-24}$ g is the mass of the hydrogen atom; ξ is the fraction of the surface of a gas-accreting star with radius R_*; and N_0 and V_0 are the density and velocity of the accreted gas, given in cm^{-3} and km s^{-1} for numerical estimation, respectively. The accretion luminosity is

$$L_{ac} = \dot{M}\frac{V_0^2}{2} \simeq 5.0 \times 10^{-3} L_\odot \left(\frac{\dot{M}, M_\odot/\text{year}}{10^{-9}}\right)\left(\frac{V_0}{250}\right)^2.$$

We found that $R_* \le 2R_\odot$ and that V_0 most likely lies in the range 250 to 300 km s^{-1}. Judging by the Doppler imaging of DF Tau (Unruh *et al.* 1998), the fraction of the stellar surface occupied by hot gas (ξ) is close to 20%. Therefore, to estimate the accretion rate and accretion luminosity, we need only information about the infall gas density. Figure 7 shows portions of the IUE spectra near the Si III] λ1892 and C III] λ1909 intercombination lines. Figures 7a–7e correspond to spectra SWP 35386, 35392, 48853, 48871, and 48893 taken on January 20, 1989, January 22, 1989, October 5, 1993, October 8, 1993, and October 11, 1993, respectively. The flux ratios in these lines generally depend both on V_0 and on N_0. However, as follows from Fig. 3 in Gomez de Castro and Lamzin (1999), C III] λ1909 can be stronger than Si III] λ1892 at any reasonable V_0 only when $N_0 < 10^{11}$ cm^{-3}. We see from our Fig. 7 that in four of the five cases, the carbon line is appreciably stronger than the silicon line; consequently, the situation with $\log N_0 < 11$ is typical of DF Tau. This assertion is also supported by the fact that, when the first two spectrograms were taken, the star's *V* brightness was, respectively, $12^m.0$ and $12^m.1$ (Gomez de Castro and Franqueira 1997), which corresponds, according to Fig. 6b, to the mean level of stellar activity.

It thus follows that at the mean activity level of DF Tau, the accretion rate must be $\sim 3 \times 10^{-9}$ $M_\odot$ yr^{-1}, which is one and a half orders of magnitude lower than its value from Gullbring *et al.* (1998). For such $\dot{M}$, the accretion luminosity is $\simeq 0.02 L_\odot$; i.e., it accounts for a mere 10% of the primary's luminosity. This is several times smaller than follows from observations, and two possibilities can be suggested to overcome the contradiction. First, the calculations of the shock structure

(Lamzin 1998a) used to estimate the accreted-gas density may be erroneous. Second, the luminosity of the primary component of DF Tau may be several times lower than $0.3L_\odot$, for example, because the distance to the star is approximately a factor of 2 smaller than 140 pc. Note, incidentally, that a plausible estimate for the total mass of the system's components ($M_s = 0.35 \pm 0.2M_\odot$) is obtained at $d \simeq 70$ pc if we take the secondary's orbital parameters from Thiébaut *et al.* (1995).

Let us consider the causes of the DF Tau variability. The continuum intensities in Figs. 7a and 7e are approximately the same ($F_\lambda \simeq 5 \times 10^{-14}$ erg s^{-1} cm^{-2} Å^{-1}), although, judging by the intensity ratio of the Si III] λ1892 and C III] λ1909 lines, the infall gas density in the latter case increased by more than an order of magnitude compared to that in the former case. This may imply that the increase in N_0 was accompanied by the corresponding decrease in accretion-zone area, i.e., in ξ; that is why the accretion rate changed only slightly. However, an alternative possibility should also be borne in mind: a change in accretion-zone orientation relative to the observer, which also causes the (optically thick) continuum intensity to change (Lamzin 1995). The finite width of the band in Fig. 6a, which is several times larger than the observational errors, may be attributable to the combined effect of these two factors.

The intensity ratio of the resonance doublet components of lithium-like ions, to which the C IV λ1550 doublet belongs, must lie in the range 1 to 2, depending on line optical depth. The fact that the observed intensity ratio is larger than 2 by 10% requires a special explanation. It would be reasonable to assume that this is attributable either to the absorption of λ1550.78 line emission or to the superposition of an extraneous emission line on the λ1548.20 line. Note, incidentally, that the C IV λ1550 Å line profiles are similar in appearance to the profile of the subordinate He I λ5876 line in the stellar spectrum (Edwards *et al.* 1994; Batalha *et al.* 1996), so the distortions of the C IV profiles must actually be small.

If the Fe II level population is actually described by the Boltzmann formula with $T_e < 10^{-4}$ K, then one might expect two Fe II lines, λ1548.70 and λ1550.27 Å, near the C IV λ1550 doublet to have the largest optical depth. According to Errico *et al.* (2000), their optical depth must exceed $0.3\tau_{2784}$ and $10\tau_{2784}$, respectively, where τ_{2784} is the optical depth of the Fe II λ2784 line, the most intense absorption line in the spectral range of Fig. 1. As we see from the insert in Fig. 2, a small emission peak is actually superimposed on the blue wing of the C IV λ1548.20 line. It would be natural to identify this peak with the Fe II λ1548.70 line. Near the expected position of Fe II λ1550.27, there is also a small emission peak shifted by about +25 km s^{-1}, as in the case of other metal lines. The absorption component of this line may also be responsible for the small deficit of flux in the blue wing of C IV λ1550.78. At the same time, we failed to establish the cause of the difference between the carbon line profiles near their maximum, which, in fact, gives a major contribution to their abnormal intensity ratio.

Since the velocity of the gas accreted on DF Tau is definitely lower than 400 km s^{-1}, there can be virtually no iron ions in the shock wave with a change larger than +16. However, T Tauri stars exhibit intense X-ray radiation with energy >2 keV (Koyama *et al.* 1994; Carkner *et al.* 1996), suggesting the presence in young stars of regions with a temperature ~10^7 K that are not explicitly associated with the accretion shock wave (Lamzin 1999). It is therefore of interest to obtain information about the emission measure $EM = N_e^2 V$ of the region(s) with a temperature of 10^7 K in DF Tau by using the coronal [Fe XIX] λ1328.90 and [Fe XXI] λ1354.10 lines.

Assume that the region of interest is homogeneous and that the so-called coronal (ionization) equilibrium takes place in it, with hydrogen and helium being ionized virtually completely. The expression for the luminosity in an (optically thin) coronal line can then be written in standard form:

$$L \simeq 0.8h\nu_{ij}A_{ij}\frac{n_j}{N_e}n_{\rm ion}\xi_{\rm Fe}EM,$$

where $\xi_{\rm Fe} \simeq 4 \times 10^{-5}$ is the iron abundance; n_j is the relative population of the upper level for a $j \longrightarrow i$ transition; and $n_{\rm ion}$ is the relative abundance of the ion under consideration at the so-called temperature of maximum abundance T_m. For Fe XIX, $n_{\rm ion} \simeq 0.023$ at $\log T_m = 6.9$; for Fe XXI, $n_{\rm ion} \simeq 0.025$ at $\log T_m = 7.0$; and for Fe XII, $n_{\rm ion} \simeq 0.3$ at $\log T_m = 6.1$ (Arnaud and Raymond 1992). The relative level population n_j was calculated for a five-level model atom at temperature T_m for various electron densities N_e. The respective atomic parameters for Fe ions were taken from the CHIANTI database (Dere *et al.* 1997).

Let us consider the [Fe XXI] λ1354.10 line. Calculations show that the upper-level population for this line at $\log N_e < 13$ is satisfactorily fitted by the expression $n_j = 1.8 \times 10^{-14}N_e$. For the luminosity in this line, we therefore derive the relation $L_{1354} = 1.5 \times 10^{-27}EM$. The observed line flux is

$$F_{1354} = \frac{L_{1354}}{4\pi d^2}\exp(-0.92A_{1354}),$$

where A_{1354} is the interstellar absorption coefficient at wavelength λ = 1354 Å, which can be calculated from the known A_V by using the fitting formula from Seaton (1979). If we assume the distance d to the star to be 70 pc and $A_V = 0^m.5$, then we obtain $EM \simeq 10^{69}F_{1354}$ cm^{-3}.

If an (optically thin) line originates in a hydrostatically equilibrium region with a temperature of 10^7 K, then it must have the full width at half maximum FWHM ≃ 0.2 Å, determined by thermal ion motion.

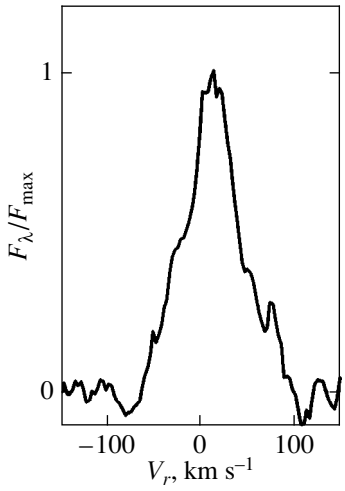

Fig. 8. Average profile of molecular hydrogen lines in the spectrum of DF Tau. Radial velocity (in km s^{-1}) is plotted along the horizontal axis (see the text for details).

Since the [Fe XXI] λ1354.10 line cannot be clearly distinguished above the noise level, it would be natural to assume that $F_{1354} \le \mathrm{FWHM} \times 3\sigma_c$, where $\sigma_c \simeq 5 \times 10^{-5}$ erg s^{-1} cm^{-2} Å^{-1} is the rms deviation of noise fluctuations near the line (see above). We then obtain $F_{1354} \le 3 \times 10^{-15}$ erg s^{-1} cm^{-2} and, consequently, $EM(T = 10^7\ \mathrm{K}) < 3 \times 10^{54}$ cm^{-3}. Similar estimation of the emission measure for hot regions using the [Fe XIX] λ1328.90 line yields a much higher upper level on *EM* at almost the same T_m, and, hence, it is of no interest.

Generally, the [Fe XII] λ1349.38 line in T Tauri stars can originate both in coronal regions and behind the accretion shock front (Lamzin 1999). Here, we restrict ourselves to estimating the emission measure only in the coronal model. To this end, two facts should be taken into account. First, the upper-level population for the transition under consideration at $\log T_m = 6.1$ is $n_j \simeq 3 \times 10^{-15} N_e$ (with an accuracy of ~30% for $\log N_e < 12$), so $L_{1349} = 6.8 \times 10^{-29} EM$. Second, the expected FWHM, along with the upper level on the flux, is approximately a factor of 3 smaller than that for [Fe XXI] λ1354.10; i.e., $F_{1349} \le 1 \times 10^{-15}$ erg s^{-1} cm^{-2}. As a result, we obtain $EM(T = 1.25 \times 10^6\ \mathrm{K}) < 2 \times 10^{55}$ cm^{-3}.

As we already pointed out above, the magnesium lines in Fig. 1 exhibit absorption components originating in the stellar wind. Based on the analyzed observational data, we can say little about the stellar-wind parameters of DF Tau. In particular, using the method described by Errico *et al.* (2000), we found that, if the absorption dip in the blue wing of the Mg II λ2790.84 line is real, then the atomic hydrogen column density of the stellar wind lN_H at the time of observation exceeded 10^{18} cm^{-2}. Thus, the fact that the ROSAT satellite detected no X-ray radiation from DF Tau (Neuhauser *et al.* 1995) may be attributable to the high stellar-wind density at the time of observation rather than to the low stellar luminosity in this range.

The molecular hydrogen lines are moderately intense in the stellar spectrum. To improve the signal-to-noise ratio, we drew the H_2-"line" profile in Fig. 8 constructed by averaging four unblended lines whose maximum intensity was initially normalized to unity: P(2) λ1338.57, P(3) λ1342.26, P(1) λ1396.22, and P(2) λ1398.95. The centroid of the average line is redshifted by about 15 km s^{-1}, which essentially matches the radial velocity of DF Tau from Hartmann and Stauffer (1989): $V_r = 15.8 \pm 1.0$ km s^{-1}. In other words, the H_2-line formation region moves only slightly along the line of sight relative to the star. This appears strange enough, because the line wings extend to ±100 km s^{-1}. If we attribute such a large wing extension to the optical depth rather than to gas motion, then we will have to assume a high population of the levels of the ground electronic configuration with $v = 4$ and 5, whose excitation energy is approximately 3 eV. It thus follows that in the H_2-line formation region, the gas density is high, and the temperature is ~2000 K.

CONCLUSION

Our constraints on the radius of the primary component of DF Tau ($R_* \le 2R_\odot$) and on the interstellar extinction ($A_V \simeq 0\overset{m}{.}5$) allow us to constrain the luminosity of this star: $L < 0.3L_\odot$, which is apparently in agreement with observations. An analysis of the ultraviolet spectrum for DF Tau clearly shows that circumstellar gas accretion is responsible for the star's activity. The theoretically estimated accretion rate that corresponds to the mean activity level was found to be low: $\dot{M} \sim 3 \times 10^{-9} M_\odot\ \mathrm{yr}^{-1}$. If the reliability of the theoretical calculations on which this estimate is based is not called into question, then the distance to DF Tau should be assumed to be ≃70 pc in order to reconcile our result with the observed relative intensity of the veiling continuum.

Judging by the large photometric variability and the intensity variation of emission lines, the accretion is unsteady. It turns out that the observed continuum intensity may be virtually constant when the accreted-gas density changes by more than an order of magnitude. At the same time, we believe that the observed photometric variability can be attributed, in part, to a change in accretion-zone orientation relative to the observer.

ACKNOWLEDGMENTS

We wish to thank Dr. F. Launay, who provided an electronic version of the atlas of molecular hydrogen lines, and S.Yu. Melnikov who helped us to extract data from the INES database. S. Lamzin is grateful to the administration of the Capodimonte Observatory (Naples, Italy) for the invitation and support, as well as the Russian Foundation for Basic Research (project no. 99-02-17184).

REFERENCES

1. H. Abgrall, E. Roueff, F. Launay, *et al.*, Astrophys. J., Suppl. Ser. **101**, 273 (1993).
2. C. W. Allen, *Astrophysical Quantities*, 3rd ed. (Athlone Press, London, 1973; Mir, Moscow, 1977).
3. M. Arnaud and J. C. Raymond, Astrophys. J. **394**, 39 (1992).
4. C. C. Batalha, N. M. Stout-Batalha, G. Basri, and M. A. O. Terra, Astrophys. J., Suppl. Ser. **103**, 211 (1996).
5. C. Bertout, N. Robichon, and F. Arenou, Astron. Astrophys. **352**, 574 (1999).
6. R. C. Bless and B. D. Savage, Astrophys. J. **171**, 293 (1972).
7. J. Bouvier and C. Bertout, Astron. Astrophys. **211**, 99 (1989).
8. C. Carkner, E. D. Feigelson, K. Koyama, *et al.*, Astrophys. J. **464**, 286 (1996).
9. W. P. Chen, M. Simon, A. J. Longmore, *et al.*, Astrophys. J. **357**, 224 (1990).
10. F. D'Antona and I. Mazzitelli, Astrophys. J., Suppl. Ser. **90**, 467 (1994).
11. K. P. Dere, E. Landi, H. E. Mason, *et al.*, Astrophys. J., Suppl. Ser. **125**, 149 (1997).
12. S. Edwards, P. Hartigan, L. Ghandour, and C. Andrulis, Astron. J. **108**, 1056 (1994).
13. L. Errico, S. A. Lamzin, and A. A. Vittone, Astron. Astrophys. **357**, 951 (2000).
14. A. M. Ghez, R. J. White, and M. Simon, Astrophys. J. **490**, 353 (1997).
15. A. I. Gómez de Castro and M. Franqueira, ULDA Access Guide to T Tauri Stars Observed with IUE, ESA SP-1205, 1997.
16. A. I. Gómez de Castro and S. A. Lamzin, Mon. Not. R. Astron. Soc. **304**, 41 (1999).
17. V. P. Grinin, Astrofizika **16**, 243 (1980).
18. E. Gullbring, L. Hartmann, C. Briceno, and N. Calvet, Astrophys. J. **492**, 323 (1998).
19. P. Hartigan, S. Edwards, and L. Ghandour, Astrophys. J. **452**, 736 (1995).
20. L. Hartmann and J. R. Stauffer, Astron. J. **97**, 873 (1989).
21. G. H. Herbig and K. R. Bell, Lick Obs. Bull. **1111**, 1 (1988).
22. C. M. Johns-Krull and G. Basri, Astrophys. J. **474**, 433 (1997).
23. A. Königl, Astrophys. J. Lett. **370**, L39 (1991).
24. K. Koyama, Y. Maeda, M. Ozaki, *et al.*, Publ. Astron. Soc. Jpn. **46**, L125 (1994).
25. S. A. Lamzin, Astrophys. Space Sci. **224**, 211 (1995).
26. S. A. Lamzin, Astron. Zh. **75**, 367 (1998a) [Astron. Rep. **42**, 322 (1998a)].
27. S. A. Lamzin, Astrophys. Space Sci. **261**, 137 (1999b).
28. S. A. Lamzin, Pis'ma Astron. Zh. **25**, 505 (1999) [Astron. Lett. **25**, 430 (1999)].
29. S. A. Lamzin, Pis'ma Astron. Zh. **26**, 273 (2000a) [Astron. Lett. **26**, 225 (2000a)].
30. S. A. Lamzin, Pis'ma Astron. Zh. **26**, 683 (2000b) [Astron. Lett. **26**, 589 (2000b)].
31. S. A. Lamzin, Astron. Zh. **77**, 373 (2000c) [Astron. Rep. **44**, 323 (2000c)].
32. A. D. McMurry, C. Jordan, and K. G. Carpenter, Mon. Not. R. Astron. Soc. **302**, 48 (1999).
33. K. A. Miller and J. M. Stone, Astrophys. J. **489**, 890 (1997).
34. J. Najita, S. Edwards, G. Basri, and J. Carr, in *Protostars and Planets IV*, Ed. by A. Mannings *et al.* (Univ. of Arizona Press, Tuscon, 2000), p. 457.
35. R. Neuhauser, M. F. Sterzik, J. H. M. M. Schmitt, *et al.*, Astron. Astrophys. **297**, 391 (1995).
36. J.-Y. Roncin and F. Launay, J. Phys. Chem. Ref. Data **4**, 1 (1994).
37. M. J. Seaton, Mon. Not. R. Astron. Soc. **187**, 75 (1979).
38. The Hipparcos and Tycho Catalogues, ESA SP-1200, 1997.
39. E. Thiébaut, Y. Balega, I. Balega, *et al.*, Astron. Astrophys. **304**, L17 (1995).
40. Y. C. Unruh, A. Collier Cameron, and E. Guenther, Mon. Not. R. Astron. Soc. **295**, 781 (1998).

Translated by V. Astakhov

Astronomy Letters, Vol. 27, No. 5, 2001, pp. 324–327. Translated from Pis'ma v Astronomicheskiĭ Zhurnal, Vol. 27, No. 5, 2001, pp. 376–380.

Infrared Observations of the Star R Cas

A. É. Nadzhip[1], A. M. Tatarnikov[1], V. I. Shenavrin[1], G. Weigelt[2], and B. F. Yudin[1]*

[1] *Sternberg Astronomical Institute, Universitetskiĭ pr. 13, Moscow, 119899 Russia*
[2] *Max Planck Institute for Radio Astronomy, Auf dem Hügel 69, Bonn, D-53121 Germany*

Received June 30, 2000; in final form, September 22, 2000

Abstract—We present our *JHKLM* photometry for R Cas performed during 1988–2000. The pulsation period of R Cas is $P \approx 429\overset{d}{.}6$, with the maximum IR brightness lagging behind the maximum visual brightness by ~0.2 *P*. The amplitude of light variations appreciably decreases with increasing wavelength at $\lambda \leq 3$ μm. At $\lambda > 3$ μm, this decrease virtually ceases. There is a step on the ascending branch of IR *JHK* brightness. The *K–L* color index increases linearly with *K* magnitude: $K–L = 0.304K + 1\overset{m}{.}20$. The color temperature dependence, $T_{K–L} = f(K)$, is also linear: $T_{K–L} = -622K + 1100$ K. In going from minimum to maximum, the *K* flux (as well as the bolometric flux) from the star and its color temperature $T_{K–L}$ increase by a factor of ~2.2 and ~1.3, respectively.

Key words: *stars—variable and peculiar*

INTRODUCTION

R Cas belongs to the class of Mira Ceti long-period variable giants (Miras). The period of its variations is $P \approx 430\overset{d}{.}5$, and the peak-to-peak visual amplitude is $\Delta V \approx 9$. The red giant's spectral type varies in the range M6e–M10e (Kholopov *et al.* 1985). The visual light curve of R Cas was described in detail by Isles and Saw (1989). They estimated the period of its light variations to be $\sim 429\overset{d}{.}5$. The brightness rise and decline times are $\sim 173\overset{d}{.}8$ and $255\overset{d}{.}0$, respectively. The asymmetry factor is $f = t_{rise}/P \approx 0.40$.

The near-IR light curve of R Cas was given by Lockwood and Wing (1971). Their observations (28 data points) were carried out during 1965–1970 at a wavelength of 1.04 μm with a narrow-band filter. The mean variability amplitude is $\Delta I \approx 1.6$. It may change from cycle to cycle by $\sim 0\overset{m}{.}5$. The above authors analyzed the light curves of 24 Miras. Their maximum IR brightness turned out to be shifted in phase from the maximum visual brightness by $\Delta\varphi = 0.1–0.2$. In other words, if, as assumed for Miras, the maximum visual brightness corresponds to phase $\varphi = 0$, then the maximum IR brightness occurs at $\varphi = 0.1–0.2$. In turn, the phases of minima lie in the range $\varphi = 0.5 \pm 0.1$. The light curves of most Miras exhibit a step near $\varphi \approx 0.7$. There is no such step on the light curve of Mira Ceti, the prototype of this class of stars.

Here, we present and analyze our photometry for R Cas.

OBSERVATIONS

Photometric *JHKLM* observations of R Cas have been performed with the 1.25-m telescope at the Crimean Station of the Sternberg Astronomical Institute since 1988. The IR photometer was described by Nadzhip *et al.* (1986). The star BS 8860 ($J = 1.46$, $H = 0.62$, $K = 0.37$, $L = 0.25$, and $M = 0.67$) was chosen as a photometric standard. Our photometry is given in the table. The measurement errors do not exceed $0\overset{m}{.}02$. Figure 1 shows *JHKLM* light curves of R Cas during 1997–2000, when the series of observations was densest. Figure 2 presents (*J–L*, *K*), (*K–L*, *K*), and (*J–L*, *K–L*) diagrams.

In Fig. 3, the *J* light curve is folded with the period $P = 429\overset{d}{.}6$. The dates of maxima are given by

$$\mathrm{Max}(J) = 2\,447\,151 + 429\overset{d}{.}6E. \quad (1)$$

The zero phase corresponds to maximum IR brightness. Below, it is denoted by ψ to distinguish it from the phase φ, which was calculated by using the ephemeris of visual maximum light for R Cas (Kholopov *et al.* 1985):

$$\mathrm{Max}(V) = 2\,444\,463 + 430\overset{d}{.}476E. \quad (2)$$

DISCUSSION

We searched for the period of IR brightness variations in R Cas using the software developed by Yu.K. Kolpakov (http://infra.sai.msu.ru/prog/kolpakov). The method of searching for a periodicity involves fitting a given time series by a complex polynomial; a third-degree polynomial restores a cubic trend of the constant signal component and a Fourier decomposition up to the third har-

* E-mail address for contacts: yudin@sai.msu.ru

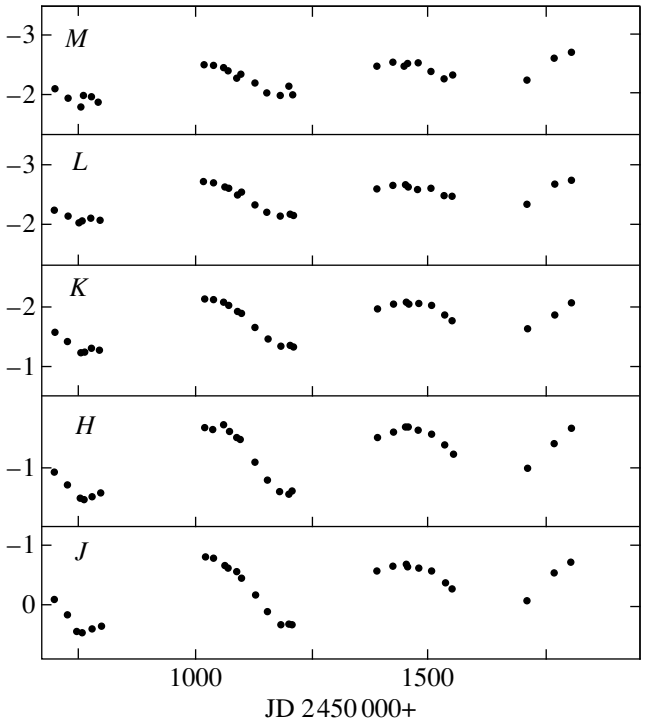

Fig. 1. *JHKLM* light curves of R Cas.

monic. The coefficients of the fitting polynomial can be determined by least squares.

The periods found in *JHKL* lie in the range 429.5–429.8 days. We determined the initial epoch of maximum IR brightness (1) from the time of maximum light of R Cas in 1999, when there was a sufficiently dense series of observations (Fig. 1). It is evident from Eqs. (1) and (2) that our estimated period is shorter than that from the GCVS (Kholopov *et al.* 1985) by almost one day. At the same time, the period of visual brightness variations in R Cas from Isles and Saw (1989) matches our estimate.

According to the ephemeris of pulsations (2), the maximum IR brightness of R Cas corresponds to $\varphi \approx 0.22$. In other words, it occurs ~0.22 *P* after the maximum visual brightness. At the same time, the maximum *I* brightness of the star observed in August 1966 (Lockwood and Wing 1971) corresponds to $\varphi \approx 0.16$. Thus, the delay of the IR brightness maximum from the visual brightness maximum increases from *I* to *J*, *H*, *K*, and *L*. It may well be that the delay varies with time, and this conclusion then becomes invalid.

We see from Fig. 3 that a step shows up on the light curve near $\psi \approx 0.6$; it emerges because of a delay in brightness rise. The star's *J* brightness can change from maximum to maximum by $\sim 0\overset{m}{.}3$ (Fig. 3). The curve that fits the folded light curve in Yu.K. Kolpakov's program has an amplitude of $\sim 1\overset{m}{.}4$, $1\overset{m}{.}1$, $1\overset{m}{.}0$, $0\overset{m}{.}8$, $0\overset{m}{.}5$, and $0\overset{m}{.}5$ in *I*, *J*, *H*, *K*, *L*, and *M*, respectively. We may take it as the mean amplitude of light variations in the star and, accordingly, conclude that it decreases with increasing wavelength in the range 1–3 μm and remains essentially constant in the range 3–5 μm.

We see from the (*J–L*, *K*) and (*K–L*, *K*) diagrams in Fig. 2 that R Cas reddens with declining brightness; i.e., its color temperature in the near IR decreases. Of all the color–magnitude diagrams, the (*K–L*, *K*) diagram exhibits the smallest scatter of data points about the curve fitting this dependence; it will suffice to take a linear polynomial for its fitting: $K\text{–}L = 0.304K + 1\overset{m}{.}20$. In other words, the *K–L* color index increases linearly with *K* magnitude, i.e., with declining brightness of the star.

We see from Fig. 2 that at a given *K* brightness of the star, the range of *J–L* variations is appreciably larger than that of *K–L* variations, especially near minimum light. This shows up more clearly in the (*J–L*, *K–L*) dia-

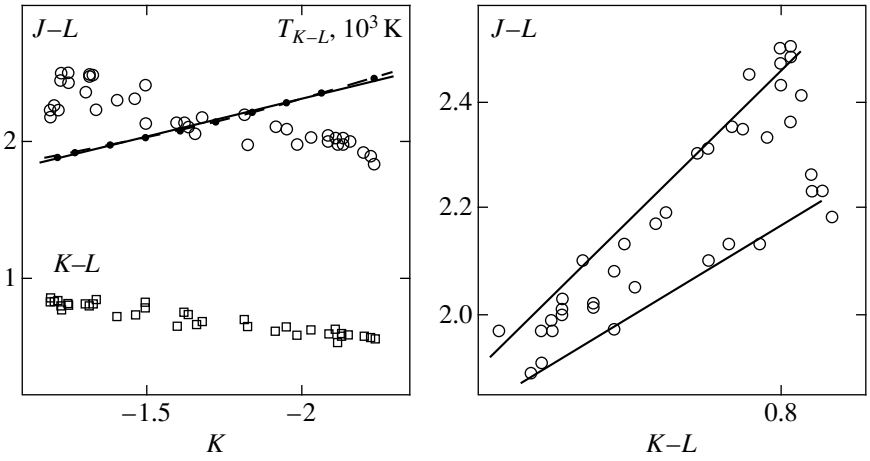

Fig. 2. (*J–L*, *K*), (*K–L*, *K*), and (*J–L*, *K–L*) diagrams and the $T_{K-L} = f(K)$ relation (dots). The solid and dashed lines represent linear and quadratic polynomial fits to the (T_{K-L}, *K*) relation, respectively.

JHKLM photometry for R Cas

JD 2440000+	*J*	*H*	*K*	*L*	*M*
7398	0.10	−0.57	−1.23	−2.08	−1.97
7404	0.19	−0.55	−1.24	−2.07	−2.01
7405	0.19	−0.55	−1.24	−2.07	−2.00
7431	0.15	−0.57	−1.25	−2.08	−2.11
7433	0.17	−0.57	−1.23	−2.06	−1.95
7774	0.22	−0.62	−1.33	−2.14	−2.00
7825	−0.23	−0.98	−1.61	−2.36	−2.21
7852	−0.25	−0.97	−1.62	−2.35	−1.49
8133	−0.25	−0.99	−1.64	−2.30	−2.25
9595	0.03	−0.80	−1.36	−2.20	−2.26
9613	−0.15	−0.98	−1.50	−2.28	−2.30
9641	−0.46	−1.26	−1.79	−2.43	−2.50
9751	−0.87	−1.72	−2.15	−2.70	−2.50
10403	0.09	−0.86	−1.50	−2.32	−2.18
10698	−0.11	−0.96	−1.59	−2.24	−2.08
10726	0.16	−0.78	−1.42	−2.14	−1.93
10754	0.42	−0.60	−1.26	−2.03	−1.78
10763	0.44	−0.58	−1.26	−2.06	−1.97
10777	0.41	−0.59	−1.28	−2.09	−1.95
10793	0.35	−0.65	−1.28	−2.08	−1.87
11018	−0.81	−1.57	−2.14	−2.70	−2.49
11035	−0.78	−1.54	−2.12	−2.69	−2.47
11060	−0.66	−1.58	−2.06	−2.63	−2.42
11069	−0.61	−1.53	−2.02	−2.61	−2.38
11088	−0.54	−1.42	−1.93	−2.51	−2.26
11095	−0.46	−1.40	−1.90	−2.54	−2.32
11124	−0.17	−1.09	−1.66	−2.34	−2.19
11152	0.11	−0.84	−1.47	−2.20	−2.00
11180	0.33	−0.67	−1.34	−2.14	−1.97
11199	0.32	−0.65	−1.35	−2.16	−2.11
11205	0.33	−0.69	−1.34	−2.15	−2.00
11387	−0.57	−1.44	−1.97	−2.59	−2.46
11420	−0.65	−1.51	−2.04	−2.66	−2.53
11447	−0.67	−1.58	−2.08	−2.66	−2.48
11452	−0.64	−1.58	−2.06	−2.65	−2.51
11475	−0.61	−1.53	−2.05	−2.58	−2.53
11502	−0.58	−1.48	−2.02	−2.61	−2.38
11532	−0.38	−1.32	−1.87	−2.48	−2.25
11548	−0.28	−1.20	−1.78	−2.47	−2.32
11707	−0.07	−1.01	−1.64	−2.35	−2.24
11767	−0.54	−1.35	−1.88	−2.67	−2.60
11802	−0.72	−1.56	−2.07	−2.74	−2.70

gram, which consists, as it were, of two branches (indicated by solid lines) diverging with increasing color indices, i.e., with a declining brightness of the star. For stars surrounded by dust envelopes, the *J–L* color index is a sensitive indicator of the optical depth of the dust envelope. However, the divergence between the two branches near minimum light exceeds the effect that might be expected for R Cas during possible variations in the optical depth of its dust envelope due to the nonstationary condensation of dust envelopes around Miras (Fleischer *et al.* 1992).

The relation between the color temperature (T_{K-L}) and *K* magnitude for R Cas is shown in Fig. 2. The derived $T_{K-L} = f(K)$ relation is essentially linear. In Fig. 2, it is indicated by the solid line (the dashed line represents a quadratic polynomial) and takes the form $T_{K-L} = -622K + 1100$ K. Accordingly, at maximum and minimum brightness (JD 2451035 and JD 2450763 in the table), $K \approx -2.12$ and -1.26, while $T_{K-L} \approx 2420$ and 1880 K. Thus, the *K* flux increases by a factor of ~2.2, while the color temperature increases by a factor of ~1.3. Note that the bolometric flux at maximum and minimum IR brightness of R Cas, which can be estimated by integrating the corresponding energy distributions, changes by the same factor as does the *K* flux.

In October 1996, Hofmann *et al.* (1999) estimated the angular diameter of R Cas at 1.04 μm to be $\theta_{1.04} \sim 29\overset{''}{.}9 \times 10^{-3}$. At that time, the Mira was near its minimum IR brightness ($\psi \approx 0.47$). By comparing the visibility curve derived from their interferometric observations with a theoretical curve, they determined the star's photospheric radius (the Rosseland radius, $\tau_{Ross} = 1$). Having estimated the bolometric flux and the corresponding bolometric luminosity, they also inferred the effective temperature of R Cas. As a result, they obtained $\theta_{Ross} \approx 32\overset{''}{.}9 \times 10^{-3}$ and $T_{eff} \approx 1900$ K.

In August 1999, near its maximum brightness ($\psi \approx 0.93$), the angular diameter of R Cas was estimated in *K* to be $\theta_K \approx 25\overset{''}{.}3 \times 10^{-3}$ (Weigelt *et al.* 2000). In this case, according to Weigelt *et al.* (2000), $\theta_{Ross} \approx 24\overset{''}{.}2 \times 10^{-3}$ and $T_{eff} \approx 2680$ K. Our photometric observations of R Cas in August 1999 were obtained four days after their interferometric observations (JD 2451420 in the table). In 1996, the photometric observations (JD 2450403 in the table) follow the interferometry 43 days later, but their phases are roughly symmetric about the phase of minimum IR brightness: $\psi \approx 0.47$ and 0.57. Thus, knowing the angular diameter and brightness of the star at the corresponding wavelength, we can determine its brightness temperature: $T_{1.04} \approx T_J \approx 2100$ K at minimum and $T_K \approx 2680$ K at maximum.

Thus, exceeding the color temperature by ~200 K, the brightness temperature increases from minimum to maximum by a factor of ~1.3, i.e., approximately by the same factor as does the color temperature. At the same time, the apparent diameter decreases by a factor of ~1.18. Thus, we can apparently estimate the change in brightness temperature and, accordingly, predict the change in monochromatic angular diameter of R Cas from the change in the Mira's color temperature (T_{K-L}). Concurrently, the star's effective temperature increases by a factor of ~1.4, while the photospheric radius decreases by a factor of ~1.36. The effective tempera-

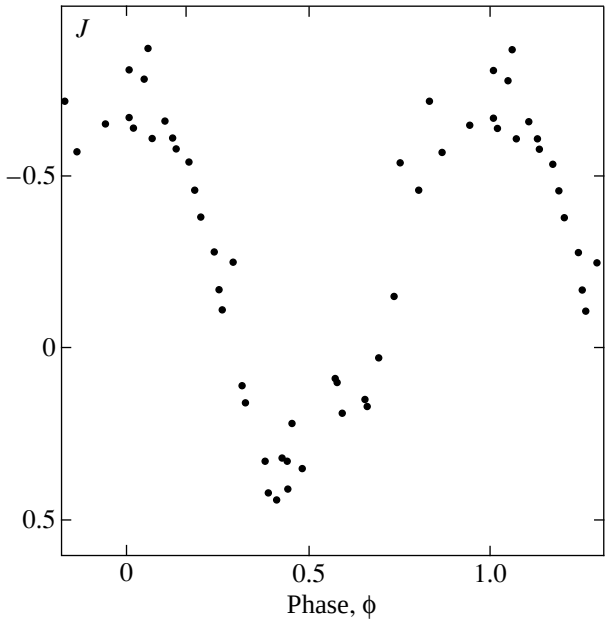

Fig. 3. The *J* light curve of R Cas folded according to Eq. (1).

ture matches the color and brightness temperatures at minimum and maximum brightness, respectively.

CONCLUSION

The pulsation period of R Cas estimated from our photometric observations is $P \approx 429^{d}.6$, with the maximum IR brightness lagging behind the maximum visual brightness by ~0.2 *P*. The amplitude of brightness variations appreciably decreases with increasing wavelength at $\lambda \leq 3$ μm. At $\lambda > 3$ μm, this decrease essentially ceases. Therefore, the middle- and far-IR flux from R Cas can be predicted by using photometric *LM* observations. A step is observed on the ascending branch of IR brightness.

Of all the color–magnitude diagrams, the *K–L*, *K* diagram is most suitable for estimating the color-temperature variations in R Cas. The *K–L* color index increases linearly with *K* magnitude, i.e., with declining brightness of the star: $K–L = 0.304K + 1.20$. The $T_{K–L} = f(K)$ relation is also linear: $T_{K–L} = –622K + 1100$ K. From minimum to maximum, the *K* flux from the star (as well as the bolometric flux) and its color temperature (as well as its infrared brightness temperature) increase by a factor of ~2.2 and ~1.3, respectively. The latter makes it possible to predict changes in the star's monochromatic angular diameter.

REFERENCES

1. A. J. Fleischer, A. Gauger, and E. Sedlmayr, Astron. Astrophys. **266**, 321 (1992).
2. K.-H. Hofmann, Y. Balega, M. Scholz, and G. Weigelt, Astron. Astrophys. **353**, 1016 (1999).
3. J. E. Isles and D. R. B. Saw, J. Br. Astron. Soc. **99**, 121 (1989).
4. P. N. Kholopov, N. N. Samus', V. P. Goranskiĭ, *et al.*, in *General Catalogue of Variable Stars* (Nauka, Moscow, 1985), Vol. 1, p. 236.
5. G. W. Lockwood and R. F. Wing, Astrophys. J. **169**, 63 (1971).
6. A. É. Nadzhip, V. I. Shenavrin, and V. G. Tikhonov, Tr. Gos. Astron. Inst. im. P. K. Shternberga **58**, 119 (1986).
7. G. Weigelt, K.-H. Hofmann, and M. Scholz, private communication, 2000.

Translated by N. Samus'

Astronomy Letters, Vol. 27, No. 5, 2001, pp. 328–337. Translated from Pis'ma v Astronomicheskiĭ Zhurnal, Vol. 27, No. 5, 2001, pp. 381–392.

A Spectroscopic Study of the Secondary Star of BM Ori: Preliminary Results

É. A. Vitrichenko[1]* and V. G. Klochkova[2]

[1] *Space Research Institute, Russian Academy of Sciences, ul. Profsoyuznaya 84/32, Moscow, 117810 Russia*
[2] *Special Astrophysical Observatory, Russian Academy of Sciences, Nizhni Arkhyz, Stavropol kraĭ, 357147 Russia*

Received June 14, 2000; in final form, September 5, 2000

Abstract—Two CCD spectra of the star BM Ori were obtained with the echelle spectrograph of the 6-m telescope. In one of the spectra, a large proportion of lines are distorted by emission. The emission component is blueshifted by 50 km s^{-1}, suggesting hot-gas outflow from the atmosphere. The equivalent-width ratio of measured lines in the spectra outside and during eclipse is consistent with the assumption that ~2/3 of the primary star's area is obscured during eclipse, as follows from light curves. Measured line equivalent widths were used to estimate atmospheric parameters of the secondary star, $T_{\rm eff}$ = 7300 K, $\log g$ = 5.2, and microturbulence ξ_t = 6 km s^{-1}, and to determine its chemical composition. The C, Na, Al, Si, S, Ca, Fe, Ni, and Zn abundances are solar, within the error limits. Li, Sc, Ti, V, Cr, Mn, Co, and Y are overabundant, while Mg, Cu, and Ba are underabundant. In general, the secondary is similar in chemical composition to the star V1016 Ori. Based on the secondary's mass determined by solving the radial-velocity curve and on $\log g$ estimated spectroscopically from iron ionization equilibrium, we calculated its photospheric radius, $R_2 = 0.5R_\odot$. However, the spectroscopic $\log g$ = 5.2 disagrees with $\log g$ = 3.5 calculated from the luminosity and effective temperature and with $\log g$ = 3.0 calculated from light and radial-velocity curves. If the secondary's photospheric radius is indeed small; this argues for the hypothesis that the eclipsing body is a dust envelope. The radial velocities measured from the two spectra are systematically higher than those calculated from the radial-velocity curve by +34 and +24 km s^{-1}. It is likely that the secondary's atmosphere occasionally shrinks. *© 2001 MAIK "Nauka/Interperiodica".*

Key words: *stars—variable and peculiar, properties and classification*

INTRODUCTION

The Orion Trapezium stars belong to extremely young Galactic objects. The faintest of the four stars that form the Trapezium, BM Ori (=HD 37021), arouses particular interest. This is a spectroscopic binary and eclipsing system with a period of 6.5 days, but the pattern of eclipse and the nature of its secondary component have been the subject of debate for several tens of years.

The main difficulty in understanding this stellar system lies in the fact that its light curve shows a total eclipse 8.5 h in duration, but at the same time the spectrum during totality remains the same as that outside eclipse (Doremus 1970; Popper and Plavec 1976). Meanwhile, the star significantly reddens during an eclipse, suggesting that a definitely cooler star is located in front of it (Zakirov and Shevchenko 1982).

A number of exotic hypotheses about the nature of the secondary star have been proposed to resolve this paradox [see Vitrichenko (1998a) for an overview]. Another unusual idea was developed in the above paper: an eclipse is produced by a dust envelope around the secondary. Vasileĭskiĭ and Vitrichenko (2000) considered a different eclipsing scheme which assumes the presence of a third light in the system. In this case, the primary and secondary stars are B4 V and G2 III, respectively, while the third light comes from a blue B0 VI subdwarf.

The identification of secondary lines in the stellar spectrum could prove this hypothesis. A history of searching for these lines was outlined in Vitrichenko *et al.* (1996), who confirmed that the weak yellow sodium *D*1 and *D*2 doublet lines actually belonged to the secondary star, but the existence of other secondary lines was called into question.

A crucially important question arises: in which spectral region is the contribution of the secondary star largest or, in other words, in which wavelength range are secondary lines the easiest to detect? This question was answered by Vitrichenko and Larionov (1996): by studying the continuum spectrum, they showed that the secondary's contribution to the system's total light was largest in the wavelength range 1–2 μm. Consequently, secondary lines should be sought in the red. The contribution of the secondary component in the photographic band is small; that is why experienced spectroscopists detected no secondary lines in this spectral range (Plaskett and Pearce 1931; Struve and Titus 1944).

* E-mail address for contacts: vitrich@nserv.iki.rssi.ru

Table 1. Observational data

No.	JD 245124…	Phase	V_r, km s^{-1}	ΔV_r, km s^{-1}	λ, Å
1	6.329	0.054	132(1)	–26	4400–7700
2	2.239	0.436	132(2)	–26	5000–6600

Another method of searching for secondary lines involves analyzing the spectrum near primary minimum. In this case, secondary lines in the V band are enhanced by a factor of ~2 compared to the spectrum outside eclipse. Such a spectrum was obtained, and 18 secondary lines were detected and measured (Vitrichenko and Plachinda 2000), arguing against the opinion of Doremus (1970) that there are no changes in the spectrum during eclipse.

Here, we set the following objectives: (1) finding secondary lines in the red and measuring their equivalent widths; (2) determining atmospheric parameters of the secondary component from these measurements; (3) estimating the secondary's chemical composition and comparing it with the chemical composition of another Orion Trapezium member, V1016 Ori, and with the mean chemical composition of old-cluster giants; and (4) determining the secondary's photospheric radius from its mass calculated by solving the radial-velocity curve and from its spectroscopically estimated surface gravity and comparing it with the radius of the eclipsing body calculated by solving the light curve. If these radii are equal, within the error limits, then the secondary star is the eclipsing body. If, however, the photospheric radius is smaller than the radius of the eclipsing body, then the eclipse is produced by a dust envelope around the secondary component.

OBSERVATIONAL DATA

Our observational data were obtained with the PFES echelle spectrograph mounted on the 6-m telescope (Panchuk *et al.* 1998). See Table 1 for details.

Here, columns 1 and 2 list arbitrary spectrum numbers and Julian date for the middle of a 30-min exposure, respectively. Column 3 gives the phase calculated with the elements from Bondar' and Vitrichenko (1995). It accidentally turned out that both spectra were obtained outside eclipse but near conjunctions. Spectrum 1 was taken immediately after the star emerged from primary minimum, while spectrum 2 was taken before the beginning of secondary minimum. Columns 4 and 5 give spectroscopically measured radial velocities uncorrected for the Earth's motion and corrections to the radial velocities for this motion, respectively. The wavelength ranges covered by the spectra are given in the last column.

The spectra were wavelength calibrated by using telluric lines. Subsequently, we filtered the spectra to increase the signal-to-noise (S/N) ratio. The filter was in the shape of a 0.8-Å-wide rectangular window. Simulations show that at the secondary's rotational velocity $V\sin i$ = 60 km s^{-1} (Vitrichenko and Plachinda 2000), filtration broadens lines by ~5% and reduces their central depth by the same amount. In this case, however, the S/N ratio increases by a factor of ~2, which is much more important than a slight loss of resolution. During the filtration, we simultaneously solve the problem of adding up overlapping orders of spectrum. As a result, the S/N ratios for spectra 1 and 2 were ~500 and ~400, respectively.

LINE EQUIVALENT WIDTHS

Many authors searched for secondary lines [see Vitrichenko *et al.* (1996) for an overview]. These searches aimed at constructing a radial-velocity curve for the secondary star. The equivalent widths of secondary lines were given only by Vitrichenko and Plachinda (2000), who analyzed a relatively narrow spectral range (~80 Å) and identified 18 lines. Here, we investigate a wide spectral range (~3300 Å) and identified ~400 secondary lines.

The technique for measuring line equivalent widths has been described in detail previously (Vitrichenko and Klochkova 2000). Based on the VALD list of lines, we first identified and measured about 520 lines for spectrum 1 and about 300 lines for spectrum 2. Subsequently, outliers in radial velocities, in line widths, and in chemical-composition deviations were removed from the line list. The final line list for spectrum 1 contains ~400 lines, which are given in Table 2.[1]

Our analysis of spectrum 2 revealed that about half of the lines exhibited a clear emission or emission masked the absorption line to an extent that it could not be measured. All these lines were rejected. The remaining lines were compared with the lines measured in spectrum 1. Their equivalent widths turned out to agree well. However, since spectrum 2 covers a considerably narrower spectral range, is distorted by emission, and has a slightly lower S/N ratio, we did not use the lines of spectrum 2 in our analysis.

Measuring lines involves a number of difficulties which are attributable to line weakness, a high probability of blending, and chemical anomalies. The list of lines with wavelengths and relative intensities that was kindly sent to us from VALD (Kupka *et al.* 1999) at our request served as a basis for line identification. Using

[1] Table 2 is published in electronic form only and is accessible via ftp cdsarc.u-strasbg.fr/pub/cats/J (130.79.128.5) or at http://cdsweb.u-strasbg.fr/pub/cats/J.

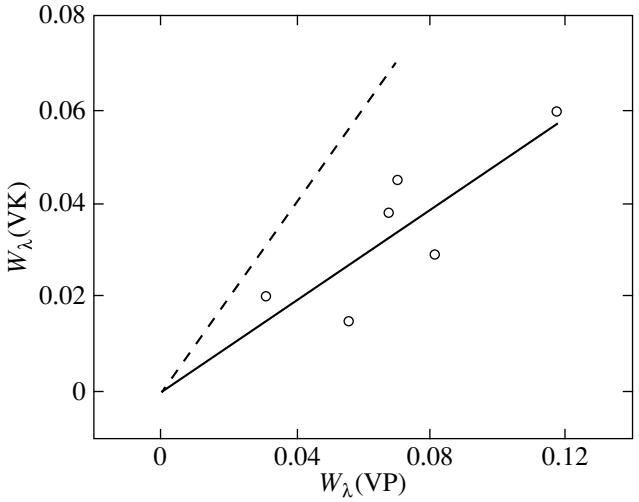

Fig. 1. Comparison of the equivalent widths W_λ(VP) measured by Vitrichenko and Plachinda (2000) with our measured values of W_λ(VK) (circles). The solid line is a least-squares fit, and the dashed line represents the line of one-to-one correspondence.

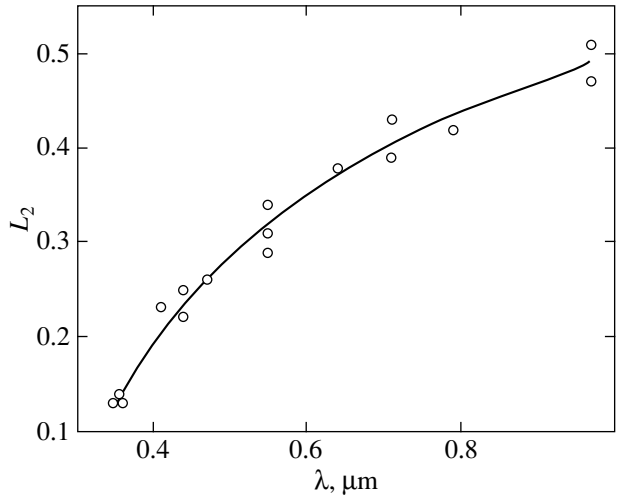

Fig. 2. Wavelength dependence of brightness L_2 for the secondary star. The circles indicate observations, and the solid line represents a fit to the dependence using formula (2).

our program, we searched for each line by wavelength with allowance for its radial velocity, specified a refined continuum spectrum and the boundaries for the line in such a way as to reduce the superposition effect of neighboring lines, and fitted the line profile by a Gaussian. The manual procedures were checked on the screen which displayed the observed spectrum and its fit. The equivalent width was computed twice: as an integral in the boundaries chosen and using a formula for the integral of a Gaussian curve. In the latter case, the continuum spectrum was redetermined. The match between two equivalent-width determinations, within the error limits, served as evidence that the line was measured correctly. The error in the equivalent width was, on the average, 0.004 Å. The lines found were checked by their radial velocities using the 3σ criterion, where $\sigma = 18$ km s^{-1} is the error in the radial velocity estimated from a single line. Subsequently, we rejected lines by their widths. The Gaussian parameter for the line profile was, on the average, 1.1 Å with an error of 0.4 Å. The broadest lines are mostly blends; they were rejected. We also rejected lines with doubtful identification and lines that yielded abundances that disagreed with the mean values according to the 3σ criterion.

From the equivalent-width measurements by Vitrichenko and Plachinda (2000), six lines proved to be common to our measurements. It is of interest to compare these measurements, because the spectrum analyzed by Vitrichenko and Plachinda (2000) was taken during a total eclipse, while our spectra were taken outside eclipse.

Based on the depth of minimum, we can predict that the line equivalent widths must obey the relation $W_\lambda(\mathrm{VK})/W_\lambda(\mathrm{VP}) = 0.56(2)$. The equivalent widths are compared in Fig. 1. The solid straight line is a least-squares fit, whose equation is

$$W_\lambda(\mathrm{VK}) = 0.000(4) + 0.48(5)W_\lambda(\mathrm{VP}).$$

The coefficient of W_λ(VP) satisfactorily agrees with its predicted value. The error of a single equation is 0.009 Å, which is also in satisfactory agreement with the errors of the two series of measurements. The zero free term in the equation for the straight line suggests that there are no systematic differences in the line equivalent width measurements. The agreement between $W_\lambda(\mathrm{VK})/W_\lambda(\mathrm{VP})$ calculated from the depth of minimum and its value calculated from the ratio of observed line equivalent widths also suggests that the main idea of the eclipse pattern is correct: 2/3 of the primary star's surface is obscured during totality.

Popper and Plavec (1976) studied the central intensities of six helium lines in the range 3819–4471 Å both outside eclipse and near "pseudominimum" (the authors' terminology). They found that the helium lines at minimum weakened only slightly, but remained strong enough. This is in conflict with the idea of a total eclipse. Having analyzed the depths of helium lines, the authors calculated the magnitude difference between the components, $1\overset{m}{.}2$. This difference is in good agreement with the B magnitude difference determined by analyzing the continuum spectrum (Vitrichenko and Larionov 1996).

Before using the measured line equivalent widths in our subsequent analysis, we must take into account the radiation from the primary star. This is done by using the formula

$$W_\lambda = W_\lambda(\mathrm{mes})/L_2. \quad (1)$$

Here, W_λ is the true equivalent widths of secondary lines; W_λ(mes) is the measured equivalent widths; and L_2 is the secondary's relative brightness, the ratio of its flux to the system's total flux.

The wavelength dependence of L_2 is shown in Fig. 2. In this figure, wavelengths (in μm) and L_2 taken from

three sources (Bondar' and Vitrichenko 1995; Vitrichenko and Larionov 1996; Vasileĭskiĭ and Vitrichenko 2000) are plotted along the horizontal and vertical axes, respectively. The solid line represents a third-degree polynomial fit to the wavelength dependence of L_2 whose coefficients were calculated by least squares. This polynomial is

$$L_2 = -0.576(4) + 2.932(7)\lambda - 2.99(1)\lambda^2 + 1.13(1)\lambda^3. \quad (2)$$

The errors, in units of the last digit, are given in parentheses near the coefficients. The error of a single conditional equation is 0.02.

Below, when talking about equivalent widths, we have in mind the quantities transformed by using formula (1), but Table 2 gives the original measurements.

ATMOSPHERIC PARAMETERS

The following three atmospheric parameters must be determined for the subsequent analysis: effective temperature $T_{\rm eff}$, surface gravity $\log g$, and microturbulence ξ_t.

The effective temperature of the secondary star was determined by several authors (see Table 3 for a summary). We see from this table that the results are not in satisfactory agreement. Nevertheless, three papers give similar results. An examination of Table 3 leads us to conclude that our temperature of the secondary star agrees well with the results of Poper and Plavec (1976) and Vitrichenko and Larionov (1996), but disagrees with the temperature estimated by Vitrichenko *et al.* (1996) and Vasileĭskiĭ and Vitrichenko (2000). This disagreement is mainly attributable to the use of different eclipse models.

The classical methods of two-dimensional classification use a color index that fixes the effective temperature and a line equivalent width that fixes the surface gravity. Since both these characteristics are distorted because of the star's binary nature, the classical methods are unsuitable in this case.

We used a procedure based on the model-atmosphere method to determine the effective temperature. This procedure involved choosing a grid of models with various effective temperatures, computing the iron abundance from each of the models, and checking this abundance for correspondence to the Boltzmann formula. A correction to the effective temperature was calculated by using the Boltzmann formula. We compared this corrected temperature with that specified in the model and took the temperature with a zero correction as the final value. The idea of the method is that for a given model effective temperature, there must be no dependence of the species abundance on excitation potential if the temperature was chosen correctly. If this dependence is statistically significant, then its slope determines the correction to the effective temperature.

Our temperature determinations are shown in Fig. 3. Here, the model temperature is plotted along the horizontal axis, and the model temperature plus the temperature correction calculated from the Boltzmann formula is plotted along the vertical axis. The dashed line represents the line of one-to-one correspondence for the model temperature, and the solid line represents the calculated temperature. The intersection of these lines yields the sough-for effective temperature of the secondary star.

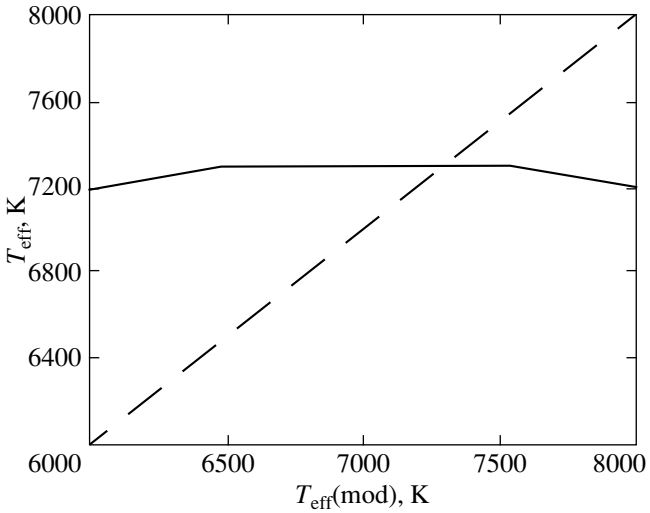

Fig. 3. Effective-temperature determination. $T_{\rm eff}$(mod) is the effective temperature of a model atmosphere, and $T_{\rm eff}$ is the secondary's effective temperature calculated by adding the correction given by the Boltzmann formula to the model temperature (solid line). The dashed line represents the line of one-to-one correspondence for the model effective temperature.

The same technique was applied to the species Si I, Ca I, Cr I, Ti I, and Ti II. The results proved to be the same as those for neutral iron, but the errors were a factor of 2 or 3 larger because of the smaller number of lines.

Finally, we obtained $T_{\rm eff}$ = 7300(100) K. This is the result of the last approximation. For the first approximations, we specified virtually arbitrary values of $\log g$ and ξ_t, which were subsequently refined. Calculations show that the temperature depends weakly both on the above parameters and on chemical composition.

We determined the surface gravity from Fe I and Fe II equilibrium. In Fig. 4, the iron abundance derived

Table 3. A summary of effective-temperature determinations for the secondary star (different eclipse models were used)

Authors	$T_{\rm eff}$, K	Spectral type
Popper and Plavec (1976)	8000–7000	A7–F2
Vitrichenko and Larionov (1996)	7000	F0 V
Vitrichenko *et al.* (1996)	10 400	B9 V
Vasileĭskiĭ and Vitrichenko (2000)	5700	G2 III
This paper	7300	F2

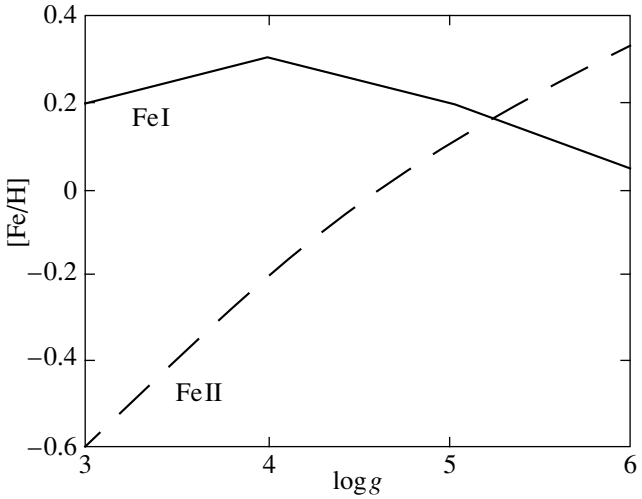

Fig. 4. Iron abundance derived from Fe I (solid curve) and Fe II (dashed curve) lines versus $\log g$.

from Fe I (solid curve) and Fe II (dashed curve) lines is plotted against surface gravity. As we see from Fig. 4, the same abundance is obtained for $\log g = 5.2(3)$. It is important to note that the iron abundance derived from lines of neutral species depends weakly on $\log g$. Conversely, this dependence is considerably stronger for ionized iron. A similar phenomenon is also observed for other species. Therefore, the data obtained from lines of neutral species should be preferred in an abundance analysis.

Similar dependences were constructed for silicon, titanium, and chromium. Si I and Si II give $\log g$ that matches, within the error limits, its value determined from iron, while the dependences for titanium and chromium give a slightly larger $\log g$. However, because the number of lines is small, the errors are considerably larger than those for iron, and the results obtained from titanium and chromium lines may therefore be considered less reliable.

The mass of the secondary star was estimated by solving the radial-velocity curve to be $M_2 = 2.5M_\odot$ (Vitrichenko *et al.* 1996). Using our spectroscopic surface gravity, we can determine the secondary's photospheric radius,

$$R_2 = (M_2 g_\odot / g)^{1/2} = 0.5(2) R_\odot. \quad (3)$$

Here, $g_\odot = 2.7 \times 10^4$ cm s^{-2} is the solar surface gravity. The secondary's photospheric radius was found to be abnormally small. It follows from the solution of light and radial-velocity curves that the eclipsing body has a radius of 8.4(2) $R_\odot$ (Vitrichenko *et al.* 1996), which is a factor of ~17 larger than the photospheric radius. We thus conclude that the eclipsing body cannot be the secondary star itself, but only a dust cloud around it. A similar result was obtained by Vitrichenko and Tsymbal (1996), who showed that the secondary's photospheric radius was a factor of ~4.4 smaller than the radius of the eclipsing body. However, the results are in close agreement only qualitatively; the ratios of radii disagree, within the error limits.

It is crucially important to find a method for verifying the derived surface gravity and photospheric radius of the secondary star. Let us consider two other methods for determining $\log g$.

First method. Assume, as was done by Vasileĭskiĭ and Vitrichenko (2000), that the secondary component has the radius of the eclipsing body, $R_2 = 8.4(2)\ R_\odot$, and mass $M_2 = 2.5(1) M_\odot$ (Vitrichenko *et al.* 1996). Formula (3) then yields $\log g = 3.0(1)$. Recall that under this assumption, the light curve can be explained only if there is a third light in the system. The value of $\log g$ obtained by this method disagrees with its spectroscopic value.

Second method. For this check, we used the Stefan–Boltzmann formula, substituting the surface gravity for the radius in it. The modified formula takes the form

$$M_\mathrm{b} = 30.23 + 2.5 \log g - 10 \log T_\mathrm{eff}. \quad (4)$$

When deriving (4), we assumed the secondary's mass to be $2.5M_\odot$.

We determined the bolometric absolute magnitude M_b of the secondary star from

$$M_\mathrm{b} = V - 2.5 \log L_2 - (m - M) - A_V + \mathrm{BC} = 0\overset{m}{.}3(1). \quad (5)$$

Here, $V = 7\overset{m}{.}95$ is the system's apparent V magnitude; $L_2 = 0.325$ is the secondary's V brightness calculated from (2); $m - M = 8\overset{m}{.}22$ is the system's distance modulus; $A_V = 0\overset{m}{.}7$ is the interstellar extinction; and BC = $0\overset{m}{.}01$ is the bolometric correction, which may be ignored in our case. The main sources of errors are errors in the distance modulus and in the interstellar extinction.

Using formula (4) and M_b calculated from (5), we obtain $\log g = 3.5(1)$ for $T_\mathrm{eff} = 7300$ K. This surface gravity also disagrees with its spectroscopic value, but in satisfactory agreement with its value determined by the first method.

This disagreement can be explained by the presence of a third light in the system whose source can be either a B star or the radiation of a hot dense gas (Vasileĭskiĭ and Vitrichenko 2000). However, under any of the above assumptions, L_2 should be corrected to allow for this radiation. Unfortunately, we cannot correct L_2, because our data are scarce.

The best way out of this situation would be to obtain high-quality spectra near primary minimum. In that case, the depth of secondary lines increases by a factor of 1.8, on the average, which allows us to measure the line equivalent widths more accurately and to solve the problem of their identification and blending better. The first attempt of this kind was made, but only a narrow wavelength range was studied (Vitrichenko and Plachinda 2000).

The microturbulence ξ_t, along with the remaining atmospheric parameters, were determined by successive approximations. Below, we present the results only for the last approximation.

The ATLAS9 code in the STARSP software package was used to compute a model with $T_{\rm eff}$ = 7300 K, $\log g$ = 5.2, and [M/H] = 0. Using this model with several values of ξ_t, we computed the abundance from all Fe I lines and constructed a linear dependence for each ξ_t:

$$[\mathrm{Fe/H}] = a + bW_\lambda. \quad (6)$$

Next, we plotted the coefficient b against ξ_t and took the microturbulence for which $b = 0$ as its true value. An example of this plot is shown in Fig. 5.

It follows from an examination of Fig. 5 that ξ_t = 6(1) km s^{-1}. The error in ξ_t was estimated from the error in b. A similar dependence constructed from Cr I lines yields ξ_t that matches its value determined from iron lines, within the error limits. However, an attempt to estimate ξ_t from Si I, Ca I, and Ti II lines failed. The coefficient b is positive over a wide range of microturbulences for the first two species and negative for Ti II. This is most likely attributable to the small number of lines, to the narrow range of line equivalent widths, and to errors in the equivalent widths and oscillator strengths.

The significance of the deduced atmospheric parameters was checked by three methods.

The *first method* involves calculating the correlation coefficient between the observed spectrum profile and the synthetic spectrum profile computed with the STARSP package. By the spectrum profile, we mean the quantity $1 - I/I_c$, where I is the star's spectrum, and I_c is its continuum spectrum. We used a model atmosphere computed using this package with given atmospheric parameters and with anomalies of the chemical composition (see below) introduced into this model. The observed spectrum was reduced to zero radial velocity. For our analysis, we chose the spectral range 5200–5300 Å without noticeable primary lines. The correlation coefficient for this spectral range was found to be 0.84(2). The large ratio of the correlation coefficient to its error (0.84/0.02 = 42) suggests good agreement between the observed and synthetic spectrum profiles.

An advantage of the method is that it is insensitive to the scaling factor. Therefore, it yields a result that is completely independent of L_2. The method is only slightly sensitive to microturbulence. Since most of the lines in the above spectral range belong to neutral iron, the method is also weakly sensitive to chemical composition.

The *second method* involves comparing the observed and synthetic spectrum profiles by least squares. A linear relation between the profiles was given by

$$r(\mathrm{obs}) = a_1 + b_1 r(\mathrm{syn}). \quad (7)$$

Here, r(obs) is the observed spectrum profile, and r(syn) is the synthetic spectrum profile; a_1 and b_1 can be determined by least squares. It turned out that a_1 = 0.012(1). This quantity characterizes the systematic error in continuum placement associated with the overlapping of weak lines. This correction is large by itself, because the mean central intensity of all measured lines is 0.015; i.e., it is comparable in magnitude to the systematic correction. However, in our procedure for line measurement, the continuum is drawn near each line, and this correction is eliminated. The quantity b_1 was found to be 0.34(1). By its definition, it must match L_2. Formula (2) for the middle of the spectral range yields L_2 = 0.30(2). The agreement may be considered good, confirming that the atmospheric parameters are correct.

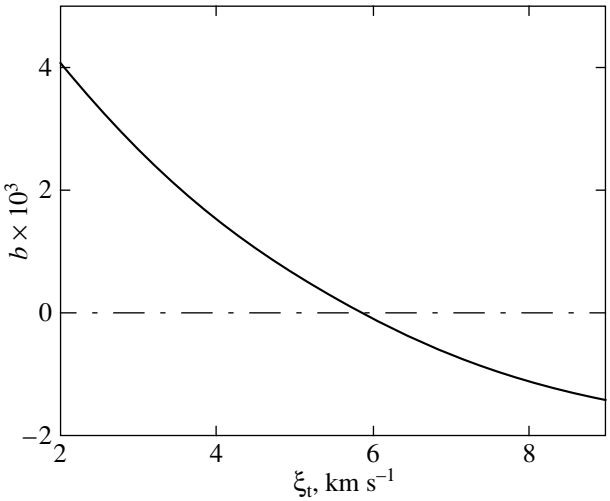

Fig. 5. Dependence of b [see formula (4)] on microturbulence ξ_t constructed from Fe I lines (solid curve). The dashed line was drawn at the b = 0 level.

The *third method* involves a visual comparison of the observed and synthetic spectra. This comparison was made with the MERSEN code developed by V.V. Tsymbal and Ch. Cowley and kindly made available to us. The code uses a model atmosphere computed by the ATLAS9 code and the VALD line list. The MERSEN code varies the oscillator strength in such a way that the observed and synthetic spectra coincide most closely. Since the oscillator strengths and elemental abundances appear in the formula for computing equivalent widths in the form of cofactors, the MERSEN code allows us to adjust either the oscillator strengths or the chemical composition. In this approach, we must apply the correction a_1, as well as reduce the observed spectrum to zero radial velocity and take into account the binary nature of the star by using the formula

$$r = r(\mathrm{obs})/L_2. \quad (8)$$

Here, r is the true spectrum profile corrected for the effect of the primary's radiation.

Figure 6 shows the results of such a comparison. We see from this figure that the observed and synthetic spectra are in satisfactory agreement. The difference between the spectra is largest near 5273 Å. However, as

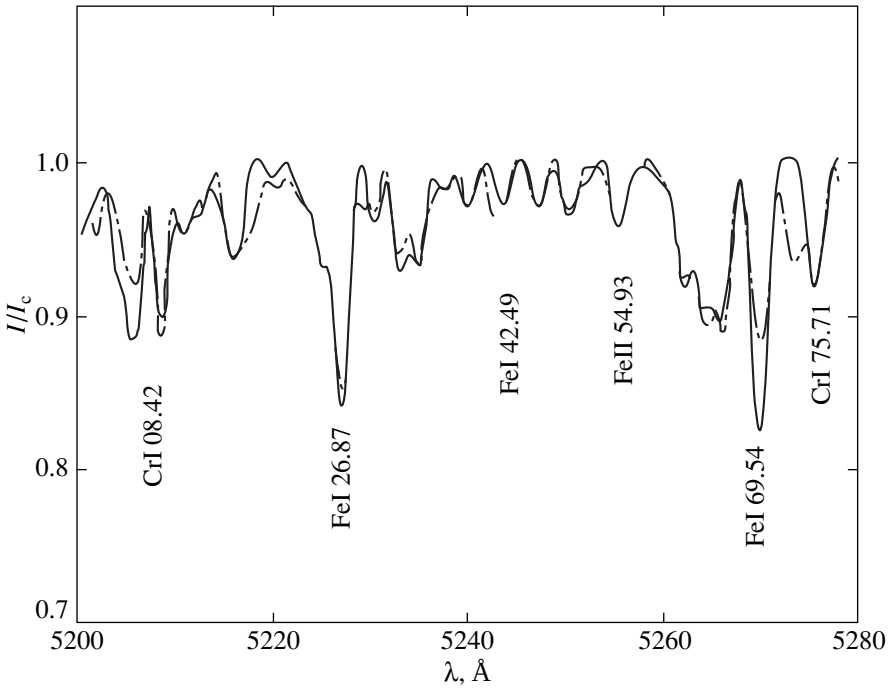

Fig. 6. Comparison of the observed spectrum (dashed line) with the spectrum computed with the MERSEN code (solid line). Some identified lines are marked in the lower part of the figure. The first two digits of the wavelengths were omitted.

an analysis indicates, our line list does not contain the Fe I 5273.16 line whose intensity is slightly below the line selection threshold, while this line is clearly present in the observed spectrum. If we include this line in our line list, then the above difference disappears.

CHEMICAL COMPOSITION OF THE SECONDARY STAR

For our abundance analysis, we used a model atmosphere with the above parameters and with the chemical composition deduced in the first approximation. The model was computed with the ATLAS9 code. We used only the lines listed in Table 2.

The results are summarized in Table 4. The first and second column list species and their VALD solar abundances, respectively. The next two columns give deviations from the solar abundances and the number of lines used. For comparison, the following columns give the chemical composition of V1016 Ori (Vitrichenko and Klochkova 2000) and the mean chemical composition for stars of the old cluster M 15 (Sneden *et al.* 1997).

A comparison of the chemical compositions for the secondary component of BM Ori and V1016 Ori indicates that most of the elements have similar abundances. Only nickel and titanium are more abundant in the latter star. However, since only one line was measured for these species, the difference cannot be considered statistically significant.

For old stars of the cluster M 15, iron shows the largest abundance difference: old stars have an underabundance of ~2.5 dex, a well-know fact. Another difference is that almost all elements in old stars are more abundant. Scandium, titanium, and vanadium, which are less abundant than they are in the secondary component of BM Ori, constitute an exception. Only the nickel abundance in the secondary star of BM Ori matches that in stars of the cluster M 15, within the error limits, and simultaneously agrees with its solar abundance.

A preliminary chemical composition was previously determined from the line equivalent widths given in Table 2; it shows large abundance anomalies (Vitrichenko and Plachinda 2000). Here, we failed to confirm our previous results, because we used distinctly different atmospheric parameters.

EMISSION LINES

The light curve of BM Ori is known to be photometrically unstable (Bondar' and Vitrichenko 1995). However, none of the researches has been able to detect any changes in the spectrum. Clearly, photometric variability must show up in spectroscopic variability.

About half of the lines detected in spectrum 2 exhibit a blueshifted emission component. Several sample line profiles with the emission component are shown in Fig. 7.

It follows from an analysis of data similar to those in Fig. 7 that the emission feature is observed for various species, and that its shift is –50(10) km s^{-1}, which is a factor of ~4 higher in absolute value than the speed of sound.

Table 4. Chemical composition of the secondary star of BM Ori

Species	Sun	BM Ori		V1016 Ori		M 15
		[X/H]	*N*	[X/H]	*N*	[X/H]
Li I	–10.9	3.2(4)	2			
C I	–3.2	0.3(1)	3	–0.1(1)	9	
Na I	–5.7	0.0(3)	4			0.2(3)
Mg I	–4.5	–1.3(3)	6	–0.3	1	0.4(3)
Al I	–5.6	–0.1	1	–0.2(2)	2	0.8(3)
Si I	–4.5	0.1(1)	25	0.1(2)	15	0.6(2)
Si II	–4.5	–0.2(1)	2			
S I	–4.8	0.2(1)	2	0.6(3)	2	
Ca II	–5.7	–0.2(1)	20			0.24(5)
Sc II	–8.9	0.6(1)	9			–0.1(1)
Ti I	–7.0	1.08(4)	10	1.9	1	0.5(2)
Ti II	–7.0	0.6(1)	11			
V I	–8.0	2.8(2)	22			0.0(1)
V II	–8.0	3.4(3)	12			
Cr I	–6.4	1.0(1)	19			
Cr II	–6.4	0.7(2)	10			
Mn I	–6.6	0.5(2)	11			
Fe I	–4.37	0.04(3)	145	0.4(1)	20	–2.40(4)
Fe II	–4.4	0.0(1)	29			
Co I	–7.1	2.5(1)	15			
Ni I	–5.79	0.3(1)	30	1.0	1	0.1(1)
Cu I	–7.8	–0.7	1			
Zn I	–7.4	–0.3(1)	2	1.8(1)	3	
Y II	–8.0	0.9(2)	11			
Ba II	–9.5	–0.2(2)	4			0.1(2)

As we see from Table 1, spectrum 2 was taken near conjunction, when the side of the secondary heated by the primary faced the observer. The secondar's atmosphere (or its surrounding dust envelope) completely fills the Roche lobe. The Lagrangian point L_2 lies near the secondary's surface. The hot gas from the secondary's heated region most likely flows onto the primary.

Spectrum 1 was also taken near (different) conjunction. At this time, the cooler side of the secondary star faced the observer. Therefore, the hot gas is invisible, being screened by the secondary's disk and/or by its dust envelope.

DISCUSSION

One of our main objectives is to compare the photospheric radius determined from spectroscopic observations with the radius of the eclipsing body estimated by solving the light and radial-velocity curves. If these radii are equal, within the error limits, then the eclipsing body is a G2 III star and there is a third light, presumably a hot B0 VI subdwarf, in the system (Vasileĭskiĭ and Vitrichenko 2000). If, however, the secondary's spectroscopic radius is considerably smaller than its geometric radius, then the eclipsing body is a dust cloud that surrounds the secondary star and is the source of continuum infrared excess (Vitrichenko and Larionov 1996; Vitrichenko 1998a, 1998b).

It should be immediately noted that we failed to give a definitive answer to the above question.

Here, we spectroscopically obtained a surprisingly small photospheric radius for the secondary component, $R_2 = 0.5R_\odot$. The star's mean density is ~20 g cm^{-3}, i.e., a factor of ~10 higher than that of the Sun. However, the spectroscopic surface gravity $\log g = 5.2(2)$ disagrees with $\log g = 3.5(1)$ determined from the bolometric absolute magnitude and temperature. The discrepancy cannot be explained by errors. It must be assumed that the bolometric absolute magnitude was overestimated, because the emission from yet another source of light fell within the aperture.

If there is indeed a third light in the system, then we must correct L_2 and recalculate the equivalent widths. Since spectroscopic observations show no evidence of a third light, we cannot take it into account and recalculate the equivalent widths.

It follows from an examination of Fig. 4 that the abundance deduced from neutral species depends weakly on surface gravity. Therefore, despite a possible large error in $\log g$, the chemical composition was determined reliably.

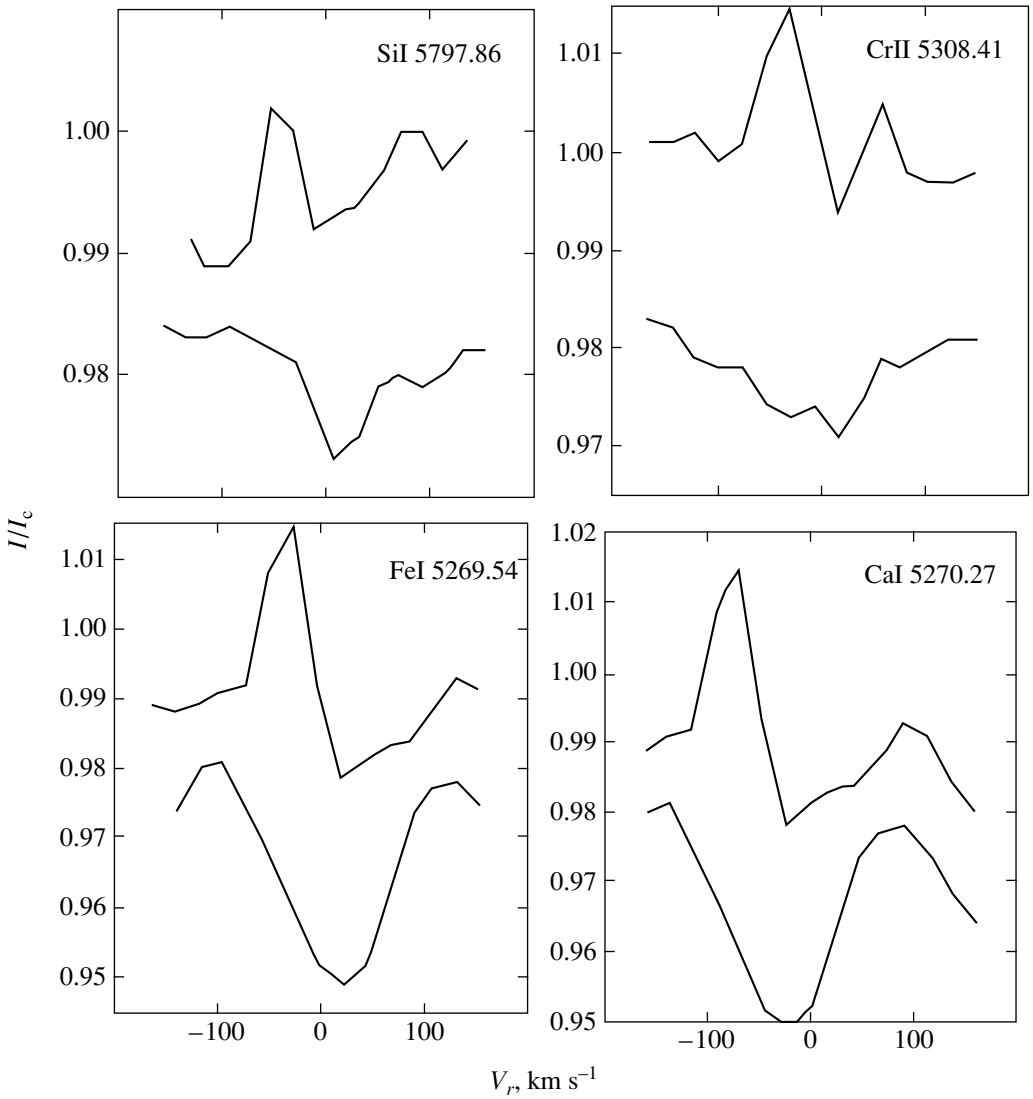

Fig. 7. Sample line profiles showing emission. The upper and lower profiles are spectra 2 and 1, respectively. The wavelength scale (in km s^{-1}) is along the horizontal axis; the mean radial velocity was subtracted. Spectrum 1 was arbitrarily displaced downward by 0.015 in fractions of the continuum spectrum.

Our effective temperature, $T_{\rm eff}$ = 7300 K, proved to be considerably higher than that from Vasileĭskiĭ and Vitrichenko (2000), $T_{\rm eff}$ = 5700 K. The reason is that a different eclipse model was taken in the above study: the secondary star with radius $8.2R_\odot$ obscures the primary star during eclipse. In that case, $\log g$ = 3.0(1); i.e., the disagreement with the "spectroscopic" surface gravity becomes even larger.

It is of interest to check whether the secondary's radial velocities in Table 1 agree with the radial-velocity curve from Vitrichenko *et al.* (1996). For spectra 1 and 2, the measured velocities were found to be the same, 132–26 = 106 km s^{-1}. The radial-velocity curve can be described by the law

$$V_r = 15 + 170\sin\varphi, \qquad (9)$$

where φ is the phase. This formula yields radial velocities of 72 and 82 km s^{-1} for spectra 1 and 2, respectively. The O–C values are +34 and +24 km s^{-1}. This difference exceed the errors, which cannot be larger than 2 km s^{-1}. A similar discrepancy was already pointed out by Vitrichenko and Plachinda (2000), who obtained O–C = +27 km s^{-1} near totality. Popper and Plavec (1976) also note several cases where O–C ~ +20 km s^{-1}, with the spectrograms being taken near elongations. A possible explanation of this effect is an occasional shrinkage of the secondary star. For spectrum 2, the atmosphere shrinks with the simultaneous outflow of hot gas toward the primary star.

A different explanation of the occasional increase in radial velocity is also possible. If there is indeed a massive third body in the system close to the eclipsing pair, then the radial-velocity variations in the secondary component are attributable to its revolution around the center of mass. In this case, negative O–C values must also be occasionally observed, which have not yet been detected.

Blueshifted emission components of spectral lines were first detected in the second spectrum. This can be key to understanding stellar flares. Recently, Bisikalo *et al.* (1999, 2000) performed three-dimensional simulations of mass outflow from the secondary onto the primary in semidetached systems. They showed that collisions of gas flows in the system generated spiral shock waves. These effects may produce line emission and flares (Bondar' and Vitrichenko 1995). Other new results were also obtained in the above studies, which can be applied to BM Ori. First, it was shown that a disk does not necessarily form around the primary star in the case of mass outflow. Second, matter leaves the system under certain conditions. Third and this is of greatest interest, the matter outflowing from the secondary star can turn around the primary star and return to the secondary. In that case, it becomes clear how a dust cloud can form around the secondary component.

Since the spectrum for the secondary component of BM Ori is very difficult to analyze, our results are preliminary. A higher level of investigation can be reached if high-quality spectra of the star will be obtained during totality.

CONCLUSION

Having analyzed out-of-eclipse spectrograms for BM Ori, we managed to identify and measure ~400 secondary lines. Our analysis of these lines allowed us to determine the secondary's atmospheric parameters: $T_{\rm eff} = 7300$ K, $\log g = 5.2$, and $\xi_t = 6$ km s^{-1}.

We found the secondary's photospheric radius from the above spectroscopic surface gravity to be $R_2 = 0.5R_\odot$, which is a factor of 17 smaller than the radius of the eclipsing body calculated by solving the light and radial-velocity curves. This fact argues for the hypothesis that the eclipsing body is a dust envelope around the secondary star. However, the spectroscopic surface gravity disagrees with its value calculated from the luminosity and temperature, and we failed to explain this effect.

We determined the atmospheric chemical composition. The C, Na, Al, Si, S, Ca, Fe, Ni, and Zn abundances are solar, within the error limits. Li, Sc, Ti, V, Cr, Mn, Co, and Y are overabundant, while Mg, Cu, and Ba are underabundant. In general, the secondary component is similar in chemical composition to the star V1016 Ori (Vitrichenko and Klochkova 2000). The chemical composition of the secondary star of BM Ori is also compared with the mean chemical composition of the old cluster M 15. The largest difference is the well-known iron underabundance in old stars.

One of the spectra exhibits an emission component in spectral lines shifted by –50 km s^{-1}, which is evidence of mass outflow from the secondary's atmosphere. The radial velocity determined from the two spectra has a systematic difference of ~30 km s^{-1} compared to that calculated from the radial-velocity curve, which cannot be explained by measurement errors. A plausible explanation of this fact is an occasional shrinkage of the secondary's atmosphere.

ACKNOWLEDGMENTS

We wish to thank the staff of the Vienna Atomic Line Data (VALD) Center for the data on spectral lines (Kupka *et al.* 1999), and V.V. Tsymbal for the STARSP and MERSEN software, which we extensively used here. We are also grateful to D.V. Bisikalo, T.A. Ryabchikova, and V.L. Khokhlova for helpful discussions.

REFERENCES

1. D. V. Bisikalo, A. A. Boyarchuk, V. M. Chechetkin, *et al.*, Astron. Zh. **76**, 905 (1999) [Astron. Rep. **43**, 797 (1999)].
2. D. V. Bisikalo, A. A. Boyarchuk, O. A. Kuznetsov, and V. M. Chechetkin, Astron. Zh. **77**, 31 (2000) [Astron. Rep. **44**, 26 (2000)].
3. N. I. Bondar' and É. A. Vitrichenko, Pis'ma Astron. Zh. **21**, 700 (1995) [Astron. Lett. **21**, 627 (1995)].
4. C. Doremus, Publ. Astron. Soc. Pac. **72**, 745 (1970).
5. F. Kupka, N. E. Piskunov, T. A. Ryabchikova, *et al.*, Astron. Astrophys. **38**, 119 (1999).
6. V. E. Panchuk, I. D. Naĭdenov, V. G. Klochkova, *et al.*, Byull. Spets. Astrofiz. Obs. **44**, 127 (1998).
7. J. S. Plaskett and J. A. Pearce, Publ. Dom. Astrophys. Obs. Victoria BC **1**, 1 (1931).
8. D. M. Popper and M. Plavec, Astrophys. J. **205**, 462 (1976).
9. C. Sneden, R. P. Kraft, M. D. Snetsone, *et al.*, Astron. J. **114**, 1964 (1997).
10. O. Struve and J. Titus, Astrophys. J. **99**, 84 (1944).
11. A. S. Vasileĭskiĭ and É. A. Vitrichenko, Pis'ma Astron. Zh. **26**, 613 (2000) [Astron. Lett. **26**, 529 (2000)].
12. É. A. Vitrichenko, Pis'ma Astron. Zh. **22**, 587 (1996) [Astron. Lett. **22**, 523 (1996)].
13. É. A. Vitrichenko, Pis'ma Astron. Zh. **24**, 708 (1998a) [Astron. Lett. **24**, 611 (1998a)].
14. É. A. Vitrichenko, Preprint No. 1991, IKI RAN (Space Research Institute, Russian Academy of Sciences, 1998b).
15. É. A. Vitrichenko and V. G. Klochkova, Pis'ma Astron. Zh. **26**, 133 (2000) [Astron. Lett. **26**, 104 (2000)].
16. É. A. Vitrichenko and V. M. Larionov, Pis'ma Astron. Zh. **22**, 178 (1996) [Astron. Lett. **22**, 157 (1996)].
17. É. A. Vitrichenko and S. I. Plachinda, Pis'ma Astron. Zh. **26**, 456 (2000) [Astron. Lett. **26**, 390 (2000)].
18. É. A. Vitrichenko and V. V. Tsymbal, Pis'ma Astron. Zh. **22**, 132 (1996) [Astron. Lett. **22**, 116 (1996)].
19. É. A. Vitrichenko, V. S. Shevchenko, and V. A. Shcherbakov, Pis'ma Astron. Zh. **22**, 185 (1996) [Astron. Lett. **22**, 163 (1996)].
20. M. M. Zakirov and V. S. Shevchenko, Perem. Zvezdy **21**, 629 (1982).

Translated by V. Astakhov

Astronomy Letters, Vol. 27, No. 5, 2001, pp. 338–344. Translated from Pis'ma v Astronomicheskiĭ Zhurnal, Vol. 27, No. 5, 2001, pp. 393–400.

Infrared Photometry of Five Long-Period Binaries

O. G. Taranova* and V. I. Shenavrin

Sternberg Astronomical Institute, Universitetskiĭ pr. 13, Moscow, 119899 Russia

Received October 5, 2000; in final form, December 22, 2000

Abstract—We present and discuss *JHKLM* photometry for five long-period binaries (VV Cep, ZZ CMi, WY Gem, ε Aur, and ζ Aur). The IR radiation from WY Gem may contain a component with a period of ~430 days, attributable to temperature pulsations of an M supergiant. The 3.5- and 5-μm radiation from the eclipsing binary ε Aur outside the eclipse exhibits excess (relative to the light from an F supergiant) fluxes which correspond to the emission from a cool source with a temperature of ~1000 K. For the eclipsing binary ε Aur, we present the hitherto unpublished results of our optical and IR photometry during 1982–1985, when a primary eclipse was observed in the system. © *2001 MAIK "Nauka/Interperiodica"*.

Key words: *long-period variables, infrared photometry*

INTRODUCTION

The star ζ Aur is the prototype of long-period binaries whose components are a K giant and a hot companion (typically a main-sequence star). These stars have been extensively studied for more than 70 years. Being eclipsing systems, they give an excellent opportunity for determining accurate masses and radii of late-type stars. ζ Aur was observed several times during its 1993 and 1995 eclipses with the Hubble Space Telescope (HST) as part of the program of research on the extended atmospheres of K supergiants. Based on these data, Bennet and Harper (1996) determined fundamental stellar and orbital parameters of the system.

VV Cep (in the Cep OB2 association, in the NGC 7160 region) is the prototype of a small class of long-period binary systems consisting of an M supergiant and a hot dwarf or giant, mostly of spectral type B. Apart from TiO absorption bands, their spectra show numerous Fe II emission lines, which does not rule out their classification as symbiotic binaries. For example, Buss and Snow (1988) placed our program long-period system WY Gem (in the Gem OB1 association) with an M supergiant and a B star as its components into the class of VV Cep stars. On the other hand, an UV excess in its radiation allowed Sahade *et al.* (1984) to class the object with symbiotic stars.

The rarely observed star ZZ CMi is classified in the GCVS Catalog (Kholopov *et al.*, 1985–1990) as a semiregular variable of spectral type M6 I–IIep with a possible period of ~500 days, which was derived by Chernova (1949) from photographic observations spanning about 40 years. The spectroscopic observations of Sanford (1947) revealed absorption components typical of M6 stars and low-excitation emission lines. Subsequently, Iijima (1984), who observed high-excitation [Ne III] and [O III] lines, and almost simultaneously Bopp (1984), who carried out IR observations, placed ZZ CMi into the class of symbiotic stars. Based on the star's *UBV* photometry in 1991, Zamanov and Tomov (1992) confirmed this classification.

The star ε Aur is an F supergiant in a spectroscopic binary system with a puzzling component that partially eclipses the visible star for 2 years every 27.1 years. The maximum fraction of the eclipsed primary component is ~48%. The eclipsing light curve has a long, flat minimum. The eclipse is almost gray in the spectral range 0.4–5 μm. The shallower eclipse observed at wavelengths longer than 5 μm means a contribution of thermal emission from a source with a color temperature of ~500 K (Backman *et al.* 1984). Despite numerous studies, as yet there is no universally accepted model for the system's secondary component. In their most recent paper, Lissauer *et al.* (1996) point out that the cool and dark secondary component of ε Aur is a geometrically thin, extended (~5–10 AU) gas–dust disk (gas and dust are uniformly mixed), which is elongated in the direction parallel to the orbit and surrounds one or two invisible stars located almost at the center of the disk rotating about its axis. According to these authors, the gray eclipse in the visible and near-IR ranges implies that the grain sizes in the disk are much larger (>5 μm) than those in typical circumstellar dust envelopes. Gershberg (1990) suggested that the system's primary component is a white dwarf that experiences a prolonged symbiotic-nova-type outburst (e.g., as in PU Vul); i.e., ε Aur is yet another white dwarf that mimics a supergiant.

* E-mail address for contacts: taranova@sai.msu.ru

1063-7737/01/2705-0338$21.00 © 2001 MAIK "Nauka/Interperiodica"

Table 1. General parameters of the program stars

Object	Type	V_{var}	Period, days	Sp	$E(B–V)$	r, pc	Reference*
ζ Aur	EA/GS	3.70–3.97	972.16	K5 II+B7 V	0.08	261	1
VV Cep	EA/GS+SRC	4.80–5.36	7430	M2 EPIA-IAB+B8 : EV	0.35	830	2
ZZ CMi	SR	10.2–11.9	500	M6 I-IIEP		(1300)	This study
WY Gem	LC+E	8.89–9.8	–	M2 EPIAB+B2V-B3V	0.36	1800	2
ε Aur	EA/GS	2.97–3.83	9892	A8 IA-F2EPIA+BV	0.40	600	3, 4

* (1) Bennet and Harper (1996); (2) Buss and Snow (1988); (3) Heintz and Cantor (1994); (4) Weaver and Torres-Dodren (1995).

In the early 1980s, during a primary eclipse of the long-period binary ε Aur, we carried out optical and IR observations (the data have not yet been published). In the mid-1990s, we resumed our IR observations of this system, and the list was extended to include two more well-known long-period binaries, ζ Aur and VV Cep. In addition, the two symbiotic (?) systems ZZ CMi and WY Gem were included in the list.

In this paper, we analyze our photometry of the above objects in an effort to study the physical parameters of individual components of long-period binaries.

OBSERVATIONS

Before 1985, we performed optical and IR photometry of ε Aur with a two-channel photometer (Moroz *et al.* 1979). After 1985, our photometry in the standard *JHKLM* system for all the stars under study was obtained by using a photometer with a liquid-nitrogen-cooled InSb detector (Nadzhip *et al.* 1986). The photometer is mounted at the Cassegrain focus of the 1.25-m telescope at the Crimean Station of the Sternberg Astronomical Institute; the exit aperture is ~12″. The photometric standards were stars from the catalog by Johnson *et al.* (1966): BS 1454 (for ε Aur and ζ Aur), BS 2854 (for ZZ CMi), BS 2134 (for WY Gem), and BS 8334 (for VV Cep). The star BS 1689 from the same catalog was used as the *UBVR* photometric standard for ε Aur. When necessary, the *HLM* magnitudes of the standards were estimated from their spectral types by using relations from Koornneef (1983). The photometric error of a single measurement for stars generally did not exceed a few hundredths of a magnitude.

General information about the stars under study is presented in Table 1. Its columns list, respectively, variability types, *V* magnitude ranges, variability periods, spectral types of the binaries' components (Kholopov *et al.* 1985–1990), $E(B–V)$ color excesses, distances (r) to the systems, and references to the papers in which the last two parameters are given.

Table 2[1] presents our *JHKLM* photometry for the long-period binaries and our *UBVR* photometry for the eclipsing binary ε Aur before and during the 1983–1984 eclipse. Figure 1a–1d shows phase variations of the *J* brightness and *J–K* color index for the four long-period variables (see below).

In the two-color diagram (Fig. 2), the circles denote the observed mean *J–K* and *K–L* color indices with their standard deviations; lines (1) and (2) refer to color variations in normal stars (giants and supergiants); and the dotted line represents color variations in blackbody radiation when the blackbody temperature changes from 3500 to 7500 K. The mean color indices are provided for the eclipsing binary ε Aur outside eclipse. The color indices in Fig. 2 were corrected for interstellar reddening with $E(B–V)$ from Table 1.

DISCUSSION

Table 2 leads us to conclude that the *JHKLM* brightness variations in the long-period variables under study (except for ε Aur) were in the range $0\overset{m}{.}10–0\overset{m}{.}15$ during our monitoring and were not much larger that the observational errors. The brightness variations in the eclipsing binary ε Aur during and outside eclipse (except the descending and ascending branches) did not exceed $0\overset{m}{.}10–0\overset{m}{.}15$ either.

ζ Aur. According to the light elements JD(minI) = 2 427 692.825 + 972.16*E* (Kholopov *et al.* 1985–1990), our IR photometry of this binary spans slightly more than one period. It is evident from Table 2 and Fig. 1a that at various phases of orbital variability, we observed no IR brightness variations in the binary that would appreciably exceed the observational errors. One or two dates of observations, when the IR brightness variations reached $\sim 0\overset{m}{.}15$ on adjacent nights, constitute an exception. In other words, more than 90% of the near-IR (1.25–5 μm) radiation belongs to the cool K giant ($J–K \sim 1^m$), and there is no clear evidence of radiation from the secondary component (a B7 V star), even near the primary eclipse at $\Phi \sim 0.04$ (unfortunately, no observations are available at $\Phi = 0$). In the two-color diagram (Fig. 2), ζ Aur lies near the branch of normal (K5–M1) supergiants, and there is no color excesses that could be attributed to the emission from a relatively hot dust envelope.

[1] Table 2 is published in electronic form only and is accessible via ftp cdsarc.u-strasbg.fr/pub/cats/J (130.79.128.5) or at http://cdsweb.u-strasbg.fr/pub/cats/J.

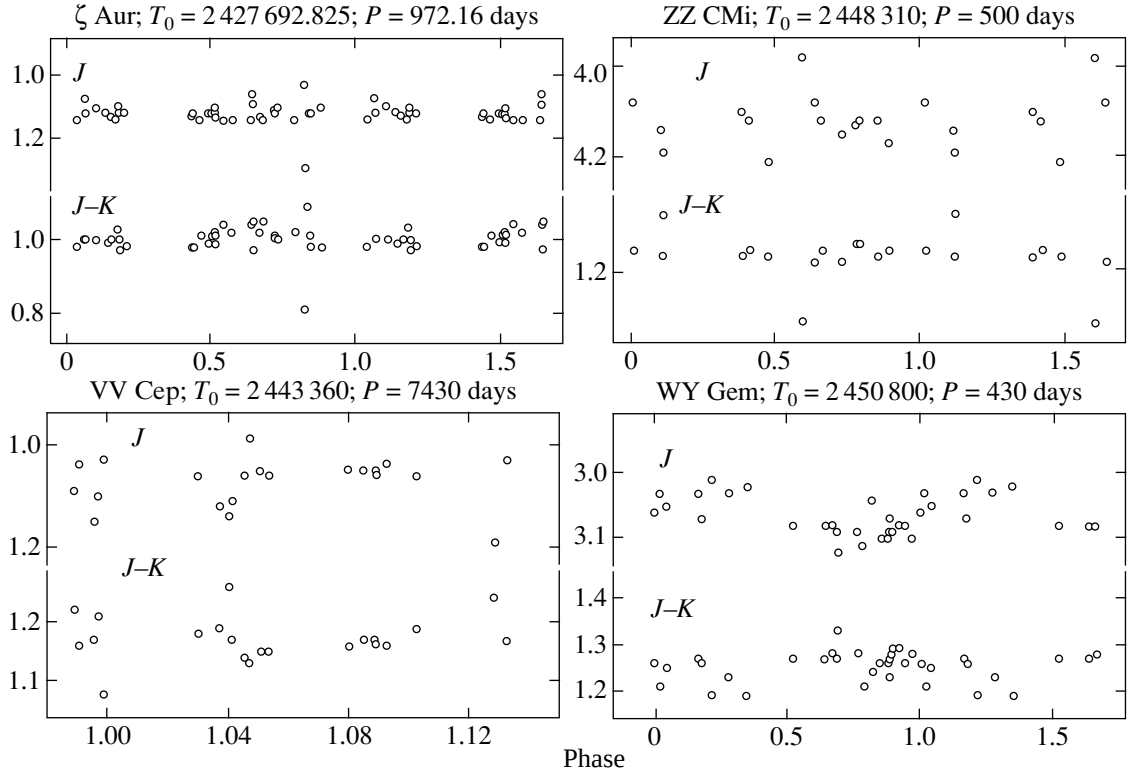

Fig. 1. Phase light and color curves for four long-period variables. The star names and light elements are shown above each panel.

VV Cep. According to the light elements JD(minI) = 2 443 360 + 7430 *E* (Kholopov *et al.* 1985–1990), our IR photometry of this binary refer to orbital phases near primary eclipse (Φ ~ 0.98–1.17), i.e., to maximum visibility of the system's cool component. The observed IR brightness variations did not exceed $0\overset{m}{.}2$ (Table 2). In the two-color diagram (Fig. 2), judging by its mean *J–K* color index, the star lies in the region of K5–M1.5 supergiants; the observed mean *K–L* color index is slightly larger (by ~$0\overset{m}{.}05$) than that for normal K5–M1.5 stars but smaller than that for a blackbody source with a temperature of ~3500 K; i.e., we can say that, as in the case of ζ Aur, we detected no excess IR emission at 3.5 μm (and also at 5 μm).

ZZ CMi. Our IR observations of this variable span about one and a half periods, as suggested by the light elements JD(BV min) = 2 448 310 + 500*E* (Zamanov and Tomov 1992). The IR brightness variations are no larger than $0\overset{m}{.}2$, and the 500-day period does not show up in the *J* brightness and *J–K* color variations (Table 2 and Fig. 1c). In the two-color diagram (Fig. 2), the star is located near normal M4.5–M5 giants. This conclusion refers to the observed *J–K* and *K–L* color indices with no correction for interstellar reddening. We did not find any excess emission (relative to the radiation from an M4.5–M5 giant) at 3.5 and 5 μm.

WY Gem. We observed this system in the infrared several times during 1984–1986 and more than twenty times during 1997–2000. Our photometry revealed a periodicity with P ~ 430 days and JD(max) = 2 450 907(±10) + 430(±7) *E* in the star's IR radiation (Fig. 1d). The *J*-band amplitude is about $0\overset{m}{.}1$, and the *J–K* color index from maximum to minimum *J* brightness decreases by a few hundredths of a magnitude; i.e., the cool star is hotter by about 100 K at maximum *J* brightness than it is at minimum *J* brightness (in the blackbody approximation). In other words, the cool star in WY Gem probably undergoes temperature pulsations with ΔT ~ 100 K and a period of ~430 days. Note that the amplitude of the IR brightness variations in WY Gem is low, and the 430-day period needs to be checked and confirmed. In the two-color diagram, the star virtually lies on the branch of M2–M2.5 supergiants. No IR excess is observed.

ε Aur. The observed IR brightness and color variations in the eclipsing binary ε Aur during and outside eclipse (except for the IR brightness variations on the descending and ascending branches) did not exceed $0\overset{m}{.}10$–$0\overset{m}{.}15$, as illustrated by Fig. 3, where the *J* brightness and *J–K* color of the eclipsing star during 1980–2000 are plotted against the orbital phase that was calculated by using the relation

$$\text{JD(minI)} = 2\,435\,629 + 9892E,$$

(Kholopov *et al.* 1985–1990).

The same figure shows *U* brightness and *U–B* color variations near totality. The spectral types that corre-

spond to the *J–K* and *U–B* colors corrected for interstellar reddening are plotted along the right vertical axis. The circles and crosses represent our observations and the data from Backman *et al.* (1984), respectively. The photometric errors in *J–K* are less than $|0^m.03|$. However, they result in large uncertainties when estimating the star's spectral type (and, consequently, its temperature) from the *J–K* color index, because this parameter depends weakly on temperature variations for $T > 7000$ K. We see from Fig. 3 that the *J*-brightness variations during eclipse at phases ~0.98–1.02 were nearly sinusoidal with a period of ~300–400 days, a minimum at phase 0.99 (upward arrow), a maximum at phase ~1.01 (downward arrow), and an amplitude $\Delta J \sim 0^m.15$. Similar wave-like variations are also clearly seen in *J–K*. The observed *J* brightness and *J–K* color variations during eclipse may be related to the structure of the eclipsing component and to pulsations of one of the components. The *J* brightness peak and the simultaneous decrease in *J–K* in mideclipse are also clearly seen in the optical range (Fig. 3, *U* brightness and *U–B* color variations); they are well known as the brightening and bluing effects in the binary's mideclipse. On the other hand, it may well be that fading and reddening are observed during eclipse to the left and to the right from this normal level.

During totality, the *J–K* color variations reached $\sim 0^m.42$–$0^m.32$, which, given the interstellar reddening and photometric errors, corresponds to temperature pulsations [(7100–7900) ± 200] K or to changes in a supergiant's spectral type from F2 to A2 (Fig. 3). Table 3 lists mean epochs of observations of this binary during and outside eclipse with the corresponding mean brightness and colors (and their standard deviations, SD). *N* is the number of averaged nights. All magnitudes were corrected for interstellar extinction with $E(B–V) = 0^m.4$ (Table 1). The colors are given together with the corresponding supergiant spectral types (Johnson 1966). The last column contains differences between the mean magnitudes during and outside eclipse; their values from Backman *et al.* (1984), who determined then from differences between the magnitudes at the second contact and before eclipse, are given in parentheses.

Analyzing the photometric state of ε Aur (Table 3) during and outside primary eclipse, the following can be noted:

(i) The 0.7–2.2 μm (*R*, *J*, *H*, and *K*) radiation from the binary outside and during eclipse, with an error in the flux of less than 10%, can be described by the radiation from a normal F0 supergiant.

(ii) The neutral fading during eclipse in this range is, on the average, $0^m.70 \pm 0^m.02$; i.e., about half of the supergiant's visible disk is shielded during eclipse. In the 1.25–2.2 μm range (*JHK*), our data match those of Backman *et al.* (1984) with an accuracy of $\pm(0^m.01$–$0^m.02)$.

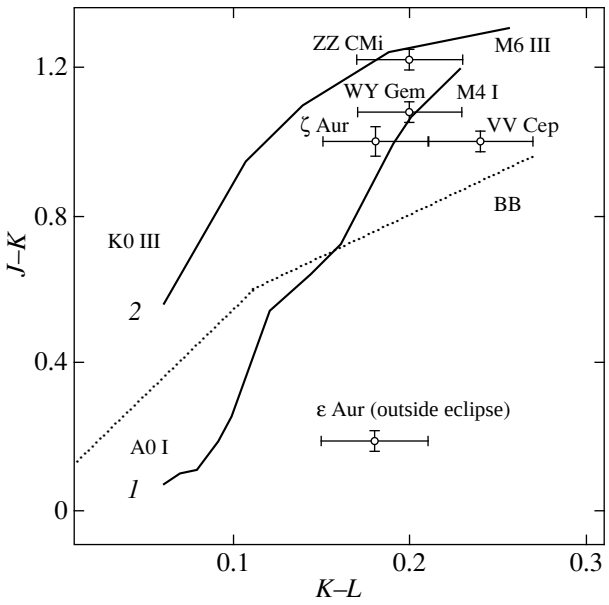

Fig. 2. The [(*J–K*), (*K–L*)] two-color diagram. The open circles denote the mean color indices for the program stars; the vertical and horizontal bars drawn through the mean values represent their standard deviations. Lines (*1*) and (*2*) refer to color variations in normal stars (giants and supergiants). The dotted line represents color variations of the radiation from a blackbody when its temperature changes from 3500 to 5000 K.

(iii) Excess (relative to the radiation from an F0 supergiant) radiation is observed in the optical range (0.36–0.45 μm). The *U–B* color index of the excess radiation is $\sim -1^m.7$ outside eclipse and less than -2^m during eclipse. Such values are characteristic of ionized-gas radiation, with the gas temperature during eclipse being slightly lower than that outside eclipse.

Table 4 summarizes our estimates of the binaries' parameters, which were obtained from averaged IR photometry. The spectral types [Sp(*J–K*)] and temperatures [$T_{\rm eff}$, K (John)] were estimated for each star from the observed mean *J–K* color indices (the second column of Table 4) and by using tables from Johnson (1966) and Koornneef (1983). The total fluxes [$F_{\rm tot}$, erg s^{-1} cm^{-2}], luminosities [$L/L_\odot$], and $M_{\rm bol}$ were derived from the mean *J* fluxes and from the distances to the stars (Table 1). The mean *J* and *J–K* values in Table 4 were corrected for interstellar extinction (with the exception of the data for ZZ CMi). With our classification for ZZ CMi (= M5 III) and with the star's total flux from Table 4, we estimated the distance to the star to be ~1.3 kpc if $M_{\rm bol}$(M5 III) ~ $-4^m.45$ (Tsuji 1978).

Out-of-eclipse radiation from ε Aur at λ ≥ 2.2 μm. The mean *K–L* color indices outside eclipse (Fig. 2)

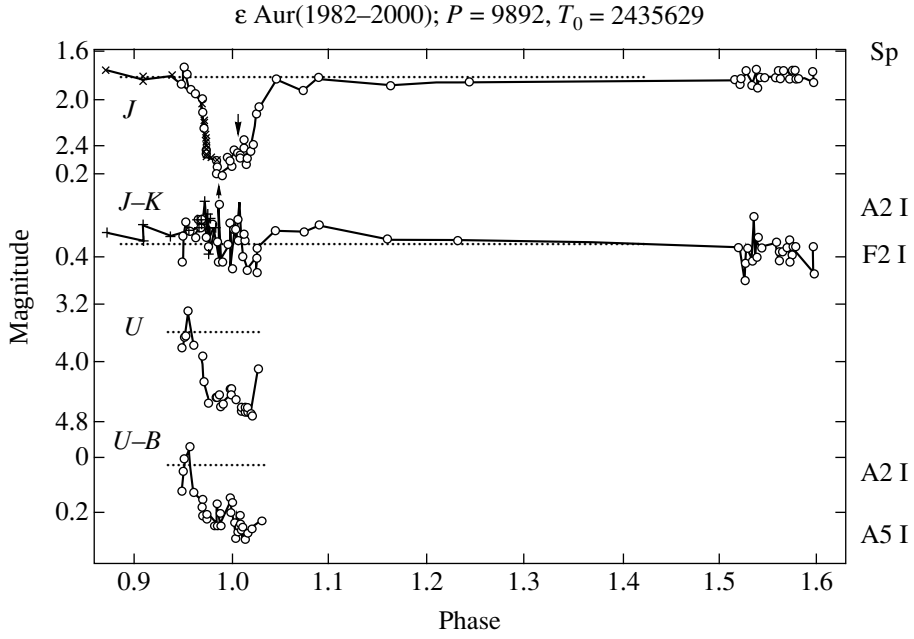

Fig. 3. Phase variations in the *J* brightness and *J–K* color of the eclipsing binary ε Aur during 1980–2000 as well as in its *U* brightness and *U–B* color near primary minimum. The open circles are our observations, and the crosses are the data from Backman *et al.* (1984). The horizontal lines are the mean out-of-eclipse values.

exceed their values for normal stars; i.e., ε Aur appears cooler and brighter than an F0 supergiant at $\lambda \geq 2.2$ μm. A cool excess is noticeable in the binary's radiation even at $\lambda = 3.5$ μm. The observed excesses in the *K–L* color index are modest, and the principal difficulty in identifying the source is to obtain reliable estimates of its flux at $\lambda \geq 2.2$ μm range. These fluxes are determined by subtracting the supergiant fluxes from the observed *K*, *L*, and *M* fluxes. Johnson (1966) gave IR color indices for normal supergiants up to *V–N*, but Koornneef (1983) in his more recent study of IR radiation from normal stars provided color indices for O9–G8 supergiants only up to *K–L*.

We estimated the excess fluxes from ε Aur at $\lambda \geq 2.2$ μm relative to the radiation from an F0 supergiant ($K–L = 0\overset{m}{.}09$ and $K = M$). In this case, the mean *L–M* color index of the excess *LM* radiation is $\sim 0\overset{m}{.}7–0\overset{m}{.}8$, and the color temperature of the excess radiation source is 1000–1100 K. Its luminosity estimated from the excess *L* flux by using the relation L_2 (1000 K) ~ $4\pi r^2 F_2$ (3.5 μm) *A* is $\sim 4 \times 10^{35}$ erg s^{-1} ~ 110 $L_\odot$ for *r* = 600 pc, $L_{exc} \sim 4^m$, F_2 (3.5 μm) is the observed excess *L* (3.5 μm) flux, and *A* ~ 4.8 (the ratio of the total flux from a blackbody source with *T* ~ 1000 K to the 3.5-μm flux).

The radius of this cool source in the blackbody approximation is $R_2 \sim r[F_2$ (3.5 μm)/*B* (3.5 μm, 1000 K)$]^{0.5} \sim r \times 1.3 \times 10^{-8} \sim 350 R_\odot$, where *B* (3.5 μm, 1000 K) is the flux from a blackbody with *T* = 1000 K.

If the radius of an F0 supergiant is estimated from its flux at 1.25 μm (*J* band) using a similar relation, then its value is $R_1(7500) \sim r[F_1$ (1.25 μm)/*B* (1.25 μm, 7500 K)$]^{0.5} \sim r \times 5 \times 10^{-9} \sim 130 R_\odot$. Its luminosity is $L_1(\text{F0 I}) \sim 4\pi R_1^2 \sigma T^4 \sim 2 \times 10^{38}$ erg s^{-1} ~ $4.8 \times 10^4 L_\odot$, and M_{bol} (F0 I) ~ -7^m.

For a period of 9870 days, the radius of a circular orbit is ~$5200 R_\odot$. The equilibrium temperature at a distance of $5200 R_\odot$ from a normal F0 supergiant is $T_2' \approx W^{0.25} T(\text{F0}) \approx 840$ K, where $W \approx 0.25[R(\text{F0})/A]^2 \approx 1.5 \times 10^{-4}$ is the dilution factor. Given the accuracy of these estimates, we can say that the equilibrium temperature is close to that derived from the star's observed *LM* excesses. For example, at an eccentricity of 0.2 (Wright 1970), the equilibrium temperatures in conjunctions and at quadratures differ by more than 10% (1000 and 890 K). In other words, our observed cool source can be a formation heated by an F0 supergiant.

We began our out-of-eclipse observations of ε Aur in the summer of 1997. At this time, the binary was observed from the ISO satellite, and to our summer observations in 1997, we added data on the radiation from ε Aur at wavelengths of 10 (*N*) and 20 (*Q*) μm, retrieved via Internet from the Calgary University and ISO databases in order to determine how they agree. The ISO data for 3.5 and 5 μm were used to match the photometric systems. For an F0 supergiant, we assumed $K = N = Q$. For JD 2 450 670, the second column in Table 5 gives the observed (corrected for interstellar extinction) *KLMNQ* magnitudes (m_{obs}) of ε Aur,

Table 3. The mean brightness and color of ε Aur during eclipse in 1982–1984 and outside eclipse in 1982 (*UBVR*) and in 1995–2000 (*JHKLM*)

Parameter	Eclipse			Outside eclipse			Δ*m*
	value	SD	*N*	value	SD	*N*	
				UBVR			
JD24…	45510	120	20	45098	37	3	
U	2.65	0.06	20	1.68	0.22	3	0.97
B	2.71	0.04	20	1.93	0.16	3	0.78
V	2.54	0.03	20	1.87	0.10	3	0.67
R	2.34	0.04	20	1.68	0.05	3	0.66
U–B	−0.06/A5	0.04	20	−0.25/A2	0.08	3	0.19
B–V	0.17/A9	0.02	20	0.06/A2	0.06	3	0.11
V–R	0.20/F0	0.03	20	0.19/A9	0.06	3	0.01
				JHKLM			
JD24…	45513	119	21	51204	313	33	
J	2.21	0.06	20	1.53	0.03	33	0.68 (0.70)
H	2.11	0.07	20	1.38	0.05	33	0.73 (0.72)
K	2.04	0.06	20	1.33	0.03	33	0.71 (0.71)
L	1.98	0.10	2	1.16	0.03	33	0.82 (0.72)
M	1.90		1	1.19	0.04	33	0.71 (0.66)
V–J	0.33/A7	0.05	20	0.34/A8	0.06	3	−0.01
J–K	0.17/F0	0.05	19	0.2/F2	0.03	33	−0.03 (−0.01)
K–L	0.06	0.11	2	0.17	0.03	33	−0.11 (−0.01)

Table 4. Estimated parameters for long-period binaries

Object	$(J–K)_0$	se	SP(*J–K*)	SP(GCVS)	T_{eff}, K (John)	J_0	se	F_{tot}, erg s^{-1} cm^{-2}	$L/L_\odot$	M_{bol}
ζ Aur	0.96	0.01	K5 I-III	K5 II	3750 20	1.06	0.00	2.2×10^{-6}	4600	−1.9
VV Cep	1.00	0.01	M1 I	M2 I	3620 40	0.81	0.01	1.6×10^{-6}	27700	−6.3
ZZ CMi	1.25	0.01	M5 III	M6 I-II	2950 ?	4.14	0.02	7.5×10^{-8}	(4700)	(−4.45)
WY Gem	1.10	0.00	M3 III	M2 I	3300	2.80	0.00	2.6×10^{-7}	26000	−6.3
ε Aur (max)	0.20	0.00	F1 I	(A8-F2) I	7270	1.52	0.00	4.4×10^{-6}	49000	−7
ε Aur (min)	0.18	0.03	F0 I		7500 ± 300	2.30	0.01	2.2×10^{-6}	24500	−5.6

and the third column lists magnitudes for an F0 I supergiant. The next columns give *LMNQ* magnitudes and color indices for the excess radiation [*m*(exc)], and the last column lists the blackbody temperatures (T_d) corresponding to the color indices.

The table shows that the blackbody source with $T \sim 1000$ K is seen up to 10 μm, while the *NQ* radiation corresponds to a source with $T < 400$ K. The existence of a cool source with $T \sim 500$ K in ε Aur was established by analyzing the binary's IR observations during eclipse [see Carroll *et al.* (1991) for references], and it was assumed that this source might be the system's secondary component.

Table 5. Excess *LMNQ* radiation from the eclipsing binary ε Aur outside eclipse

λ, μm	m_{obs}	*m*(F0I)	*m*(exc)	T_d, K
2.2 (*K*)	1.32	1.33	–	
3.5 (*L*)	1.15	1.24	~3.9	
L–M			0.8	~1000
5 (*M*)	1.14	1.33	~3.1	
M–N			0.9	~1100
10 (*N*)	~0.94	1.33	~2.2	
N–Q			1.2	<400
20 (*Q*)	~0.4	1.33	~1	

In recent years, a number of studies have been devoted to elucidating the nature of the eclipsing binary's secondary component [see Lissauer *et al.* (1996) for references].

CONCLUSION

Our main conclusions can be formulated as follows.

The *JHKLM* brightness variations in the long-period variables studied (except for ε Aur) over the period of our monitoring were in the range $0^m.10$–$0^m.15$ and exceeded only slightly the observational errors (about $0^m.02$–$0^m.03$).

In the two-color *J–K–K–L* diagram, ζ Aur lies near the branch of normal supergiants (K5–M1); VV Cep is located in the region of K5–M1.5 supergiants; ZZ CMi is close to normal M4.5–M5 giants; and WY Gem lies on the branch of M2–M2.5 supergiants. For the above variables, we found no excess IR emission at 3.5 μm (and at 5 μm).

There may be a periodicity with $P \sim 430$ days and JD(max) = 2 450 907(±10) + 430(±7) E in the IR radiation from WY Gem. The *J*-band amplitude is about $0^m.1$, and the *J–K* color index decreases from maximum to minimum *J* brightness by a few hundredths of a magnitude; i.e., the cool star at maximum *J* light is hotter by approximately 100 K than it is at minimum *J* light. The cool star in WY Gem probably undergoes temperature pulsations with $\Delta T \sim 100$ K and a period of ~430 days.

The observed IR brightness and color variations in the eclipsing binary ε Aur during and outside eclipse (except for the IR brightness variations on the descending and ascending branches) did not exceed $0^m.10$–$0^m.15$. During eclipse, the *J* light reached a minimum near phase 0.99, and a local maximum was observed at phase ~1.01. These variations may reflect periodic (~400 days) IR brightness variations in one of the system's components. The binary's radiation in the 0.7–2.2 μm spectral range (*R*, *J*, *H*, and *K* bands), both outside and during eclipse, can be described by the radiation from a normal F0 supergiant with an error in the flux of less than 10%. The (mean) neutral fading during eclipse in this range is $0^m.70 \pm 0^m.02$; i.e., about half of the supergiant's visible disk is shielded during eclipse. The mean *K–L* color indices outside eclipse exceed their values for normal stars, and cool excess emission is noticeable even at λ = 3.5 μm. The mean *L–M* color index of the excess *LM* radiation is ~$0^m.7$–$0^m.8$, and the color temperature of the excess radiation source is 1000–1100 K. Its luminosity is L_2 (1000 K) ~ 110 $L_\odot$, and its radius is $R_2 \sim 350 R_\odot$. ISO observations of the binary confirm the existence of a blackbody source with $T \sim 1000$ K. Its radiation is visible up to 10 μm; the radiation at 20 μm belongs to a cooler source ($T <$ 400 K).

ACKNOWLEDGMENTS

This study was supported by the State Science and Technology Program "Astronomy" and the Russian Foundation for Basic Research (project no. 00-02-16353).

REFERENCES

1. D. E. Backman, E. E. Becklin, and D. P. Cruikshank, Astrophys. J. **284**, 799 (1984).
2. P. D. Bennet and G. H. Harper, Astrophys. J. **471**, 454 (1996).
3. B. W. Bopp, Publ. Astron. Soc. Pac. **96**, 894 (1984).
4. R. H. Buss and Yh. P. Snow, Astrophys. J. **335**, 331 (1988).
5. S. M. Carroll, E. F. Guinan, G. P. McCook, and R. A. Donahue, Astrophys. J. **367**, 278 (1991).
6. T. S. Chernova, Perem. Zvezdy **7**, 140 (1949).
7. R. E. Gershberg, Astron. Zh. **67**, 76 (1990) [Sov. Astron. **34**, 39 (1990)].
8. W. D. Heintz and B. A. Cantor, Publ. Astron. Soc. Pac. **106**, 363 (1994).
9. T. Iijima, Inf. Bull. Var. Stars, No. 2491 (1984).
10. H. L. Johnson, Annu. Rev. Astron., Astrophys. **4**, 163 (1966).
11. H. L. Johnson, R. I. Mitchel, B. Iriarte, and W. Z. Wisniewski, Commun. Lunar Planet. Lab. **4**, 99 (1966).
12. P. N. Kholopov, N. N. Samus', V. P. Goranskiĭ, *et al.*, *General Catalogue of Variable Stars* (Nauka, Moscow, 1985–1990).
13. J. Koornneef, Astron. Astrophys. **128**, 84 (1983).
14. J. J. Lissauer, S. J. Wolk, C. A. Griffit, and D. E. Backman, Astrophys. J. **465**, 371 (1996).
15. V. I. Moroz, O. G. Taranova, V. I. Shenavrin, and B. F. Yudin, Astron. Tsirk., No. 1056 (1979).
16. A. É. Nadzhip, V. I. Shenavrin, and V. G. Tikhonov, Tr. Gos. Astron. Inst., Mosk. Gos. Univ. **58**, 119 (1986).
17. J. Sahade, E. Brandi, and J. M. Foutenla, Astron. Asrophys., Suppl. Ser. **56**, 17 (1984).
18. R. F. Sanford, Publ. Astron. Soc. Pac. **59**, 136 (1947).
19. T. Tsuji, Astron. Asrophys. **62**, 29 (1978).
20. Wm. B. Weaver and V. Torres-Dodren, Astrophys. J. **446**, 300 (1995).
21. K. O. Wright, Vistas Astron. **12**, 147 (1970).
22. R. Zamanov and T. Tomov, Inf. Bull. Var. Stars, No. 3705 (1992).

Translated by N. Samus'